Applied Computational Electromagnetics Society

Journal

November 2011

Vol. 26 No. 11

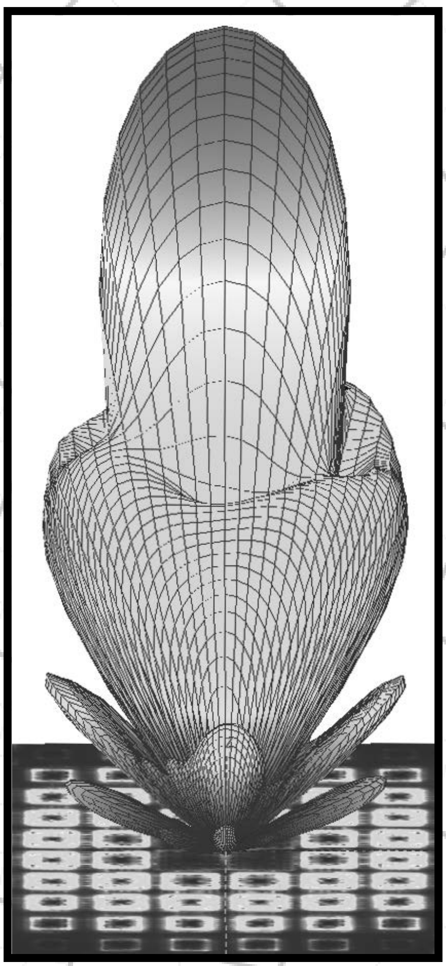

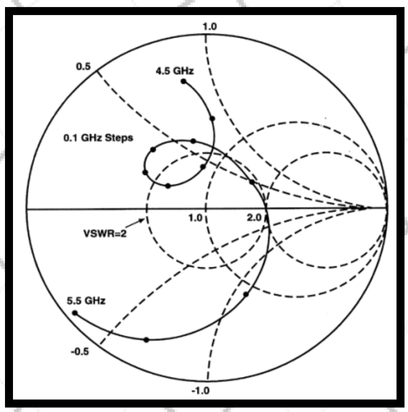

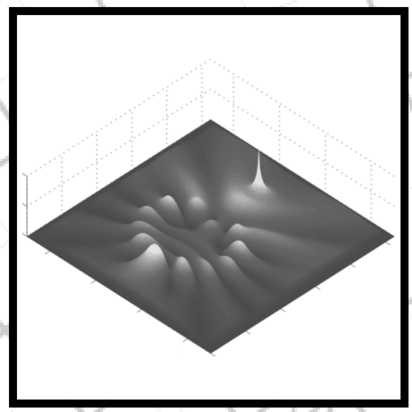

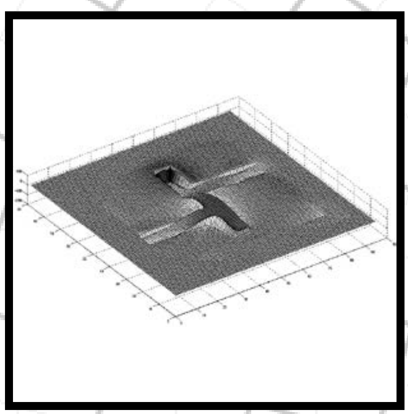

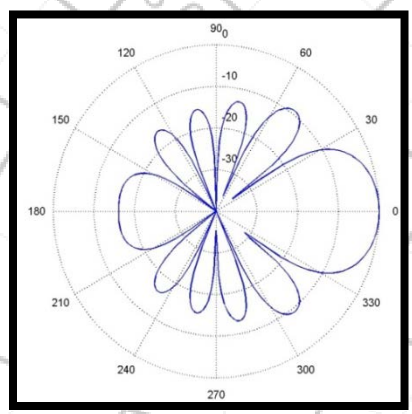

ISSN 1054-4887

GENERAL PURPOSE AND SCOPE: The Applied Computational Electromagnetics Society ***(ACES)*** Journal hereinafter known as the ***ACES Journal*** is devoted to the exchange of information in computational electromagnetics, to the advancement of the state-of-the art, and the promotion of related technical activities. The primary objective of the information exchange is to inform the scientific community on the developments of new computational electromagnetics tools and their use in electrical engineering, physics, or related areas. The technical activities promoted by this publication include code validation, performance analysis, and input/output standardization; code or technique optimization and error minimization; innovations in solution technique or in data input/output; identification of new applications for electromagnetics modeling codes and techniques; integration of computational electromagnetics techniques with new computer architectures; and correlation of computational parameters with physical mechanisms.

SUBMISSIONS: The ***ACES Journal*** welcomes original, previously unpublished papers, relating to applied computational electromagnetics. Typical papers will represent the computational electromagnetics aspects of research in electrical engineering, physics, or related disciplines. However, papers which represent research in applied computational electromagnetics itself are equally acceptable.

Manuscripts are to be submitted through the upload system of ***ACES*** web site http://aces.ee.olemiss.edu See "Information for Authors" on inside of back cover and at ***ACES*** web site. For additional information contact the Editor-in-Chief:

Dr. Atef Elsherbeni
Department of Electrical Engineering
The University of Mississippi
University, MS 386377 USA
Phone: 662-915-5382
Email: atef@olemiss.edu

SUBSCRIPTIONS: All members of the Applied Computational Electromagnetics Society are entitled to access and download the ***ACES Journal*** any published journal article available at http://aces.ee.olemiss.edu. Printed issues of the ***ACES Journal*** are delivered to institutional members. Each author of published papers receives a printed issue of the ***ACES Journal*** in which the paper is published.

Back issues, when available, are $50 each. Subscription to ***ACES*** is through the web site. Orders for back issues of the ***ACES Journal*** and change of address requests should be sent directly to ***ACES*** office at:

Department of Electrical Engineering
The University of Mississippi
University, MS 386377 USA
Phone: 662-915-7231
Email: aglisson@olemiss.edu

Allow four weeks advance notice for change of address. Claims for missing issues will not be honored because of insufficient notice, or address change, or loss in the mail unless the ***ACES*** office is notified within 60 days for USA and Canadian subscribers, or 90 days for subscribers in other countries, from the last day of the month of publication. For information regarding reprints of individual papers or other materials, see "Information for Authors".

LIABILITY. Neither ***ACES***, nor the ***ACES Journal*** editors, are responsible for any consequence of misinformation or claims, express or implied, in any published material in an ***ACES Journal*** issue. This also applies to advertising, for which only camera-ready copies are accepted. Authors are responsible for information contained in their papers. If any material submitted for publication includes material which has already been published elsewhere, it is the author's responsibility to obtain written permission to reproduce such material.

APPLIED COMPUTATIONAL ELECTROMAGNETICS SOCIETY JOURNAL

November 2011
Vol. 26 No. 11
ISSN 1054-4887

The ACES Journal is abstracted in INSPEC, in Engineering Index, DTIC, Science Citation Index Expanded, the Research Alert, and to Current Contents/Engineering, Computing & Technology.

The illustrations on the front cover have been obtained from the research groups at the Department of Electrical Engineering, The University of Mississippi.

NOVEMBER 2011 REVIEWERS

Ahmed Abdelrahman
John Aldrin
Ayman Al-Zayed
Marco Arjona
Ahmed Boutejdar
Nihad Dib
Ali Farahbakhsh
Antonio Faraone
Naftali Herscovici
Hai Jiang
Darko Kajfez
Said El-Khamy
Chao Li
Morui Li
Mingyu Lu
Francisco Medina
Zahera Mekkioui
Paolo Mezzanette
Yoginder Negi
Andrew Peterson
Qinjiang Rao
Colan Ryan
Harvey Schuman
Theodoros Tsiboukis
Yasuhiro Tsunemitsu
Bing Xiao
Wenhua Yu

THE APPLIED COMPUTATIONAL ELECTROMAGNETICS SOCIETY

JOURNAL

Vol. 26 No. 11 November 2011

TABLE OF CONTENTS

Efficient Multilevel Compressed Block Decomposition for Large-Scale Electromagnetic Problems using Asymptotic Phasefront Extraction

Z. N. Jiang, R. S. Chen, Z. H. Fan, S. G. Shen, and X. Q. Hu

Department of Communication Engineering
Nanjing University of Science and Technology, Nanjing, China, 210094
eechenrs@mail.njust.edu.cn

Abstract- A large dense complex linear system can be obtained when solving an electromagnetic scattering problem with the surface integral equation approach. To analyze the large dense complex linear system efficiently, the multilevel compressed block decomposition (MLCBD) is used to accelerate the matrix-vector multiplication operations. Although the MLCBD is efficient compared with the direct method of moments, it is still less efficient for the large-scale electromagnetic problems. Therefore, an efficient version of MLCBD is proposed in this paper. It utilizes the asymptotic phasefront extraction (APE) to reduce the exorbitant dependence on computer storage and solution time in the MLCBD for analyzing the large-scale electromagnetic problems. The numerical results demonstrate that the APE combined with MLCBD is much more efficient than conventional MLCBD for analyzing the large-scale electromagnetic scattering problems.

Index terms- Asymptotic phasefront extraction (APE), electromagnetic scattering, multilevel compressed block decomposition (MLCBD).

I. INTRODUCTION

In electromagnetic wave scattering calculations, a classical problem is to compute the equivalent surface currents induced by a given incident plane wave. Such calculations, relying on the Maxwell equations, are required in the simulation of many industrial processes ranging from antenna design, electromagnetic compatibility, computation of back-scattered fields, and so on. All these simulations require fast and efficient numerical methods to compute an approximate solution of Maxwell's equations. The method of moments (MoM) [1-2] is one of the most widely used techniques for electromagnetic problems. However, It is basically impractical to solve electric-field integral-equation (EFIE) matrix equations using MoM because its memory requirement and computational complexity are of the orders of $O(N^2)$ and $O(N^3)$, respectively, where N is the number of unknowns.

To alleviate this problem, many fast solution algorithms have been developed. The first kind of algorithms is the fast iterative solution. The most popular fast iterative solution includes the multilevel fast multipole algorithm (MLFMA) [3–4], with $O(N\log N)$ complexity for a given accuracy. Though efficient and accurate, this algorithm is highly technical. It utilizes a large number of tools, such as partial wave expansion, exponential expansion, filtering, and interpolation of spherical harmonics. MDA-SVD is another popular iterative solution used to analyze the scattering/radiation [5-6], which exploits the well known fact that for well separated sub-scatterers, the corresponding sub-matrices are low rank and can be compressed. The second kind of algorithms

Submitted On: Oct. 24, 2010
Accepted On: March 6, 2011

is the fast direct solution. The *H*-matrix technique [7] is one of the most popular fast direct solutions, which is based on a *data-sparse* representation. [8] introduces a popular direct solution, which is based on the adaptive cross approximation (ACA). The MLCBD algorithm [9-11] is another popular direct solution. It is based on a blockwise compression of the impedance matrix, by the same technique as used in the matrix decomposition algorithm (MDA) [12-13]. The numerical complexity of the algorithm is shown to be $O(N^2)$ and the storage requirements scale with $O(N^{1.5})$ [11].

Although both the numerical complexity and the storage requirement of the fast iterative solution are less than that of the fast direct solution, the convergence rate of iterative methods can vary in an unpredictable way. The complexity of the iterative solution method is depending on the matrix condition number. Iterative solvers may be quite satisfactory for only a few right-hand sides (RHS) such as antenna or bistatic problems, but become expensive for monostatic scattering with many required sampling angles. It is well known that the matrix condition number of EFIE for electrically large problem is large [14]. Therefore, the system has poor convergence history.

The aim of this paper is to present a more efficient MLCBD for the large-scale electromagnetic problems. It utilizes the APE method [15-21] to reduce the number of unknowns. Simulation results show that the proposed method is computationally more efficient than for the conventional MLCBD.

The remainder of this paper is organized as follows. Section II gives the theory of APE. Section III describes the theory and implementation of MLCBD in more details. Numerical experiments are presented to demonstrate the efficiency of this proposed method in Section IV. Conclusions are provided in Section V.

I. The Theory of APE

A. The formulation of EFIE

In the work proposed for this paper, the electric field integral equation (EFIE) formulation is adopted [2]. The formulation of EFIE can be expressed as

$$\hat{t}\bullet\int_S \overrightarrow{G}(\mathbf{r},\mathbf{r}')\mathbf{J}(\mathbf{r}')dS' = \frac{4\pi i}{k\eta}\hat{t}\bullet\mathbf{E}^i(\mathbf{r})\,. \qquad (1)$$

Here, $\overrightarrow{G}(\mathbf{r},\mathbf{r}')$ refers to the dyadic Green's function, $\hat{t}$ is any unit tangential vector to S at $\boldsymbol{r}$, $\boldsymbol{E}^{\boldsymbol{i}}(\mathbf{r})$ is the incident excitation plane wave, and η and k denote the free space impendence and wave number, respectively. $\mathbf{J}(\mathbf{r}')$ is the induced current density on S, which is the unknown of the problem.

B. Asymptotic phasefront extraction

According to the formulation of the conventional MoM [2], the induced current **J** is expanded in terms of subsectional basis functions. On the smooth regions S of the object, where the induced surface currents present an asymptotic behavior [22], the current density is expanded in terms of the proposed asymptotic phasefront extraction (APE) basis functions. Since the dominant phase variation is included within the function formulation, the current density in these regions can be efficiently represented using a low number of basis functions. The formulation of the asymptotic phasefront extraction (APE) basis functions is given as follows:

$$f_n(r) = \begin{cases} \Lambda_n^+ e^{-jk_n^+(\rho_n^+ - \rho_{nc}^+)} & r \ in \ T_n^+ \\ \Lambda_n^- e^{-jk_n^-(\rho_n^- - \rho_{nc}^-)} & r \ in \ T_n^- \\ 0 & otherwise \end{cases}, \qquad (2)$$

where $\Lambda_n^{\pm}$ are the RWG vector basis functions [23], defined by

$$\Lambda_n^{\pm} = \pm \frac{l_n}{2A_n^{\pm}} \rho_n^{\pm}, \qquad r \; in \; T_n^{\pm} \, . \tag{3}$$

The l_n is the length of the common edge to the triangles $T_n^{\pm}$ conforming the basis function, $A_n^{\pm}$ is the area of each triangle, $\rho_n^{\pm}$ is the corresponding vector from the free vertex of $T_n^{\pm}$ to a point r on the triangle, and $\rho_{nc}^{\pm}$ is the vector from the free vertex of the triangle $T_n^{\pm}$ to the midpoint of the common edge r_{nc}. Finally, k_n is the vector wavenumber associated to the phase of the current density on the function. Thus, including the incident phase in the RWG basis functions should allow a reduction in the density of the mesh for regions away from discontinuities.

Away from the smooth parts, where the asymptotic representation becomes invalid, the current density can be accurately modeled using a higher density of ordinary RWG basis functions. Then, the impedance matrix which is gained through the EFIE equation can be symbolically rewritten as:

$$ZI = V \, . \tag{4}$$

To solve the above matrix equation by a direct method, a fast method is needed. In this paper, the multilevel compressed block decomposition (MLCBD) is used.

II. Multilevel Compressed Block Decomposition

A. Block decomposition

When the equation (4) is solved by the fast iterative solution, the convergence rate can vary in an unpredictable way. Therefore, the multilevel compressed block decomposition (MLCBD) is used, which is independent on the matrix condition number. Take three dimensional problems into account; MLCBD is based on the data structure of the binary trees. The binary trees are obtained by subdividing an index set into two subsets recursively. In Fig. 1, the box enclosing the object is subdivided into smaller boxes at multiple levels, in the form of a binary tree. The far interaction boxes [9] are analyzed by MDA-SVD at each level. Consider there exists two boxes at the same level, one is a source box i which contains m_1 basis functions and the other is an observation box j which contains m_2 test functions. The impedance matrix between two well-separated boxes can be expressed through low rank representations [10-11].

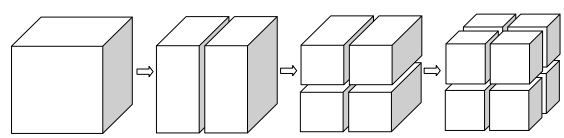

Fig. 1. Sketch of the binary trees structure.

MDA utilizes this low rank nature of the interaction between two well-separated boxes. In MDA implementation, the impedance matrix of the two well-separated boxes can be expressed as three small matrices [10-11]

$$[Z_{ij}]_{m_1 m_2} = [\tilde{U}_{ij}]_{m_1 r} [\tilde{\omega}_{ij}]_{rr}^{-1} [\tilde{V}_{ij}]_{m_2 r}^{T} \, , \tag{5}$$

where $[Z_{ij}]_{m_1 m_2}$ is the interaction matrix between observation and source boxes. r denotes the number of equivalent RWG sources [10-11], which is much smaller than m_1 and m_2.

Since the matrices $[\tilde{U}_{ij}]_{m_1 r}$ and $[\tilde{V}_{ij}]^T_{m_2 r}$ generated by MDA are usually not orthogonal, they may contain redundancies, which can be removed by the following algebraic recompression technique. This method may be regarded as the singular value decomposition optimized for rank-*k* matrices. Utilize QR and SVD to reorthonormalize $[\tilde{U}_{ij}]_{m_1 r}$ and $[\tilde{V}_{ij}]^T_{m_2 r}$ and the equation (5) can be obtained as

$$[Z_{ij}]_{m_1 m_2} = [U_{ij}]_{m_1 r}[\omega_{ij}]^{-1}_{rr}[V_{ij}]^T_{m_2 r}\,, \qquad (6)$$

where $[U_{ij}]_{m_1 r}$ and $[V_{ij}]^T_{m_2 r}$ are both orthogonal. These techniques can reduce the required amount of storage of MDA, while the asymptotic complexity of the approximation remains the same.

At the finest level, blocks (which do not include the self-interaction blocks) representing interactions between adjacent source and observation boxes are compressed by SVD (T) compression. The details of the SVD (T) compression are shown in [23]. The impedance matrix can be expressed as that shown in Fig. 2 (a). The *A* and *B* blocks of the impedance matrix are stored in compressed form as the product of three matrices (6).

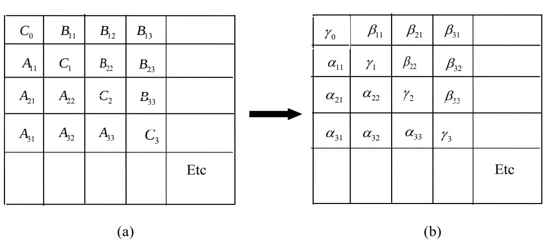

Fig. 2. Transformation from blocked impedance matrix to block inverse.

B. The theory of CBD

The procedure of the CBD is shown in this part. According to [23], CBD is based on the blockwise compressed matrix which is shown in Fig. 2 (a). The details of the CBD is shown in following,

Algorithm CBD (M blocks)

1) $\Pi_0 = C_0^{-1}$
2) For $i = 1$ *to* M−1 do
3) For $j = 1$ *to* i do
4) $P_{jj} = \gamma_{j-1}\left(B_{ij} - \Sigma_{k=1}^{j-1}\alpha_{j-1,k}B_{i,k}\right)$
5) $Q_{jj} = \left(A_{ij} - \Sigma_{k=1}^{j-1}A_{i,k}\beta_{j-1,k}\right)\gamma_{j-1}$
6) *reorthonormalize* P_{jj} *and* Q_{jj}
7) For $k = 1$ *to* $j-1$ do
8) $P_{jk} = P_{j-1,k} - \beta_{j-1,k}P_{jj}$
9) $Q_{jk} = Q_{j-1,k} - Q_{jj}P_{j-1,k}$
10) *reorthonormalize* P_{jk} *and* Q_{jk}
11) End(k)
12) End(j)
13) For $k = 1$ to i do; $\beta_{ik} = P_{ik}$; $\alpha_{ik} = Q_{ik}$; $End(k)$
14) $\gamma_i = \left(C_i - \Sigma_{j=1}^{i}A_{ij}\beta_{ij}\right)^{-1}$
15) End(i)

Steps 6) and 10) of the algorithm are explained in [23]. In order to use the decomposed matrix to an independent vector X to obtain the linear system solution y, the independent vector is subdivided according to the blocks of the impedance matrix, yielding a set of vectors $X_0, \cdots, X_{M-1}$. Then the algorithm Apply_CBD given in the following is used to compute the solution block by block.

Algorithm Apply_CBD (X)

1) *For* $i = 0$ *to* $M-1$ *do*
2) $y_i = \gamma_i\left(X_i - \Sigma_{j=1}^{i}\alpha_{ij}X_{j-1}\right)$
3) *For* $i = 0$ *to* $M-1$ *do*
4) $y_{j-1} = y_{j-1} - \beta_{ij}y_i$
5) $End\left(j\right)$
6) $End\left(i\right)$

C. The multilevel CBD

When the size of solving problem increases, the computational costs of the step 14) of the algorithm is very large [9]. The remedy is to subdivide again the self-interaction matrix into several smaller submatrices. This procedure is called the multilevel version of CBD [9-11], which is shown in Fig. 3.

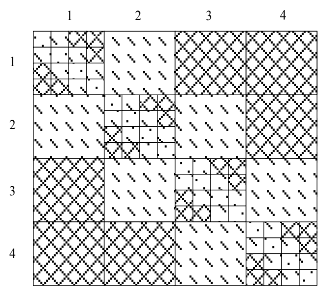

Fig. 3. The procedure of recursive sub-division of the self-interaction matrices.

III. NUMERICAL RESULTS

To validate and demonstrate the accuracy and efficiency of the proposed method, some numerical results are presented in this section. It is because of that that the impedance matrix formed by asymptotic phase is not symmetrical; the impedance matrix of the proposed method is not symmetrical. All the computations are carried out on Intel(R) Core(TM) 2 Quad CPU at 2.83 GHz and 8 GB of RAM in double precision and the truncating tolerance of the MDA-SVD is 10^{-3} relative to the largest singular value.

A. Sphere

First, we consider the scattering of a perfectly electrically conducting (PEC) sphere with radius 1.6λ at 300 MHz. The incident direction is $\theta_i = 0^\circ, \phi_i = 0^\circ$ and the scattered angles vary from 0° to 180° in the azimuthal direction when the pitch angle is fixed at 0°. The conventional MLCBD solution needs 10107 unknowns with 0.1λ patch size, while the proposed method only needs 396 unknowns with 0.5λ patch size. The number of the binary trees is $L=7$. Figure 4 compares the analytical Mie solution with the results of the proposed method. There is a good agreement between them.

Table I summarizes the matrix building and inversion time and the matrix building and inversion memory of the conventional MLCBD and the proposed method. It can be observed that the time and memory of the matrix building and inversion time of the proposed method are much less than that of the conventional MLCBD. The matrix building and inversion time and the matrix building and inversion memory of the proposed method for the sphere at 1 GHz are also shown in the Tab. I. The sphere is discretized with 115707 unknowns with 0.1λ patch size by using the conventional MLCBD, while it is discretized with only 1689 unknowns with 0.8λ patch size by using the proposed method. The number of the unknowns by using the conventional MLCBD is very large, which can not be analyzed on the computer used in this paper. It can be observed that the memory and time of the proposed are very few for the 10.6λ sphere.

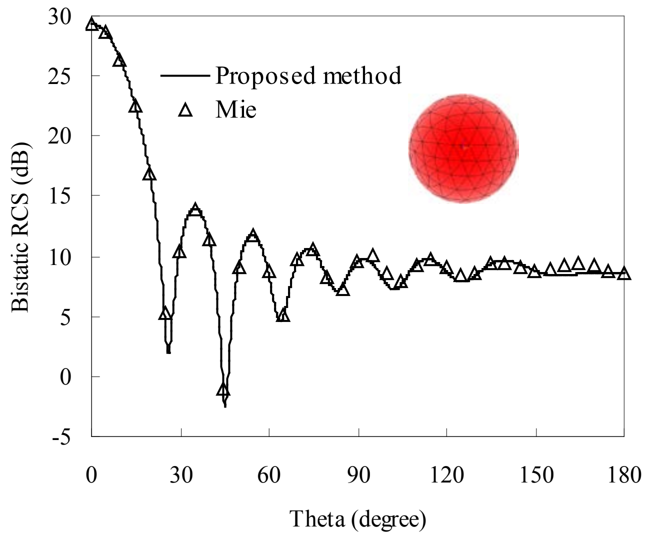

Fig. 4. Bistatic scattering cross section of the sphere.

Table 1: The matrix building and inversion time and the matrix building and inversion memory of the proposed method for the sphere

Frequency	Algorithms	Matrix building		Matrix inversion	
		Memory (MB)	**Time (S)**	**Memory (MB)**	**Time (S)**
300 MHz	Proposed method	4	8	5	49
	MLCBD	222	151	219	753
1 GHz	Proposed method	56	100	106	428
	MLCBD	~	~	~	~

B. Plane

The second example is a plane. The dimension of the structure is $4\,m\times 2\,m$. The rotation axis of plane geometry is *z*-axis. The incident and scattered angles are ($\theta_i = 0^\circ, \phi_i = 0^\circ$) and ($0^\circ \le \phi_s \le 180^\circ, \theta_s = 90^\circ$), respectively.

The frequency is 3 GHz. The conventional MLCBD solution needs 276606 unknowns with 0.1λ patch size, while the proposed method only needs 5691 unknowns with the middle part of the plane is discretized with 0.9λ. The number of the binary trees is $L = 9$. The bistatic RCS by use of the proposed method is shown in Fig. 5, and is agreed well with that of the MLFMA.

Table 2 shows the matrix building and inversion time and the matrix building and inversion memory of the proposed method. It can be found that the proposed method needs much less memory and time for analyzing the 40λ plane.

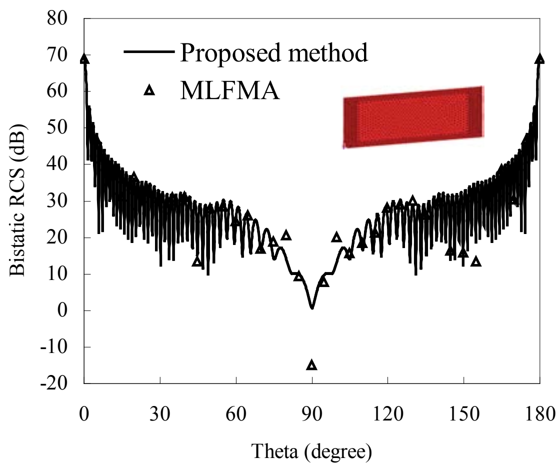

Fig. 5. Bistatic scattering cross section of plane.

Table 2: The matrix building and inversion time and the matrix building and inversion memory of the proposed method for plane

Algorithms	Matrix building		Matrix inversion	
	Memory (MB)	Time (s)	Memory (MB)	Time (s)
Proposed method	130	326	138	137

C. Airplane

The last example is the airplane model. The dimension of the structure is $10\,m \times 8.5\,m \times 2.75\,m$. The rotation axis of the airplane geometry is the *x*-axis. The incident and scattered angles are ($\theta_i = 90^\circ, \phi_i = 0^\circ$) and ($0^\circ \le \phi_s \le 180^\circ, \theta_s = 90^\circ$), respectively. The frequency is 600 MHz. The conventional MLCBD solution needs 99795 unknowns with 0.1λ patch size, while the proposed method only needs 6246 unknowns with the smooth parts of the airplane discretized with 0.8λ. The number of the binary trees is $L = 9$. The bistatic RCS by using the proposed method is shown in Fig. 6, which is compared with the results of the MLFMA. It can be found that the results of the proposed method are well agreed with that of the MLFMA.

The matrix building and inversion time and the matrix building and inversion memory of the proposed method are also given in the Tab. III. It can be seen that the proposed method needs much less memory and time for analyzing the 20λ airplane.

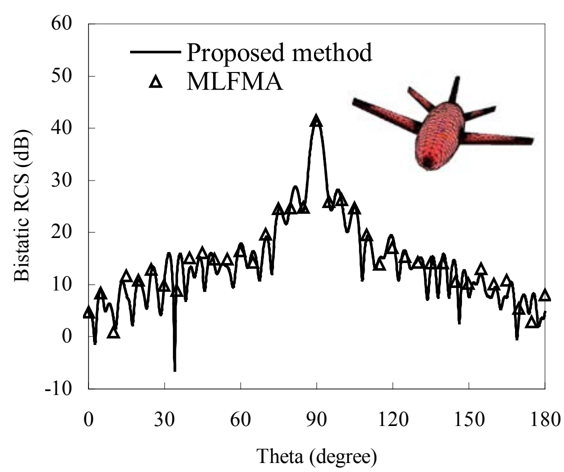

Fig. 6. Bistatic scattering cross section of airplane.

IV. CONCLUSIONS

In this paper, an efficient version of MLCBD is introduced. It utilizes the APE method to represent the unknown surface currents in very large scatters using a low number of unknowns. The numerical results demonstrate that the efficient version of the MLCBD is efficient for the EFIE analysis of large-scale electromagnetic scatterings. Compared with the conventional MLCBD, the efficient version of MLCBD can reduce the solution time and memory requirement significantly.

Table 3: The matrix building and inversion time and the matrix building and inversion memory of the proposed method for airplane

Algorithms	Matrix building		Matrix inversion	
	Memory (MB)	Time (s)	Memory (MB)	Time (s)
Proposed method	215	614	292	1154

ACKNOWLEDGMENT

We would like to thank the support of Major State Basic Research Development Program of China (973 Program: 2009CB320201); Natural Science Foundation of 60871013, 60701004, 60928002; Jiangsu Natural Science Foundation of BK2008048.

REFERENCES

[1] R. F. Harrington, *Field Computations by Moment Methods*, MacMillan, New York, 1968.

[2] S. M. Rao, D. R. Wilton, and A. W. Glisson, "Electromagnetic Scattering by Surfaces of Arbitrary Shape," *IEEE Trans. Antennas Propagat.*, vol. AP-30, pp. 409-418, May 1982.

[3] R. Coifman, V. Rokhlin, and S.Wandzura, "The fast multipole method for the wave equation: A pedestrian prescription," *IEEE Antennas Propag. Mag.*, vol. 35, no. 6, pp. 7-12, Jun. 1993.

[4] W. C. Chew, J. M. Jin, E. Michielssen, and J. Song, *Fast efficient algorithms in computational electromagnetics*, Boston, MA: Artech House, 2001.

[5] J. M. Rius, J. Parron, A. Heldring, J. M. Tamayo, and E. Ubeda, "Fast iterative solution of integral equations with method of moments and matrix decomposition algorithm - singular value decomposition," *IEEE Trans. Antennas Propag*, vol. 56, no. 8, pp. 2314-2324, Aug. 2008.

[6] J. M. Rius, A. Heldring, J.M. Tamayo, and J. Parron, "The MDA-SVD algorithm for fast direct or iterative solution of discrete integral equations," Antennas Propag, *EuCAP The Second European Conference on*, pp. 1-8, 2007.

[7] M. Bebendorf and S. Rjasanow, "Adaptive low-rank approximation of collocation matrices," *Computing*, 70, pp. 1-24, 2003.

[8] J. Shaeffer, "Direct Solve of Electrically Large Integral Equations for Problem Sizes to 1 M Unknowns," *IEEE Trans. Antennas Propag*, vol. 56, no. 8, pp. 2306-2313, Aug. 2008.

[9] A. Heldring, J. M. Rius, J.M. Tamayo, and J. Parron, "Compressed Block-Decomposition Algorithm for Fast Capacitance Extraction," *IEEE Transactions on computer-aided design of integrated circuits and systems*, vol. 27, no. 2, pp. 265-271, Feb. 2008.

[10] A. Heldring, J. M. Rius, J.M. Tamayo, and J. Parron, "Multilevel MDA-CBI for fast direct solution of large scattering and radiation problems," *Antennas and Propagation Society International Symposium*, 2007.

[11] A. Heldring, J.M. Tamayo, J. M. Rius, J. Parron, and E. Ubeda, "Multiscale CBD for Fast Direct Solution of MoM Linear System," *Antennas and Propagation Society International Symposium*, 2008.

[12] E. Michielssen and A. Boag, "A multilevel matrix decomposition algorithm for analyzing scattering from large structures," *IEEE Trans. Antennas Propag*, vol. 44, no. 8, pp. 1086–1093, Aug. 1996.

[13] J. Parron, G. Junkin, and J. M. Rius, "Improving the performance of the multilevel matrix decomposition algorithm for 2.5-d structures application to metamaterials," *in Proc. Antennas Propag. Soc. Int. Symp*, pp. 2941-2944, Jul. 2006.

[14] A. Heldring, "Full wave analysis of electrically large reflector antenna," Ph.D. dissertation, Dept. Elect. Eng., Delft Univ. Technol., Delft, the Netherlands, April 2002.

[15] D.H. Kwon, R.J. Burkholder, and P.H. Pathak, "Efficient method of moments formulation for large PEC scattering problems using asymptotic

phasefront extraction (APE)," *IEEE Trans. Antennas Propag*, vol. 49, no. 4, pp. 583-591, Apr. 2001.

[16] F. Vico, G. Vecchi, and M. Ferrando, "Asymptotic phase extraction as a preconditioning technique for mom," *Antennas and Propagation Society International Symposium*, 2007.

[17] R. M. James, "A contribution to scattering calculation for small wavelengths-the high frequency panel method," *IEEE Trans. Antennas Propag*, vol. 38, no. 10, pp. 1625-1630, Oct. 1990.

[18] K. R. Aberegg and A. F. Peterson, "Application of the integral equation – asymptotic phase method to two-dimensional scattering," *IEEE Trans. Antennas Propag*, vol. 43, no. 5, pp. 534-537, May. 1995.

[19] T. Abboud, J.-C. Nedelec, and B. Zhou, "Improvement of the integral equation method for high frequency problems," *Third International Conference on Mathematical Aspects of Wave Propagation Phenomena*, SIAM, 1995.

[20] X. Shen, A. W. Davis, K. R. Aberegg, and A. F. Peterson, "Highly parallel implementation of the 3D integral equation asymptotic phase method for electromagnetic scattering," *Applied Computational Electromagnetics Society (ACES) Journal*, vol. 13, pp. 107-115, July 1998.

[21] M. E. Kowalski, B. Singh, L.C. Kempel, K.D. Trott, and J-M Jin, "Application of the Integral Equation-Asymptotic Phase (IE-AP) Method to Three-Dimensional Scattering," *J. Electromagnetic Waves Appl.*, 15, pp. 885-900, July 2001.

[22] Z. Altman, R. Mittra, O. Hashimoto, and E. Michielssen, "Efficient representation of induced currents on large scatterers using the generalized pencil of function method," *IEEE Trans. Antennas Propag*, vol. 44, no. 1, pp. 51-57, Jan. 1996.

[23] A. Heldring, J.M. Rius, J.M. Tamayo, J. Parron, and E. Ubeda, "Fast direct solution of method of moments linear system," *IEEE Trans. Antennas Propag*, vol. 55, no. 11, pp. 3220-3228, Nov. 2007.

Zhaoneng Jiang was born in Jiangsu Province, the People's Republic of China. He received the B.S. degree in Physics from Huaiyin Normal College in 2007, and is currently working toward the Ph.D. degree at Nanjing University of Science and Technology (NJUST), Nanjing, China. His current research interests include computational electromagnetics, antennas, and electromagnetic scattering and propagation, electromagnetic modeling of microwave integrated circuits.

Ru-Shan Chen (M'01) was born in Jiangsu, P. R. China. He received his B.Sc. and M.Sc. degrees from the Dept. of Radio Engineering, Southeast University, in 1987 and in 1990, respectively, and his Ph.D. from the Dept. of Electronic Engineering, City University of Hong Kong in 2001. He joined the Dept. of Electrical Engineering, Nanjing University of Science & Technology (NJUST), where he became a Teaching Assistant in 1990 and a Lecturer in 1992. Since September 1996, he has been a Visiting Scholar with Department of Electronic Engineering, City University of Hong Kong, first as Research Associate, then as a Senior Research Associate in July 1997, a Research Fellow in April 1998, and a Senior Research Fellow in 1999. From June to September 1999, he was also a Visiting Scholar at Montreal University, Canada. In September 1999, he was promoted to Full Professor and Associate Director of the Microwave & Communication Research Center in NJUST and in 2007, he was appointed Head of the Dept of Communication Engineering, Nanjing University of Science & Technology. His research interests mainly include microwave/millimeter-wave systems, measurements, antenna, RF-integrated circuits, and computational electromagnetics. He is a Senior Member of the Chinese Institute of Electronics (CIE). He received the 1992 third-class science and technology advance prize given by the National Military Industry Department of China, the 1993 third class science and technology advance prize given by the National Education Committee of China, the 1996 second-class science and technology advance prize given by the National Education Committee of China, and the 1999 first-class science and technology advance prize given by JiangSu Province as well as the 2001 second-class science and technology advance prize. At NUST, he was awarded the Excellent Honor Prize for academic achievement in 1994, 1996, 1997, 1999, 2000, 2001, 2002, and 2003. He has authored or co-authored more than 200 papers, including over 140 papers in international journals. He is the recipient of the Foundation for China Distinguished Young Investigators presented by the National Science Foundation (NSF) of China in 2003. In 2008, he became a Chang-Jiang Professor under the Cheung Kong Scholar Program awarded by the Ministry of Education, China.

Zhen-Hong Fan was born in Jiangsu, the People's Republic of China in 1978. He received the M.Sc. and Ph.D. degrees in Electromagnetic Field and Microwave Technique from Nanjing University of Science and Technology (NJUST), Nanjing, China, in 2003 and 2007, respectively. During 2006, he was with the Center of wireless Communication in the City University of Hong Kong, Kowloon, as a Research Assistant. He is currently an associated Professor with the Electronic Engineering of NJUST. He is the author or coauthor of over 20 technical papers. His current research interests include computational electromagnetics, electromagnetic scattering and radiation.

Songge Shen was born in Henan Province, the People's Republic of China. She received the B.S. degree in Physics from HeNan University in 2009, and is currently working toward the M.S. degree at Nanjing University of Science and Technology (NJUST), Nanjing, China. Her current research interests include computational electromagnetics, antennas and electromagnetic scattering and propagation, electromagnetic modeling of microwave integrated circuits.

Xiaoqing Hu was born in Hubei Province, the People's Republic of China. He received the M.S. degree in Physics from Nanjing University of Science and Technology (NJUST) in 2007, and is currently working toward the Ph.D. degree at Nanjing University of Science and Technology (NJUST), Nanjing, China. His current research interests include computational electromagnetics, antennas and electromagnetic scattering and propagation, electromagnetic modeling of microwave integrated circuits.

Electromagnetic Scattering by Arbitrary Shaped Three-Dimensional Conducting Objects Covered with Electromagnetic Anisotropic Materials

Xiaoqiao Deng, Changqing Gu, and Yonggang Zhou

College of Information Science and Technology, Nanjing University of Aeronautics and Astronautics, Nanjing, 210016, China
dengxiaoqiao_521@163.com, gucq0138@sina.com, iamrealzyg@yahoo.com.cn

Abstract **─** In this paper, the equivalent dipole-moment method (EDM) is extended and applied in the analysis of electromagnetic (EM) scattering by the arbitrarily shaped perfect electric conductor (PEC) targets coated with EM anisotropic media. At first, the volume integral equation and surface integral equation are built in the EM anisotropic material region and on the conducting surface, respectively. Then, the method of moments (MoM) is used to convert the integral equation into a matrix equation and the EDM is employed to reduce the CPU time of the matrix filling procedure. Numerical results are given to demonstrate the versatility of the proposed approach in handing with the EM scattering by arbitrarily shaped PEC targets coated with EM anisotropic media.

Index Terms **─** Equivalent dipole moment (EDM), EM anisotropic material, method of moments (MOM), radar cross section (RCS), volume-surface integral equation (VSIE).

I. INTRODUCTION

EM scattering from composite bodies consisting of both conductor and coated anisotropic medium is an important and challenging problem in computational electromagnetics. Many effective methods have been proposed, among which the physical optics (PO) method [1], the finite difference time domain FDTD method [2], and the MoM [3] are used commonly. However, the PO solution is approximate and show bigger error when solving the EM scattering from coated targets. FDTD has significant accumulated errors from numerical dispersion. The MoM and its accelerated methods can overcome these disadvantages and many previous works [3-10] have been done to investigate the scattering problems of composite bodies consisting of both conductor and coated anisotropic medium.

However, when computing the impedance matrix elements, the conventional MoM consumes a considerable portion of the total solution time and memory. Moreover, this problem becomes even more serious in the analysis of anisotropic media. In recent researches, the EDM [11-12] based on the volume-surface integration equations (VSIE) has been put forward to compute the RCSs of arbitrarily shaped PEC targets coated with electric anisotropic media. It is demonstrated that the EDM can save matrix-filling time efficiently. However, in [11-12], only electric anisotropic media is considered. In many applications, such as stealth materials, both electric and magnetic anisotropic media are often used. So, in this paper, the equivalent dipole-moment method is extended and applied to model arbitrary targets covered by arbitrary electric and magnetic anisotropic media.

The article is organized as follows: Section II presents the MOM associated with VSIE and introduces the EDM in detail for 3-D arbitrary shaped conducting objects covered with EM anisotropic materials, respectively; numerical results are given in Sections III and some conclusions are drawn in the final section.

II. FORMULATIONS

A. Introduction of VSIE and MOM

For generalizing the proposed method, we refer to scattering from an arbitrary shaped 3-D conducting object coated with anisotropic media, shown in Fig. 1. Region V is an anisotropic medium characterized by relative permittivity $\bar{\bar{\varepsilon}}_r$ and permeability $\bar{\bar{\mu}}_r$ as:

Submitted On: May 16, 2011
Accepted On: Oct. 21, 2011

$$\overline{\overline{\varepsilon}}_r = \begin{bmatrix} \varepsilon_{\mathrm{xx}} & \varepsilon_{\mathrm{xy}} & \varepsilon_{\mathrm{xz}} \\ \varepsilon_{\mathrm{yx}} & \varepsilon_{\mathrm{yy}} & \varepsilon_{\mathrm{yz}} \\ \varepsilon_{\mathrm{zx}} & \varepsilon_{\mathrm{zy}} & \varepsilon_{\mathrm{zz}} \end{bmatrix}, \overline{\overline{\mu}}_r = \begin{bmatrix} \mu_{\mathrm{xx}} & \mu_{\mathrm{xy}} & \mu_{\mathrm{xz}} \\ \mu_{\mathrm{yx}} & \mu_{\mathrm{yy}} & \mu_{\mathrm{yz}} \\ \mu_{\mathrm{zx}} & \mu_{\mathrm{zy}} & \mu_{\mathrm{zz}} \end{bmatrix}. \quad (1)$$

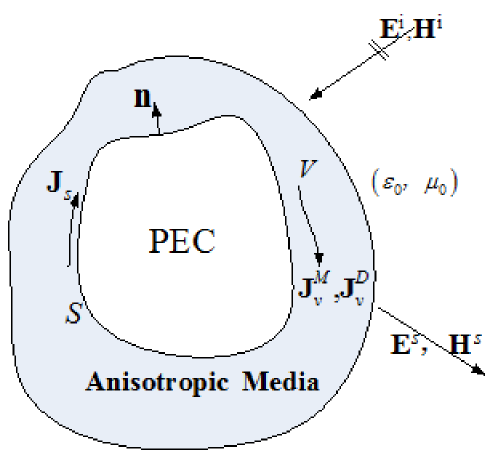

Fig. 1. Arbitrarily shaped conducting/anisotropic mixed body illuminated by a plane wave.

Let S denote the surface of a PEC object with unit normal vector n and the incident fields $\mathbf{E}^{\mathrm{i}}, \mathbf{H}^{\mathrm{i}}$ are due to an impressed source in the absence of the target. Hence, the EM field on the surface of the conducting object and in the volume of the anisotropic media must satisfy the equations below,

$$\mathbf{n} \times \left[\mathbf{E}^{\mathrm{i}} + \mathbf{E}^s\left(\mathbf{J}_s\right) + \mathbf{E}^s\left(\mathbf{J}_v^D\right) + \mathbf{E}^s\left(\mathbf{J}_v^M\right) \right] = 0, \quad \text{on S} \quad (2)$$

$$\mathbf{E} = \mathbf{E}^i + \mathbf{E}^s\left(\mathbf{J}_s\right) + \mathbf{E}^s\left(\mathbf{J}_v^D\right) + \mathbf{E}^s\left(\mathbf{J}_v^M\right), \quad \text{in V} \quad (3)$$

$$\mathbf{H} = \mathbf{H}^{\mathrm{i}} + \mathbf{H}^{\mathrm{s}}\left(\mathbf{J}_s\right) + \mathbf{H}^{\mathrm{s}}(\mathbf{J}_v^D) + \mathbf{H}^{\mathrm{s}}(\mathbf{J}_v^M), \quad \text{in V} \quad (4)$$

where $\mathbf{E}$ and $\mathbf{H}$ are the total electrical field and magnetic field. $\mathbf{E}^s\left(\mathbf{J}_s\right)$ and $\mathbf{H}^s\left(\mathbf{J}_s\right)$ are the scattered electric and magnetic field due to the surface polarization current $\mathbf{J}_s$ on the conducting surface. $\mathbf{E}^s\left(\mathbf{J}_v^t\right)$ and $\mathbf{H}^s\left(\mathbf{J}_v^t\right)\left(t = D, M\right)$ are the scattered electric and magnetic fields due to the volume polarization current $\mathbf{J}_v^t$ in the medium. Equations (3) and (4) are volume-integral equations (VIE), and equation (2) by setting the tangential electric field to zero on the conducting surface is the electric field surface-integral equation (SIE), these three equations constitute the coupled volume-surface integral equations (VSIE), which will be used for the numerical solution in this work.

The surface current $\mathbf{J}_s$ on S can be represented by vector basis functions RWG [13], namely

$$\mathbf{J}_s \approx \sum_{n=1}^{N_s} I_{s,n}^J \mathbf{f}_{s,n}(\boldsymbol{r}), \qquad \boldsymbol{r} \in S \qquad (5)$$

where $I_{s,n}^J$ is the unknown expansion coefficient, $\mathbf{f}_{s,n}$ represents the nth face basis function for the nth common edge and N_s is the total number of the common edges.

The volume electric current $\mathbf{J}_v^{\mathrm{D}}$ and magnetic current $\mathbf{J}_v^{\mathrm{M}}$ within V can be then expressed by vector basis function SWG [14] as

$$\mathbf{J}_v^M = \sum_{n=1}^{N_v} I_{v,n}^M \overline{\overline{\kappa}}^m(\mathbf{r}) \cdot \left(\eta_0 \mathbf{f}_{v,n}(\mathbf{r})\right), \qquad \mathbf{r} \in V \qquad (6)$$

$$\mathbf{J}_v^M = \sum_{n=1}^{N_v} I_{v,n}^M \overline{\overline{\kappa}}^m(\mathbf{r}) \cdot \left(\eta_0 \mathbf{f}_{v,n}(\mathbf{r})\right), \qquad \mathbf{r} \in V \qquad (7)$$

where $I_{v,n}^D$ and $I_{v,n}^M$ are the unknown expansion coefficients for the electric and magnetic currents in the dielectric volume, respectively. $\mathbf{f}_{v,n}$ denotes the basis function for the nth face of the tetrahedral model of V, and N_v is the number of common faces. $\overline{\overline{\kappa}}^e(\mathbf{r})$ and $\overline{\overline{\kappa}}^m(\mathbf{r})$ are the contrast ratio tensor defined by

$$\overline{\overline{\kappa}}^e(\mathbf{r}) = (\overline{\overline{\varepsilon}}_r - \overline{\overline{I}}) \cdot \overline{\overline{\varepsilon}}_r^{-1}, \qquad (8)$$

$$\overline{\overline{\kappa}}^m(\mathbf{r}) = (\overline{\overline{\mu}}_r - \overline{\overline{I}}) \cdot \overline{\overline{\mu}}_r^{-1}. \qquad (9)$$

It's necessary to note that the introduction of wave impedance η_0 is to achieve well conditioned systems and accurate solutions.

Using the extended Galerkin's method and substituting the equations (5), (6), and (7) into (2), (3), and (4), respectively, we can test (2) with the surface basis function $\mathbf{f}_{s,m}$, (3) with the volume basis function $\mathbf{f}_{v,m}$, and (4) with the volume basis function $\eta_0 \mathbf{f}_{v,m}$. And finally a linear system consisting of $N_s + 2N_v$ independent equations is obtained, which can be written in a matrix form as

$$\begin{bmatrix} \boldsymbol{Z}^{JJ} & \boldsymbol{Z}^{JD} & \eta_0 \boldsymbol{Z}^{JM} \\ \boldsymbol{Z}^{DJ} & \boldsymbol{Z}^{DD} & \eta_0 \boldsymbol{Z}^{DM} \\ \eta_0 \boldsymbol{Z}^{MJ} & \eta_0 \boldsymbol{Z}^{MD} & \eta_0{}^2 \boldsymbol{Z}^{MM} \end{bmatrix} \begin{bmatrix} \boldsymbol{I}^J \\ \boldsymbol{I}^D \\ \boldsymbol{I}^M \end{bmatrix} = \begin{bmatrix} \boldsymbol{V}^J \\ \boldsymbol{V}^D \\ \eta_0 \boldsymbol{V}^M \end{bmatrix}, \quad (10)$$

where $\boldsymbol{Z}^{JJ}$, $\boldsymbol{Z}^{JD}$, $\boldsymbol{Z}^{JM}$, $\boldsymbol{Z}^{DJ}$, $\boldsymbol{Z}^{DD}$, $\boldsymbol{Z}^{DM}$, $\boldsymbol{Z}^{MJ}$, $\boldsymbol{Z}^{MD}$, and $\boldsymbol{Z}^{MM}$ are the impedance sub-matrices with the dimension of $N_s \times N_s$, $N_s \times N_v$, $N_s \times N_v$, $N_v \times N_s$, $N_v \times N_v$, $N_v \times N_v$, $N_v \times N_s$, $N_v \times N_v$ and $N_v \times N_v$. $\boldsymbol{I}^J$ is the column vector of length N_s, while $\boldsymbol{I}^D$ and $\boldsymbol{I}^M$ are column vectors of length N_v. Similarly, $\boldsymbol{V}^J$ is the column vector of length N_s, while $\boldsymbol{V}^D$ and $\boldsymbol{V}^M$ are column vectors of length N_v. Then, we can obtain the entries of the impendence matrix blocks as

$$Z_{mn}^{JJ} = -<\mathbf{f}_{s,m}, \mathbf{E}^s\left(\mathbf{f}_{s,n}\right)>, \ m,n = 1,2\cdots N_s, \tag{11}$$

$$Z_{mn}^{JD} = -<\mathbf{f}_{s,m}, \mathbf{E}^s\left(\overline{\overline{\kappa}}^e \cdot \mathbf{f}_{v,n}\right)>, \ m = 1,2\cdots N_s, \quad n = 1,2\cdots N_v, \tag{12}$$

$$Z_{mn}^{JM} = -<\mathbf{f}_{s,m}, \mathbf{E}^s\left(\overline{\overline{\kappa}}^m \cdot \mathbf{f}_{v,n}\right)>, \ m = 1,2\cdots N_s, \quad n = 1,2\cdots N_v, \tag{13}$$

$$Z_{mn}^{DJ} = -<\mathbf{f}_{v,m}, \mathbf{E}^s\left(\mathbf{f}_{s,n}\right)>, \quad m = 1,2,\cdots N_v, \quad n = 1,2,\cdots N_s, \tag{14}$$

$$Z_{mn}^{DD} = <\mathbf{f}_{v,m}, \frac{\overline{\overline{\varepsilon}}_r^{-1} \cdot \mathbf{f}_{v,n}}{j\omega\varepsilon_0}> - <\mathbf{f}_{v,m}, \mathbf{E}^s\left(\overline{\overline{\kappa}}^e \cdot \mathbf{f}_{v,n}\right)>, \quad m,n = 1,2,\cdots N_v, \tag{15}$$

$$Z_{mn}^{DM} = -<\mathbf{f}_{v,m}, \mathbf{E}^s\left(\overline{\overline{\kappa}}^m \cdot \mathbf{f}_{v,n}\right)>, \ m,n = 1,2,\cdots N_v, \tag{16}$$

$$Z_{mn}^{MJ} = -<\mathbf{f}_{v,m}, \mathbf{H}^s\left(\mathbf{f}_{s,n}\right)>, \quad m = 1,2,\cdots N_v, \quad n = 1,2,\cdots N_s, \tag{17}$$

$$Z_{mn}^{MD} = -<\mathbf{f}_{v,m}, \mathbf{H}^s\left(\overline{\overline{\kappa}}^e \cdot \mathbf{f}_{v,n}\right)>, \ m,n = 1,2,\cdots N_v, \tag{18}$$

$$Z_{mn}^{MM} = <\mathbf{f}_{v,m}, \frac{\overline{\overline{\mu}}_r^{-1} \cdot \mathbf{f}_{v,n}}{j\omega\mu_0}> - <\mathbf{f}_{v,m}, \mathbf{H}^s\left(\overline{\overline{\kappa}}^m \cdot \mathbf{f}_{v,n}\right)>, \quad m,n = 1,2,\cdots N_v. \tag{19}$$

The excitation column entries contain the following integrals:

$$V_m^J = \int_S dS\mathbf{f}_{s,m} \cdot \mathbf{E}^{\mathrm{i}}, \tag{20}$$

$$V_m^D = \int_V dV\mathbf{f}_{v,m} \cdot \mathbf{E}^{\mathrm{i}}, \tag{21}$$

$$V_m^M = \int_V dV\mathbf{f}_{v,m} \cdot \mathbf{H}^{\mathrm{i}}. \tag{22}$$

B. The application of EDM to accelerate the MOM

The conducting surface S is first meshed into triangles and each triangle pair can be represented by a RWG element, the medium V can also be discretized into tetrahedrons and each tetrahedron pair can be represented by a SWG element. The nth face electric dipole moment $\mathbf{m}_n^J$ corresponds to a pair of triangle patches, the nth volume electric dipole moment $\mathbf{m}_n^D$ corresponds to tetrahedrons and their scattered fields can be found in [12]. The nth volume magnetic dipole moment can be written as

$$\mathbf{m}_n^M = \begin{cases} a_{v,n}\overline{\overline{\kappa}}^m \bullet (\mathbf{r}_{v,n}^{c-} - \mathbf{r}_{v,n}^{c+}) & T_{v,n}^{\pm} \in V \\ a_{v,n}\overline{\overline{\kappa}}^m \bullet (\mathbf{r}_{ns}^{c} - \mathbf{r}_{v,n}^{c+}) & T_{v,n}^{+} \in V \text{ and } T_{v,n}^{-} \notin V \end{cases}. \tag{23}$$

Here, $\mathbf{r}_{v,n}^{c\pm}$ and $\mathbf{r}_{ns}^{c}$ are the centroid radius vector of a pair of tetrahedrons $T_{v,n}^{\pm}$ and the *n*th boundary face, respectively. $a_{v,n}$ is the area of the common face associated with $T_{v,n}^{\pm}$ or the area of the *n*th boundary face associated with $T_{v,n}^{+}$. Referring to [12] and electric-magnetic duality, the scattered fields of the nth infinitesimal magnetic dipole at the centroid radius vector $\mathbf{r}_{u,m}\left(u = s,v\right)$ are

$$\mathbf{E}^s\left(\mathbf{m}_n^M\right) = -\frac{jk}{4\pi}\left(\mathbf{m}_n^M \times \mathbf{R}\right)C\,e^{-jkR}\Big|_{R=\left|\mathbf{r}_{u,m}-\mathbf{r}'_{v,n}\right|}, \tag{24}$$

$$\mathbf{H}^s\left(\mathbf{m}_n^M\right) = \frac{1}{4\pi\eta}\left[\left(\mathbf{M}_n^M - \mathbf{m}_n^M\right)\left(\frac{jk}{R} + C\right) + 2\mathbf{M}_n^M C\right]e^{-jkR}\Big|_{R=\left|\mathbf{r}_{u,m}-\mathbf{r}'_{v,n}\right|}, \tag{25}$$

where $\boldsymbol{r}_{u,m}$ and $\boldsymbol{r}'_{v,n}$ are the center radius vectors of the *m*th and the *n*th equivalent dipole model, respectively.

$$C = \frac{1}{R^2}\left[1 + \frac{1}{jkR}\right] \tag{26}$$

and

$$\mathbf{M}_n^M = \frac{\left(\mathbf{R} \cdot \mathbf{m}_n^M\right)\mathbf{R}}{R^2}. \tag{27}$$

Here, $\mathbf{R} = \mathbf{r}_{u,m} - \mathbf{r}'_{v,n}$ and $R = \left|\mathbf{R}\right|$. Equations (24) and (25) are the exact expressions and valid at arbitrary distances from the dipole. Considering the accuracy and efficiency of the algorithm, the critical distance between the source and the testing function locations is chosen as $0.15\lambda_g$, where λ_g is the wavelength in dielectric body [11-12]. The MOM matrix elements are computed by the EDM method directly for a separation distance of greater than the critical distance. Substituting (24) into (13) and (16), (25) into (17)-(19), and associated with paper [12], the expressions of the impedance matrix elements are calculated by

$$Z_{mn}^{JJ} = -l_{s.m}\mathbf{E}^s(\mathbf{m}_n^J) \cdot (\mathbf{r}_{s,m}^{c-} - \mathbf{r}_{s,m}^{c+}), \quad T_{s,m}^{\pm} \in S \tag{28}$$

$$Z_{mn}^{JD} = -l_{s.m}\mathbf{E}^s(\mathbf{m}_n^D) \cdot (\mathbf{r}_{s,m}^{c-} - \mathbf{r}_{s,m}^{c+}), \quad T_{s,m}^{\pm} \in S \tag{29}$$

$$Z_{mn}^{JM} = -l_{s.m}\mathbf{E}^s(\mathbf{m}_n^M) \cdot (\mathbf{r}_{s,m}^{c-} - \mathbf{r}_{s,m}^{c+}), \quad T_{s,m}^{\pm} \in S \tag{30}$$

$$Z_{mn}^{DJ}=\begin{cases}-a_{v,m}\mathbf{E}^{s}(\mathbf{m}_{n}^{J})\cdot(\mathbf{r}_{v,m}^{c-}-\mathbf{r}_{v,m}^{c+}) & T_{v,m}^{\pm}\in V\\ -a_{v,m}\mathbf{E}^{s}(\mathbf{m}_{n}^{J})\cdot(\mathbf{r}_{ms}^{c-}-\mathbf{r}_{v,m}^{c+}), & T_{v,m}^{+}\in V \text{ and } T_{v,m}^{-}\notin V\end{cases} \tag{31}$$

$$Z_{mn}^{DD}=\begin{cases}-a_{v,m}\mathbf{E}^{s}(\mathbf{m}_{n}^{D})\cdot(\mathbf{r}_{v,m}^{c-}-\mathbf{r}_{v,m}^{c+}) & T_{v,m}^{\pm}\in V\\ -a_{v,m}\mathbf{E}^{s}(\mathbf{m}_{n}^{D})\cdot(\mathbf{r}_{ms}^{c-}-\mathbf{r}_{v,m}^{c+}), & T_{v,m}^{+}\in V \text{ and } T_{v,m}^{-}\notin V\end{cases} \tag{32}$$

$$Z_{mn}^{DM}=\begin{cases}-a_{v,m}\mathbf{E}^{s}(\mathbf{m}_{n}^{M})\cdot(\mathbf{r}_{v,m}^{c-}-\mathbf{r}_{v,m}^{c+}) & T_{v,m}^{\pm}\in V\\ -a_{v,m}\mathbf{E}^{s}(\mathbf{m}_{n}^{M})\cdot(\mathbf{r}_{ms}^{c-}-\mathbf{r}_{v,m}^{c+}), & T_{v,m}^{+}\in V \text{ and } T_{v,m}^{-}\notin V\end{cases} \tag{33}$$

$$Z_{mn}^{MJ}=\begin{cases}-a_{v,m}\mathbf{H}^{s}(\boldsymbol{m}_{n}^{J})\cdot(\mathbf{r}_{v,m}^{c-}-\mathbf{r}_{v,m}^{c+}) & T_{v,m}^{\pm}\in V\\ -a_{v,m}\mathbf{H}^{s}(\boldsymbol{m}_{n}^{J})\cdot(\mathbf{r}_{ms}^{c-}-\mathbf{r}_{v,m}^{c+}), & T_{v,m}^{+}\in V \text{ and } T_{v,m}^{-}\notin V\end{cases} \tag{34}$$

$$Z_{mn}^{MD}=\begin{cases}-a_{v,m}\mathbf{H}^{s}(\boldsymbol{m}_{n}^{D})\cdot(\mathbf{r}_{v,m}^{c-}-\mathbf{r}_{v,m}^{c+}) & T_{v,m}^{\pm}\in V\\ -a_{v,m}\mathbf{H}^{s}(\boldsymbol{m}_{n}^{D})\cdot(\mathbf{r}_{ms}^{c-}-\mathbf{r}_{v,m}^{c+}), & T_{v,m}^{+}\in V \text{ and } T_{v,m}^{-}\notin V\end{cases} \tag{35}$$

$$Z_{mn}^{MM}=\begin{cases}-a_{v,m}\mathbf{H}_{n}^{s}(\boldsymbol{m}_{n}^{M})\cdot(\mathbf{r}_{v,m}^{c-}-\mathbf{r}_{v,m}^{c+}) & T_{v,m}^{\pm}\in V\\ -a_{v,m}\mathbf{H}_{n}^{s}(\boldsymbol{m}_{n}^{M})\cdot(\mathbf{r}_{ms}^{c-}-\mathbf{r}_{v,m}^{c+}), & T_{v,m}^{+}\in V \text{ and } T_{v,m}^{-}\notin V\end{cases} \tag{36}$$

where $l_{s.m}$ is the length of m^{th} common edge associated with a pair of triangle patches $T_{s,m}^{\pm}$ and $\mathbf{r}_{s,m}^{c\pm}$ is the centroid radius vector of $T_{s,m}^{\pm}$ [12].

Equations (28)-(36) are universal that it is unnecessary to treat the boundary condition on the surface of the mixed body, so the EDM method can be constructed by using a simple procedure and the impedance matrix's generation is very efficient. From the above equations, it can be concluded that the EDM method has two advantages over the conventional MOM: one is that the EDM method does not require evaluating the usual integrals involving the expansion and testing functions, thus reducing the computational complexity. Another is the reduction of the computation time for the calculations of each impedance matrix element, which can be obtained by one multiplication in the EDM method, while four multiplications in the conventional MOM using 1-point integration algorithm.

III. NUMERICAL RESULTS

In this section, three numerical results are presented to validate the algorithm and demonstrate the efficiency of the method. We remark that all the simulations are solved on a processor with 2.2GHz dual CPU speed. All coated structures are excited by a plane wave with the frequency of 0.3 GHz propagating along the –z direction.

In the first example, we consider a coated sphere shown in Fig. 2, where the electric dimension of the inner and outer spherical radius is $k_0a_1=0.2\pi$ and $k_0a_2=0.3\pi$, respectively, while the relative tensor elements of the uniaxial anisotropic material are $\varepsilon_{xx}=\varepsilon_{yy}=1.5-0.5j$, $\varepsilon_{zz}=2-j$, and $\mu_{xx}=\mu_{yy}=1.5-0.5j$, $\mu_{zz}=2-j$, the others are zero. The curves of Fig. 2 clearly show that the bistatic RCSs calculated in three different ways (the EDM method, the conventional MOM, HFSS) are in good agreement in both the xoz-plane and yoz-plane, thus validating the correctness and applicability of our method and the code.

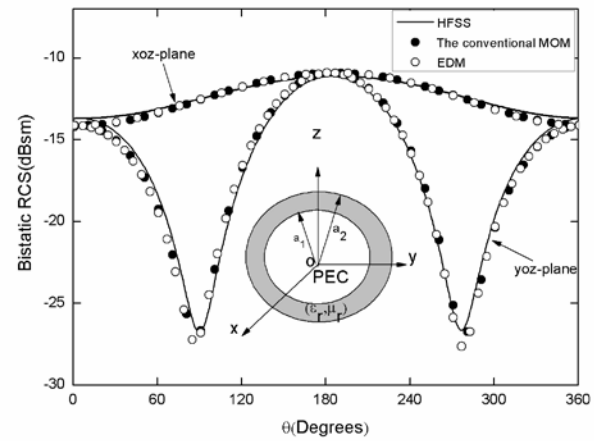

Fig. 2. Bistatic RCS of a conducting sphere coated with anisotropic uniaxial material.

Then, we consider a conducting sheet, which is coated with two-layer anisotropic materials. The relative tensor elements of the first layer sub1 are $\varepsilon_{xx}=\varepsilon_{yy}=1.5$, $\varepsilon_{zz}=2$, $\varepsilon_{xy}=j$, $\varepsilon_{yx}=-j$ and $\mu_{xx}=\mu_{yy}=\mu_{zz}=2-j$ and the others are zero. The relative tensor elements of the second layer sub2 are $\varepsilon_{xx}=\varepsilon_{yy}=\varepsilon_{zz}=2-j$ and $\mu_{xx}=\mu_{yy}=1.5$, $\mu_{zz}=2$, $\mu_{xy}=j$, $\mu_{yx}=-j$ and the others are zero. The configuration and its geometrical parameters are W=L=0.5m, $H_1=H_2=0.05$m, shown in Fig. 3. We remark here that the magnetic current unknowns could be paired with their corresponding electric current unknowns, thus resulting in total 6214 unknowns. The results of MOM are plotted in solid line, and the results of EDM are plotted in dotted line. It is observed that the results of the EDM method agree well with those of the conventional MOM, shown in Fig. 3. The total CPU time is 2249 seconds for EDM method and 4644 seconds for conventional method, respectively, which yields a reduction of 51.6% of the total computation time.

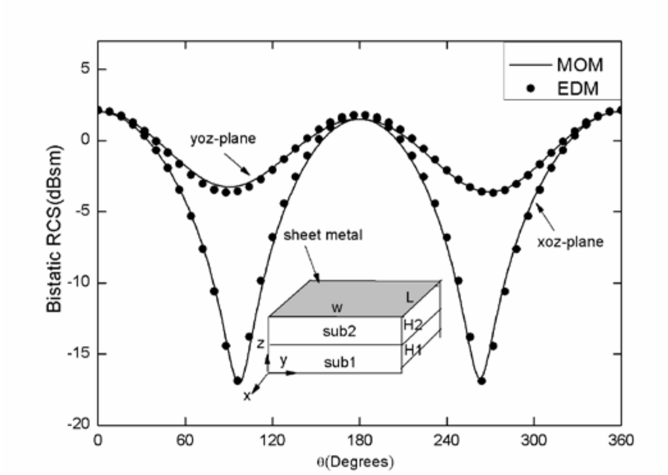

Fig. 3. Bistatic RCS of a metallic sheet coated with two-layer anisotropic off-diagonal materials.

In the last example, we consider the scattering from a coated connecting-ring, which is shown in Fig. 4 (a), and the geometrical parameters are D_1=100mm, D_2=150mm, D_3=200mm, D_4=500mm, H=500mm. The material of the coated layer of the model is uniaxial anisotropic lossy material with the relative tensors $\varepsilon_{xx} = \varepsilon_{yy} = 2 - j$, $\varepsilon_{zz} = 1.5 - 0.75j$ and $\mu_{xx} = \mu_{yy} = 1.5 - 0.75j$, $\mu_{zz} = 2 - j$, the others are zero. The unknowns (including triangles for perfect conductor and tetrahedrons for dielectric material) are 7011 in all. The RCS of the metallic connecting-ring coated with material is computed by both the conventional MOM (dashed line) and the EDM (dotted line), as shown in Fig. 4 (b) and (c), their results are in good agreement with each other. The total CPU time is 36915 seconds for conventional method and 24361 seconds for EDM method, respectively, which yields a reduction of 34% of the total computation time. We can also see from Fig. 4 (b) and (c), the presence of the uniaxial lossy material leads to the reduction of RCS in both xoz-plane and yoz-plane polarization in the scattering angle from 0° to 90° and 270° to 360° be about 7 dB lower than those of the metallic connecting-ring without coating material (solid line).

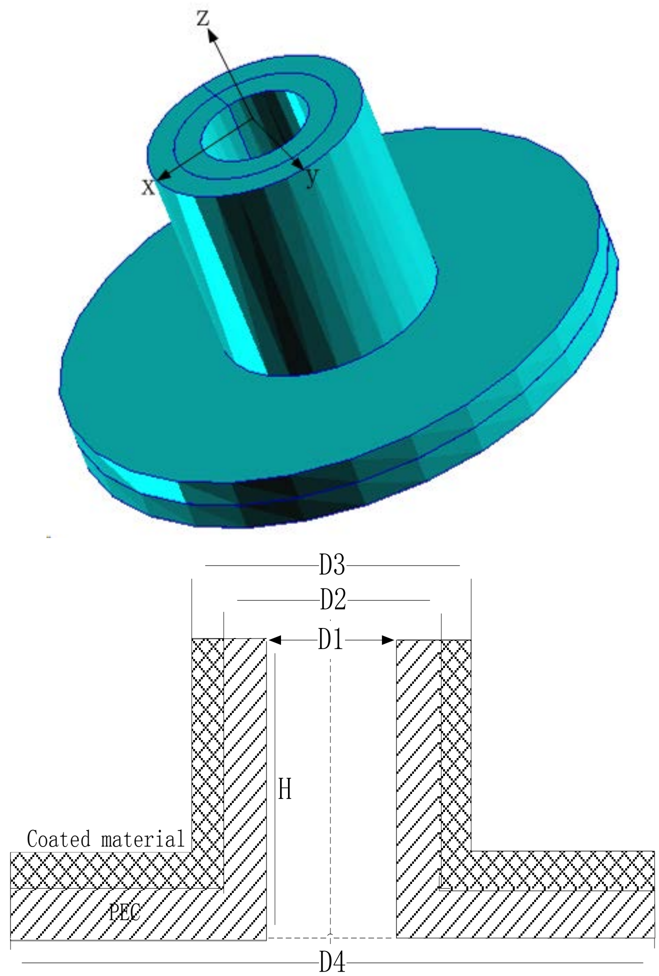

(a)

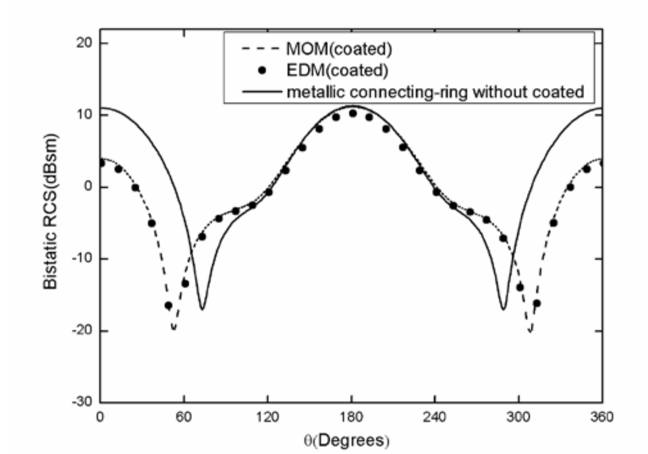

(b)

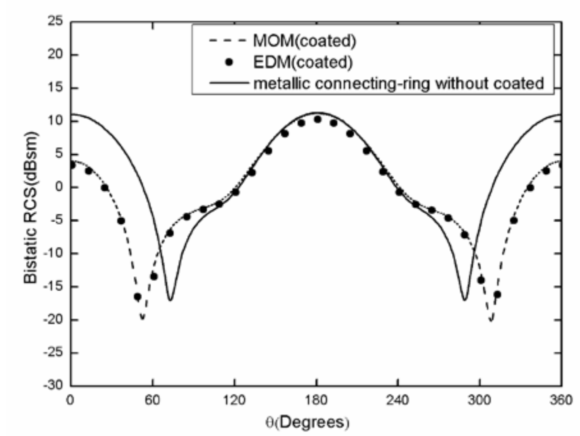

(c)

Fig. 4. (a) The connect-ring and its corresponding geometrical parameters, (b) bistatic RCS (xoz-plane) of a connecting-ring non-coated and coated with uniaxial material, (c) bistatic RCS (yoz-plane) of a connecting-ring non-coated and coated with uniaxial material.

IV. CONCLUSION

In this work, the EDM method has been successfully extended and applied in the analysis of the EM scattering characteristics of arbitrarily shaped PEC targets coated with arbitrary electric and magnetic anisotropic media. The application of the EDM method significantly reduces the computational complexity of the impedance matrix as well as the CPU time. All in all, the algorithm presented in this paper can be applied to analyze arbitrary shaped complex target coated with arbitrary thickness of EM anisotropic materials. In future work, we will focus on the application of the EDM method for the computation of the RCS of arbitrary shaped targets coated with bi-anisotropic materials.

ACKNOWLEDGMENT

The authors are grateful to Zhuo Li, Xinlei Chen and Ji Ding at College of Information Science and Technology, Nanjing University of Aeronautics and Astronautics, China, for their helpful suggestions and support during the project. The authors also gratefully acknowledge the support of the Joint Funding projects of the Aerospace Science Foundation Office of China and Nanjing University of Aeronautics and Astronautics (2008ZA52006).

REFERENCES

[1] Yin Hongcheng, Huang Peikang, and Liu Xueguan, “PO Solution for Scattering by the Complex Object Coated with Anisotropic Materials J-J,” *Journal of Systems Engineering and Electronics*, vol. 14, no. 2, pp.1-7, 2003.

[2] Z. Ruili, M. Zhizhou, L. Zha, et al., “FDTD Analysis of Wide-Band Scatting Characteristic of Metal Target Coated by Anisotropic Medium,” *Chinese Journal of Radio Science*, vol. 23, no. 1, pp. 11-16, 2008.

[3] Z. Xiuqin, G. Youlin, and W. Xinbao, “Application of MOM-CGM-FFT Method to Scattering from Three-Dimensional Magnetic Anisotropic Scatterers,” *Journal of microwave*, vol. 18, no. 3, pp. 7-13, June 2002.

[4] J. J. Angelin, “Hybrid Numerical Method for Harmonic 3-D Maxwell Equations: Scattering by a Mixed Conducting and Inhomogeneous Anisotropic Dielectric Medium [J],” *IEEE Transactions on Antennas and Propagation*, vol. 41, no. 1, pp. 66-76, 1993.

[5] G. Kobidze and B. Shanker, “Integral Equation Based Analysis of Scattering from 3-D Inhomogeneous Anisotropic Bodies,” *IEEE Transactions on Antennas and Propagation*, vol. 52, no. 10, pp. 2650-2658, October 2004.

[6] C. C. Su, “Electromagnetic Scattering by Dielectric Body with Arbitrary Inhomogeneity and Anisotropy,” *IEEE Transactions on Antennas and Propagation*, vol. 37, no. 3, pp. 384-389, March 1989.

[7] H. A. Sabbagh, R. K. Murphy, E. H. Sabbagh, et al., “The Joy of Computing with Volume Integrals: Foundations for Nondestructive Evaluation of Planar Layered Media,” *Applied Computational Electromagnetic Society (ACES) Journal*, vol. 25, no. 9, pp. 723-730, September 2010.

[8] C. Luo and C.-C. Lu, “Electromagnetic Scattering Computation Using a Hybrid Surface and Volume Integral Equation Formulation,” *Applied Computational Electromagnetic Society (ACES) Journal*, vol. 22, no. 3, pp. 340-349, November 2007.

[9] A. W. Glisson, M. Orman, F. Falco, et al., “Electromagnetic Scattering by an Arbitrarily Shaped Surface with an Anisotropic Impedance Boundary Condition,” *Applied Computational Electromagnetic Society (ACES) Journal*, vol. 10, no. 3, pp. 93-106, 1995.

[10] A. A. Kishk and P.-S. Kildal, “Electromagnetic Scattering from Two Dimensional Anisotropic Impedance Objects under Oblique Plane Wave Incidence,” *Applied Computational Electromagnetic Society (ACES) Journal*, vol. 10, no. 3, pp. 81-92, 1995.

[11] J. Yuan, C. Gu, and G. Han, “Efficient Generation of Method of Moments Matrices Using Equivalent Dipole-Moment Method,” *IEEE Antennas and Wireless Propagation Letters*, vol. 8, pp. 716-719, 2009.

[12] J. Yuan, Z. Niu, Z. Li, et al., “Electromagnetic Scattering by Arbitrarily Shaped PEC Targets Coated with Anisotropic Media using Equivalent Dipole-Moment Method,” *J Infrared Milli Terahz Waves*, vol. 31, no. 6, pp. 744–752, 2010.

[13] S. M. Rao, D. R. Wilton, and A. W. Glisson, “Electromagnetic Scattering by Surfaces of Arbitrary Shape,” *IEEE Transactions on Antennas and Propagation*, vol. AP-30, no. 3, pp. 409-418, May 1982.

[14] D. H. Schaubert, D. R. Wilton, and A. W. Glisson, “A Tetrahedral Modeling Method for Electromagnetic Scattering by Arbitrarily Shaped Inhomogeneous Dielectric Bodies,” *IEEE Transactions on Antennas and Propagation*, vol. AP-32, no. 1, pp. 77-85, January 1984.

Scattering Pattern Calculation for Large Finite Arrays using the Element-Varying Active Element Factor Method

Qifei Li, Wei Shao, and Hua Li

Institute of Applied Physics
University of Electronic Science and Technology of China, Chengdu, China
E-mail: qifei_li@163.com, weishao@uestc.edu.cn, and lihua2006@uestc.edu.cn

Abstract **─** In this paper, an efficient approach for calculating the far field pattern of one-dimensional (1-D) and two-dimensional (2-D) finite patch arrays is proposed. Based on the active element factor (AEF) defined specifically for scattering problems, this proposed method takes into account the effects of mutual couplings and array edges. From the induced current distribution on an array with odd or even elements, the array is divided into different parts and neglects the weak mutual coupling affected by far elements for each part. Thus, the element-varying AEF method changes a large array problem into a superposition of various simplified subarray problems. Three examples verify the accuracy and efficiency of the proposed method. Furthermore, the results show that the proposed method with the element-varying AEF technique has the ability to solve the scattering problems of rather large arrays whereas other methods become incapable due to computer hardware limitations.

Index Terms **─** Active element factor, far field pattern, mutual coupling, subarray.

I. INTRODUCTION

Numerical methods, such as the method of moments (MoM) [1], finite element method (FEM) [2], finite-difference time-domain (FDTD) method [3], multilevel fast multipole algorithm (MLFMA) [4], characteristic basis function method (CBFM) [5], and hybrid methods [6] are employed to calculate the electromagnetic scattering. Direct numerical simulations for a small array mounted on an arbitrary platform result in an accurate and effective solution. For an infinite periodic array, only an element is required to be extracted for calculation with the Floquet's theorem or periodic Green function [7-8]. The numerical methods, however, become inefficient or even infeasible for rather large finite arrays when considering the mutual coupling effects in the whole array environment because of the computer hardware limitations. In this case, approximate methods are needed to reduce the large memory and time requirement for the array calculation and analysis.

Over the past years, an active element pattern (AEP) technique was used for prediction of the performance of large array antennas [9-11]. With the pattern taken with a feed at a single element in the array and all other elements terminated in matched loads, the AEP technique considers mutual coupling effects between array elements and expresses the radiated pattern effectively and efficiently. From the AEP theorem, the active element factor (AEF) defined as the current distribution induced on a particular aperture is intended for scattering problems [12-13]. In [13], an average AEF with the reduced window array (RWA) approximation is introduced to analyze the scattering characteristics of finite arrays in an infinite ground plane.

In this paper, the scattering performance of finite patch arrays in a finite ground plane is studied with an element-varying AEF method. Due to the finite grounds in this study, the induced current distribution on an array with odd elements is quite different from that with even elements. Based on the element-varying AEF method, this paper presents how an array is divided into various subarrays according to the induced current distribution. The whole array elements are divided into edge elements, interior elements, and adjacent edge elements. The AEFs of edge elements can be approximated by a small subarray when neglecting

Submitted On: July 28, 2011
Accepted On: Dec. 18, 2011

the weak mutual coupling affected by far elements. The similar subarrays are also applied to AEFs of interior elements and adjacent edge elements. Thus, the far field pattern of a rather large finite array can be calculated by a superposition of these three types of the element-varying AEF from a subarray. After the current distribution of a small array is quickly gotten with the commercial software FEKO [14], the varied AEFs of each element in a subarray can easily be obtained to calculate the far field scattering pattern of a rather large array. The element-varying AEF method can greatly reduce the computing time and simplify the operational procedure. The one-dimensional (1-D) and two-dimensional (2-D) examples show that the results are actually quite good over a broad angular range and only deteriorate for angles that approach grazing.

II. THEORIES

A. Far electric field pattern of a finite array

The far electric field scattered by an array can be expressed as

$$\boldsymbol{E}_{\text{total}} = \sum_{n=1}^{N} \boldsymbol{E}_n\left(\theta,\varphi\right), \tag{1}$$

where $\boldsymbol{E}_n$ is the far electric field scattered by the nth element aperture with an entire array illuminated by an incident wave source. Induced currents on each element aperture are excited by the incident wave and contain all the effects of the mutual coupling and the array environment. Using the equivalence principle, $\boldsymbol{E}_n$ can be written as

$$\begin{aligned}\boldsymbol{E}_n(\boldsymbol{J},\boldsymbol{M}) = &-\frac{j\omega\mu}{4\pi}\int_s \boldsymbol{J}\frac{e^{-jk|\boldsymbol{r}-\boldsymbol{r}'|}}{|\boldsymbol{r}-\boldsymbol{r}'|}ds' \\ &+\frac{1}{4\pi \mathrm{j}\omega\varepsilon}\nabla\int_s \nabla'\cdot\boldsymbol{J}\frac{e^{-jk|\boldsymbol{r}-\boldsymbol{r}'|}}{|\boldsymbol{r}-\boldsymbol{r}'|}ds', \\ &-\frac{1}{4\pi}\nabla\times\int_s \boldsymbol{M}\frac{e^{-jk|\boldsymbol{r}-\boldsymbol{r}'|}}{|\boldsymbol{r}-\boldsymbol{r}'|}ds'\end{aligned} \tag{2}$$

where $\boldsymbol{r}$ and $\boldsymbol{r}'$ are the position vectors of the observation and source points with respect to a global coordinate, the electric current $\boldsymbol{J}$ consists of $\boldsymbol{J}_{\text{c}}$ and $\boldsymbol{J}_{\text{d}}$ which are the equivalent surface electric currents induced on the conducting and dielectric surfaces of the nth element aperture, and the magnetic current $\boldsymbol{M}$ is the equivalent surface magnetic current induced on the dielectric surface of the nth element aperture.

In this study, $\boldsymbol{J}_{\text{c}}$, $\boldsymbol{J}_{\text{d}}$ and $\boldsymbol{M}$ can be gotten with the commercial software FEKO, which is a powerful and convenient tool. The current information is stored in *.os file and mesh information in *.stl file after the MoM-based simulation of FEKO. Thus, $\boldsymbol{E}_n$ can be easily calculated by applying the corresponding current and mesh data to equation (2).

B. Element-varying AEF method

Figure 1 plots a 1-D homogeneous finite periodic array illuminated by a plane wave source. Currents are induced on the structure. Besides the mutual couple effects, there are edge effects introduced by the bounded nature of the finite array [15-16]. Since the currents induced on each element are varied, all $\boldsymbol{E}_n$ are needed to be calculated from (2) to complete the superposition of all elements' scattering patterns in (1).

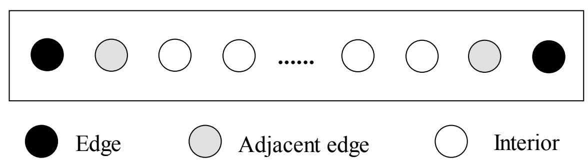

Fig. 1. 1-D finite periodic array and its elements.

Considering the element-varying AEF scheme, a fast approximation is proposed to obtain the accurate scattering performance in this paper. Once knowing the currents induced on a small array with the numerical simulation, the far field pattern of a rather large finite array can be easily calculated.

Generally, all elements of an array are divided into edge elements, interior elements, and adjacent edge elements, as shown in Figure 1. Equation (1) can therefore be rewritten as [16]

$$\boldsymbol{E}_{\text{total}} = \boldsymbol{E}_{\text{E}}\left(\theta,\varphi\right)+\boldsymbol{E}_{\text{I}}\left(\theta,\varphi\right)+\boldsymbol{E}_{\text{AE}}\left(\theta,\varphi\right), \tag{3}$$

$$\boldsymbol{E}_{\text{E}} = \sum_{e=1}^{Ne}\boldsymbol{E}_e\left(\theta,\varphi\right)e^{jk\hat{\boldsymbol{r}}\bullet\boldsymbol{r}_e}, \tag{4}$$

$$\boldsymbol{E}_{\text{I}} = \sum_{i=1}^{Ni}\boldsymbol{E}_i\left(\theta,\varphi\right)e^{jk\hat{\boldsymbol{r}}\bullet\boldsymbol{r}_i}, \tag{5}$$

$$\boldsymbol{E}_{\text{AE}} = \sum_{a=1}^{Na}\boldsymbol{E}_a\left(\theta,\varphi\right)e^{jk\hat{\boldsymbol{r}}\bullet\boldsymbol{r}_a}, \tag{6}$$

where $\boldsymbol{E}_{\text{E}}$, $\boldsymbol{E}_{\text{I}}$ and $\boldsymbol{E}_{\text{AE}}$ are the superposition of AEP of all edge elements, all interior elements and all adjacent edge elements, respectively. N_{e}, N_{i}

and N_a are the numbers of all edge elements, all interior elements and all adjacent edge elements, respectively. $\boldsymbol{E}_e(\theta,\varphi)$, $\boldsymbol{E}_i(\theta,\varphi)$ and $\boldsymbol{E}_a(\theta,\varphi)$ are obtained from the local subarrays, respectively. $e^{jk\hat{\boldsymbol{r}}\bullet\boldsymbol{r}_e}$ is the spatial phase factor, where $\hat{\boldsymbol{r}}$ is the unit radius vector from the origin to the observation, and $\boldsymbol{r}_n$ (n=e, i, a) is a position vector from the origin to the center of the nth element.

C. Arrays with odd and even elements

In the light of boundary condition and symmetry influence, the induced current distribution on an array with odd elements is quite different from that with even elements. In order to calculate AEFs of a rather large array from those of a small array accurately, it is required to calculate the two cases of odd elements and even elements, separately.

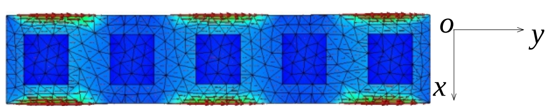

(a) 1-D 5-element array

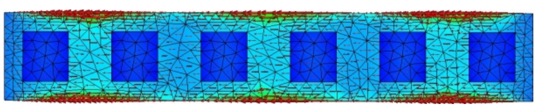

(b) 1-D 6-element array

Fig. 2. Current density on odd-element and even-element arrays. (Arrows denote current densities.)

For example, Fig. 2 shows the induced current density on two finite patch arrays with five (odd) elements and six (even) elements from the FEKO simulation. The elements of the 1-D patch array are uniformly placed along the y-axis. And the two arrays are respectively illuminated by a vertical incident plane wave with y polarization. For the two cases, the symmetrical structure and the vertical plane wave source result in a symmetrical induced current distribution. However, the symmetry line along the y-direction of the odd-element array passes through one patch, but it is between two patches for the even-element array. The two different boundary conditions lead to the separate analysis of the odd-element array and even-element array. From Fig. 2, it can be seen that the current density on the array with odd elements is quite different from that with even elements.

III. EXAMPLES AND DISCUSSIONS

A. Far field calculation for 1-D arrays

In this section, various results are obtained by using the formulation presented in Section Ⅱ. A 10-element period structure illuminated by a plane wave with $\theta_0 = 0$ and φ_0=90 is shown in Fig. 3. Each patch dimension is chosen to be $w \times l$ (w=55.5mm, l=60.6mm). The thickness of the substrate h=0.762mm and relative permittivity is chosen as ε_r=1.0 for simplicity. Each element is uniformly spaced from its neighbors by a distance of d=0.51 λ_0 in the y-direction. The central operating frequency is 1.42GHz.

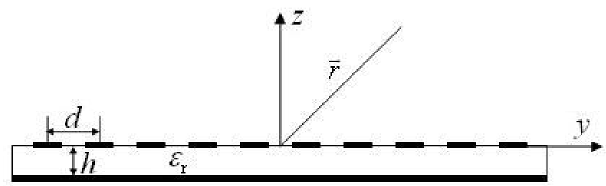

(a) Side view

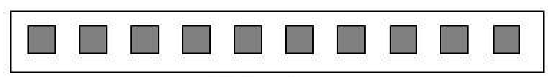

(b) Top view

Fig. 3. A 1-D 10-element array.

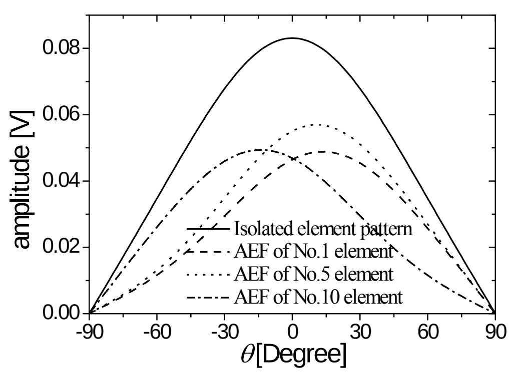

Fig. 4. Patterns calculated with isolated element and AEFs.

Figure 4 shows the isolated element pattern and varied AEFs involving all elements. It is clear that the isolated element pattern is different from the pattern of the AEFs because of the mutual-coupling effects.

The following is to determine the number of elements in a subarray involved to calculate AEFs of edge elements, adjacent edge elements and interior elements. Firstly, the far field pattern of left edge element is investigated. Figure 5 shows the far field pattern in the E-plane of left edge element in the subarray. The left edge pattern of the 4-element subarray is almost coinciding with that of the 6-element subarray. Therefore, the left edge element pattern can be determined by a 4-element subarray. Secondly, the far field pattern of the left adjacent element can be determined by a 6-element subarray from Fig. 6. Thirdly, the far field pattern of the odd interior element can be obtained by a 6-element subarray from Fig. 7. The elements on the right side can be treated in a similar way.

Therefore, only a 6-element subarray is involved to obtain all three kinds of AEF for the even-element arrays no matter how large the total element number is.

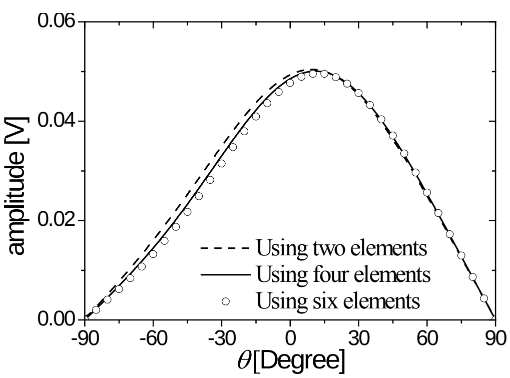

Fig. 5. AEFs of the left edge element by using different subarrays.

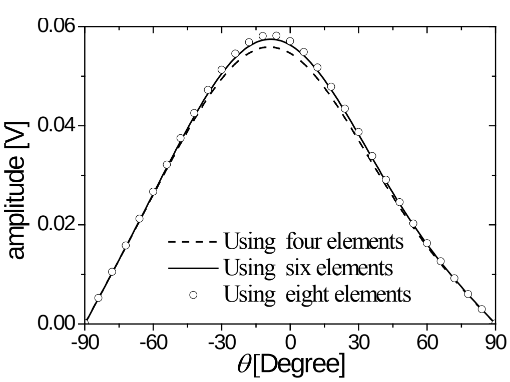

Fig. 6. AEFs of the left adjacent element by using different subarrays.

Based on the 6-element subarray, Fig. 8 plots the far field patterns of a 1-D 10-element patch array using the element-varying AEF method and the whole-array simulation with FEKO, respectively.

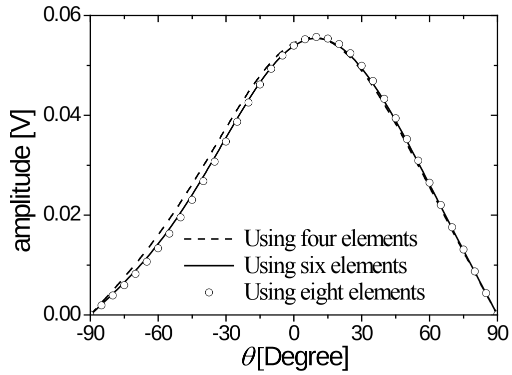

Fig. 7. AEFs of the odd interior element by using different subarrays.

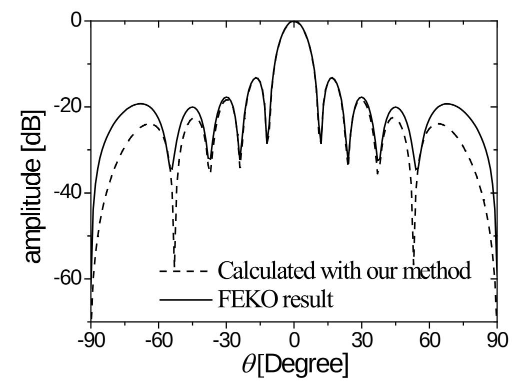

Fig. 8. Far-field pattern for the 1-D 10-element array.

The same analysis applies to an array with odd elements. Only a 5-element subarray is required to calculate the far field scattering of rather large odd-element arrays. Figure 9 plots the far field patterns of a 1-D 51-element patch array. The results show that the pattern with the element-varying AEFs method closely matches that with the whole-array simulation.

Table 1 presents the computing time comparison between the proposed method and the whole-array simulation with FEKO for the studied arrays. The proposed method shows a significant improvement in computational efficiency. All calculations are performed with an Intel Pentium Dual-Core 2.93GHz computer having 2.0GB of RAM.

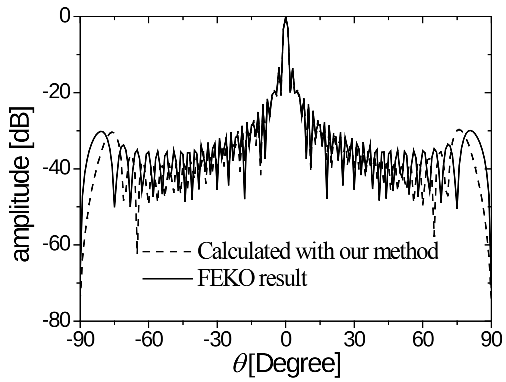

Fig. 9. Far-field pattern for the 1-D 51-element array by FEKO's simulation and the element-varying AEFs method.

Table 1: A comparison of the computing time between our method and the 1-D whole-array simulation with FEKO

10-element array	Our method	FEKO
Subarray simulation (s)	1.78	——
AEP superposition (s)	0.07×10^{-2}	——
Total time (s)	1.78	4.45
51-element array	**Our method**	**FEKO**
Subarray simulation (s)	1.22	——
AEP superposition (s)	0.01	——
Total time (s)	1.23	153.75

C. Far field calculation of 2-D finite array

The geometry of a 2-D 5×5 array illuminated by a plane wave with $\theta_0=0$ and $\varphi_0=90$ is shown in Figure 10. The materials and patch sizes are the same as the 1-D cases. Similar to a 1-D array, the array elements can be divided into corner elements, edge elements and interior elements. The analysis procedure is the same as that for a 1-D array. Thus, only a 5×5-element subarray is required to calculate a 2-D rather large odd-element array. Figure 11 illustrates the far field patterns for a 2-D 11×11-element array using the element-varying AEF method and the whole-array simulation with FEKO.

Table 2 shows that the proposed method for the 2-D 11×11-element array gets a significant improvement in computational efficiency compared to the whole-array simulation.

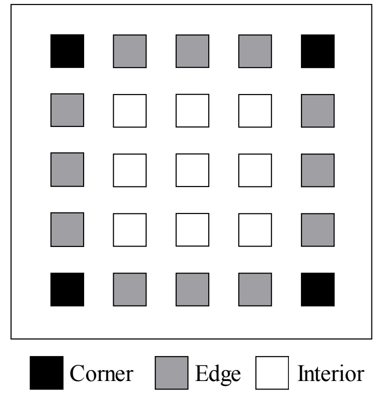

Fig. 10. Geometry of a 2-D 5×5-element array and its elements.

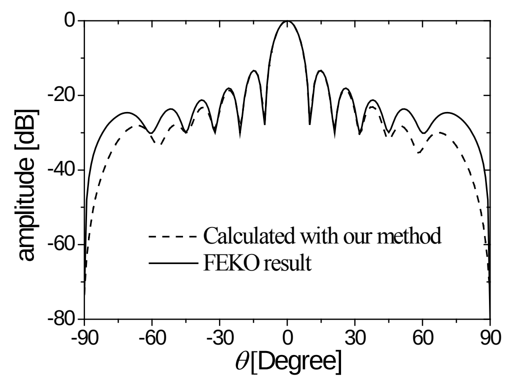

Fig. 11. Far-field pattern for an 11×11-element array.

Table 2: A comparison of the computing time between our method and the whole-array simulation with FEKO

	Our method	FEKO
Subarray simulation (s)	39.14	——
AEP superposition (s)	0.15	——
Total time (s)	39.29	10254.05

VI. CONCLUSION

In this paper, we introduce a convenient and efficient method for calculating the far field pattern of finite periodic arrays. The element-varying AEF method, considering the effects of mutual coupling and edge surroundings, involves the edge, adjacent and interior element factor patterns. Thus, it merely needs to simulate a small subarray to obtain the scattering pattern of rather large arrays. The numerical examples show that the proposed method is valid and efficient for calculating the far field scattering pattern.

ACKNOWLEDGMENT

This work is supported in part by the National Natural Science Foundation of China (60901023), the DPR Foundation (9140A03011210DZ02) and the Fundamental Research Funds for the Central Universities (ZYGX2010J043).

REFERENCES

[1] R. F. Harrington, *Field Computation by Moment Methods*, Macmillan, New York, 1968.

[2] J. M. Jin, *The Finite Element Method in Electromagnetics*, Wiley, New York, 1993.

[3] A. Taflove and S. C. Hagness, *Computational Electrodynamics: The Finite-Difference Time-Domain Method*, Artech House, 2000.

[4] H. Fangjing, N. Zaiping, and H. Jun, "An Efficient Parallel Multilevel Fast Multipole Algorithm for Large-scale Scattering Problems," *Applied Computational Electromagnetics Society* (*ACES*) *Journal*, vol. 25, no. 4, pp. 381-387, 2010.

[5] R. Maaskant, R. Mittra, and A. Tijhuis, "Fast Solution of Multi-Scale Antenna Problems for the Square Kilometre Array (SKA) Radio Telescope Using the Characteristic Basis Function Method (CBFM)," *Applied Computational Electromagnetics Society* (*ACES*) *Journal*, vol. 24, no. 2, pp. 174-188, 2009.

[6] S. Y. He, C. Li, F. Zhang, G. Q. Zhu, W. D. Hu, and W. X. Yu, "An Improved MM-PO Method with UV Technique for Scattering from an Electrically Large Ship on a Rough Sea Surface at Low Grazing Angle," *Applied Computational Electromagnetics Society* (*ACES*) *Journal*, vol. 26, no. 2, pp. 87-95, 2011.

[7] F. Xu, Y. L. Zhang, W. Hong, K. Wu, and T. j. Cui, "Finite-Difference Frequency-Domain Algorithm for Modeling Guided-wave Properties of Substrate Integrated Waveguide," *IEEE Trans. Microwave Theory Tech.*, vol. MTT-51, pp. 2221-2227, 2003.

[8] S. Singh, J. R. Zinecker, and D. R. Wilton , "Accelerating the Convergence of Series Representing the Free Space Periodic Green's Function," *IEEE Trans. Antennas and Propagat.*, vol. AP-38, pp.1958-1962, 1990.

[9] D. M. Pozar, "The Active Element Pattern," *IEEE Trans. Antennas and Propagat.*, vol. AP-42, pp. 1176-1178, 1994.

[10] D. M. Pozar, "A Relation between the Active Input Impedance and the Active Element Pattern of a Phased Array," *IEEE Trans. Antennas and Propagat.*, vol. AP-51, pp. 2486-2489, 2003.

[11] D. F. Kelley and W. L. Stutzman, "Array Antenna Pattern Modeling Methods that Include Mutual Coupling Effects," *IEEE Trans. Antennas and Propagat.*, vol. AP-41, pp. 1625-1632, 1993.

[12] F. J. Villegas, Y. Rahmat-Samii, and D. R. Jackson, "The Characteristics of Scattering from Finite Arrays of Nonuniform Cylindrical Cavities in a Ground Plane," *IEEE APS Int. Symp. Dig.*, Boston, MA, pp. 746–749, 2001.

[13] F. J. Villegas, Y. Rahmat-Samii, and D. R. Jackson, "Scattering Characteristics of Finite Arrays of Cylindrical Cavities in an Infinite Ground Plane," *IEEE Trans. Antennas and Propagat.*, vol. AP-51, pp. 2369-2379, 2003.

[14] FEKO, ver. 5.2, EM Software & System-S. A. (Pty) Ltd., Available: http://www.feko.info.

[15] D. M. Pozar, "Finite Phased Arrays of Rectangular Microstrip Patches", *IEEE Trans. Antennas and Propagat.*, vol. AP-34, pp.658-665, 1986.

[16] Q. Q. He, B. Z. Wang, and W. Shao, "Radiation Pattern Calculation for Arbitrary Conformal Arrays that Include Mutual-Coupling Effects," *IEEE Antennas and Propagat. Magazine*, vol. 52, pp. 57-63, 2010.

Qifei Li received the B.E. degree in Chengdu University of Information Technology, Chengdu, China, in 2006. From 2009 to now, she is pursuing the M.Sc. degree in the Institute of Applied Physics at the University of Electronic Science and Technology of China (UESTC), Chengdu, China. Her current research interests include the antenna radiation and array scattering.

Wei Shao received the M.Sc. and Ph.D. degrees in Radio Physics from UESTC, Chengdu, China, in 2004 and 2006, respectively.

He joined the UESTC and is now an associate professor. He has been a Visiting Scholar in the Electromagnetic Communication Laboratory, Pennsylvania State University in 2010. His research interests include the computational electromagnetics and antenna technique.

Hua Li received the Ph. D. degrees in Radio Physics from UESTC, Chengdu, China, in 2011. She joined the UESTC in 2002 and is currently a lecturer there. Her current research interests are in the areas of antenna technique and electromagnetic scattering.

Comparison of Modeling Approaches for Prediction of Cleaning Efficiency of the Electromagnetic Filtration Process

Z. Yıldız[1], M. Yuceer[2], and T. Abbasov[3]

[1] Department of Bio Engineering
Toros University, Mersin, 33140, Turkey
zehra.yildiz@toros.edu.tr

[2] Department of Chemical Engineering
Inonu University, Malatya, 44280, Turkey
mehmet.yuceer@inonu.edu.tr

[3] Department of Electrical and Electronical Engineering
Inonu University, Malatya, 44280, Turkey
teymuraz.abbasov@inonu.edu.tr

***Abstract*─** The present study aims at applying different methods for predicting the cleaning efficiency of the electromagnetic filtration process (ψ) in the mixtures of water and corrosion particles (rust) of low concentrations. In our study, artificial neural network (ANN), multivariable least square regression (MLSR), and mechanistic modelling approaches were applied and compared for prediction of the cleaning efficiency for the electromagnetic filtration process. The results clearly show that the use of ANN led to more accurate results than the mechanistic filtration and MLSR models. Therefore, it is expected that this study can be a contribution to the cleaning efficiency.

Index Terms **─** ANN, electromagnetic filtration, MLSR.

I. INTRODUCTION

Some of the known impurities in water used in the industry are mostly Feand its various compounds. In water, high concentrations of ferrous compounds cause serious problems. The ferrous compounds that accumulated in pipeline by separating on the capture surface over time to cause water pollution. Ferrous compounds result in undesirable color and turbidity.It causes to plug and the shrinkage of cross-section by accumulation inside the pipe.It is stained on the clothes and porcelain.The waters with high ferrous concentration are undesirable in various areas such as paper, leather, textile, plastic, and food industries because it leads to vary color and taste of productions.

Magnetic ferrous compounds are Fe_3O_4 andγ-Fe_2O_3. These are called also as corrosive productions. Especially, magnetite (Fe_3O_4) is a basic compound of corrosive productions. In the water and wastewaters, there are low concentrations and micron-sized dispersed particles, showing various magnetic characteristics. Various separation methods can be applied such as membrane filtration, coagulation, ion ex-changer, and precipitation. They depend on the characteristics of the solids and the ratio of the solid/liquid in the suspension. However, if the particle concentration is around 10^{-3}-10^{-5} g/kg and their sizes are lower than 1 μm, the conventional methods cannot be applied for a required separation degree. In the waters, it can be easily separated from magnetic particles using electromagnetic filters and from non-magnetic particles using other effective methods in order to use them in the plants.

Submitted On: July 19, 2011
Accepted On: Dec. 4, 2011

1054-4887 © 2011 ACES

Electromagnetic filtration is a rather simple and quite environment-friendly separation process, as it does not require any chemical or biological reagents and heavy conditions such as high temperature or pressure. Also, these filters can be simply set up and cleaned. Owing to the advantages, electromagnetic filtration is anuseful separation technique employed to separate micron and submicron magnetic particles from the carrier medium with high efficiency.For this reason, electromagnetic filters have used for the separation of heavy metal ions, phosphates, corrosion products, such as the rusts in mining, glass, ceramic, oil, power, and nuclear power generation industries [1-7].The matrix of the electromagnetic filter is composed of the magnetic packed beds, easily magnetized within an external magnetic field. The packing elements are usually balls, steel wools, metal rods, and wires. The high gradient fields are locally formed around these packing elements with an effect of the magnetic field. When liquids or gases are passing through the filter elements in the external magnetic field, the magnetic particles contained are exposed to strong sedimentation forces and most of them accumulate in the granular media of the filter elements, there it appears high gradient magnetic fields at local zones which are called capture-sections of the filter. Purification of a liquid or a gas is accomplished by passing the suspension and holding the micron sized magnetic dispersed particles in the capture-sections of the filter [1, 3, 8-13]. As magnetic filters can withstand high temperatures, corrosive and radioactive mediums, mechanical and hydro dynamical effects, these packed beds can be effectively used in the separation processes of many industrial brunches.

The electromagnetic filtration efficiency depends on several factors such as hydrodynamic, magnetic, rheological, and geometrical parameters of the system and physicochemical properties of a medium. The electromagnetic filtration efficiency is thus a multi-variable stochastic function [1-4, 14, 15]. In order to suggest a general theory for this process, effects of all these parameters must be known.

For predicting effects of the parameters such as the external magnetic field strength, diameter of the filter elements, filter length, viscosity of the suspension and the filtration velocity on the cleaning efficiency (ψ), one approach could be the identification of an input-output relationship between the involved variables based on the experimental measurements. From this perspective, artificial neural networks (ANNs) are powerful tools having the abilities to recognize underlying complex relationships from input–output data only [16].

An artificial neural network is an information processing system that imitates the behavior of a human brain by emulating the operations and connectivity of biological neurons [17]. It performs a human–like reasoning, learns the attitude, and stores the relationship of the processes based on a representative data set. In general, the neural networks do not need much of a detailed description or formulation of the underlying process, and thus, appeal to practicing engineers who tend to rely on their own data [16]. Recently, neural networks have been successfully applied to process modelingand control [18-22].

The main aim of this study is to develop a suitable ANN model by considering the feed-forward back propagation learning algorithm in the estimation of the cleaning efficiencyin the system from external magnetic field strength, filter length, diameter of the filter elements, the filtration velocity, and the viscosity of suspension parameters. Moreover, its performance comparison with the mechanistic model that was developed by Abbasov [1], and multivariate least squares regression approach are important.

II. EXPERIMENTAL METHOD

The electromagnetic filter used in the experimental studies is consisting of a non magnetic filter body and the stainless steel balls as the filter elements. As the external magnetizing medium, multipurpose electromagnetic magnetizing equipment (AC/DC, 0-220 V, and 0-10 A) has been used. The experimental studies have been carried out by placing an electromagnetic filter into this equipment, which has a 48 mm diameter. Magnetic field intensity (B) was within the range of 0-0.5 T.

The most important characteristic of the electromagnetic filters that make them more useful and popular compared to classical filters is their ability to separate micron and submicron magnetic particles from the carrier medium with high efficiency.

Experiments were carried for various conditions, such as the filtration velocity of 0.10-0.95 m/s, suspension viscosity of 0.8-10.96 cp, external magnetic field strength of175-279 kA/m, diameter of the filter elements of 4-14 mm, and filter length of 1-10 cm (Table 1).

Table 1: Parameters of the data considered for the present study

Parameters	**Min.**	**Max.**	**Average**	**Std. dev.**
$H(kA/m)$	175.070	278.521	224.500	40.618
$L(m)$	0.0100	0.1000	0.0908	0.0236
$d(m)$	0.00475	0.014	0.0077	0.0027
$V(m/s)$	0.1000	0.9500	0.1862	0.1398
$\mu(kg/m\cdot s)$	0.00008	0.01096	0.00123	0.00197
ψ	0.1800	0.8300	0.6733	0.1247

H: external magnetic field strength, *L*: filter length, *d*: diameter of the filter elements, V_f: the filtration velocity, μ: viscosity of suspension

In order to prevent the coalescence of the rust particles, a continuous mixing was applied. The filter and balls were washed and dried at the end of each experiment. After determining the total Fe amount by atomic absorption spectroscopy (AAS) analysis, the cleaning efficiency of the filtration process (ψ), was determined using the following equation:

$$\psi = \frac{C_i - C_0}{C_i}\lambda, \tag{1}$$

where, λ, the ferromagnetic fraction of the mixture, C_i and C_0 are the total Fe amount at the inlet and outlet respectively (mg/L).

The total Fe amount at the inlet is constant. A 10 g portion of particles was spread over a permanent magnet and the fraction of particles having magnetic properties was weighed. The procedure was replicated. It was determined that 85% of the corrosion products showed magnetic properties. Thus, it was determined that the magnetic fraction of the mixture (λ), was 0.85.

III. MODELLING PROCEDURE

A. Artificial neural network (ANN)model

By using the experimental observations as the input data set to identify the effects of operating parameters on the cleaning efficiency, an artificial neural network (ANN) model was created. A three-layered feed forward and a back propagation algorithm with 5 neurons in the first layer, 4 neurons in the interim layer and 1 neuron in the last layer were chosen. The network had one input layer, one hidden layer and one output layer as shown in Fig. 1. The first layer has five hyperbolic tangent sigmoid neurons, the second layer has four logarithmic sigmoid neurons, and the last layer has one linear neuron. In the course of training, which was based on the Levenberg-Marquardt method, the number of hidden layers, the number of neurons in the hidden layer, training accuracy, and the number of iterations were determined by using the trial and error method.

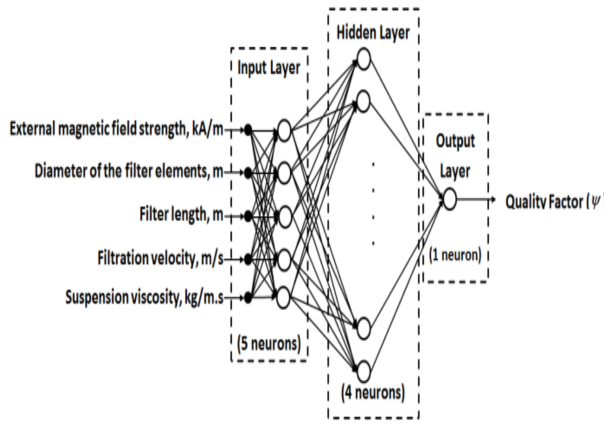

Fig.1.Schematic diagram of ANN model.

The ANN model consists of five input nodes corresponding to

(a) external magnetic field strength
(b) filter length
(c) diameter of the filter elements
(d) the filtration velocity
(e) viscosity of suspension.

The single output was the cleaning efficiency (ψ) in the system.

To develop an ANN model for estimating cleaning efficiency, the data set was partitioned into a training set and a test set. Out of 53 data sets available, 35 were used for training, and the remaining for testing. The performance function was the sum of the squares of the difference between output of ANN and observations of laboratory analysis. Training was preceded for 500 epochs. MATLAB 7.0 [23] software was used for all computations.

B. Multivariable least squares regression (MLSR)

Multivariable regression by the method of least squares is an extension of the least squares simple linear regression model. The multivariate regression methods allow the interrelationship between the response and several independent variables to be evaluated simultaneously. It also allows non-linear relationship between the response variable and the independent variables to be evaluated. The multivariable least squares regression equation is shown in equation (2).

$$y_i = \beta_0 + \beta_1 x_{i,1} + \ldots + \beta_{n-1} x_{i,n-1} + \varepsilon_i, \qquad (2)$$

where y_i is the i^{th} response. $\beta_0, \beta_1, ..., \beta_{n-1}$ are the regression parameters. $x_{i,1}, ..., x_{i,n-1}$ are the i^{th} individual's set of predictors. ε_i is the independent random error associated with the i^{th} response, typically assumed to be distributed N(0,σ). After being built on available data, the model will probably be used for predicting the values taken by the response variable for new data points $\{x\}$ that are not in the original data set (predictive modelling).

C. Model filtration theory

In general, the magnetic filtration theory can become in the basic methods of classic filtrations [24,25]. Besides other forces acting on capturing particles in the pores on magnetic filters (inertia, Archimedes density, drag etc.), the relative magnitudes of magnetic forces are the dominant mechanism in the capturing process. For this reason, the efficiency of magnetic filtration is higher than other filters [1-4]. In general, the efficiency of the magnetic filtration depends on the magnetic, rheological, geometric, and hydrodynamic parameters. On the other hand, physicochemical properties of a medium depend on these parameters determining magnetic filtration efficiency, which is a multi-variable stochastic function.

It faces toomany difficulties in the modelling and optimization of magnetic filtration performance as a variety of parameters affectsthe magnetic filtration process. But the approximation model of the filtration theory that can consider optimization of the change of magnetic filtration efficiency is in the limitation conditions. The detailed theoretical and practical investigations of the magnetic filters are reported in the literature. From the results of these studies, ψ is the cleaning efficiency as follows (equation (3)):

$$\psi = \lambda\left[1 - \exp(-\alpha L)\right]. \qquad (3)$$

where, L is the filter length, λ is the ferromagnetic fraction of the mixture, α is the fraction (coefficient) of the captured particles which depend on the magnetic, hydrodynamic, geometric, and the rheological properties of the filter. By adding the effect of diameter of the filter elements, external magnetic field strength, the filtration velocity, and the viscosity of suspension, the equation (4) can be given

$$\psi = 0.85\left(1 - exp\left\{-A\left[\frac{H^{0.75}\,L}{\mu\, d^2 V_f}\right]\right\}\right). \qquad (4)$$

where, A is rational constant, μ is the viscosity of suspension, H is magnetic field strength, d is the diameter of the filter element (stainless steel ball), V_f is the filtration velocity. It is obvious that the separation efficiency of an electromagnetic filter will depend on the operating levels of the relevant variables. In this work, we aimed at the optimization of the external magnetic field, diameter of the filter elements, filter length, and filtration velocity for the separation efficiency of the magnetic particles in the electromagnetic filters.

IV. RESULTS AND DISCUSSION

In this study, the proposed models aim to assess the effects of operating parameters on estimating the cleaning efficiency. Thus, these models were created by considering the cleaning efficiency in the mixtures of water and corrosion particles of low concentrations.

For development of the neural network model, the Neural Network Toolbox and MATLAB 7.0 were used. A MATLAB script was written, loaded the data file, trained and validated the network, and saved the model architecture.

The input data was made of the external magnetic field strength, diameter of the filter element, filter length, viscosity of the suspension, and the filtration velocity. The output data was made of the cleaning efficiency. The input data and the output data were normalized and de-normalized before and after the actual application in the network. Thus, the model was trained for input-output behavior of the system.

The neural network (NN) is exported to Simulink environment using the '*gensim*' command after the training is finished. The block diagram in Fig.2 shows the NN in Simulink [23].

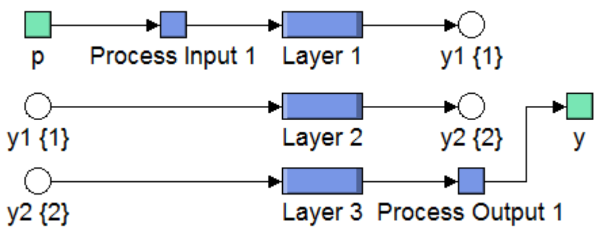

Fig. 2. Three layers of the neural network block diagram.

Figure 3 shows that the block diagram representation of the neural network model for input layer [23].Block diagrams of the neural network model for hidden layer and output layer are shown in Figs. 4 and 5, respectively [23].

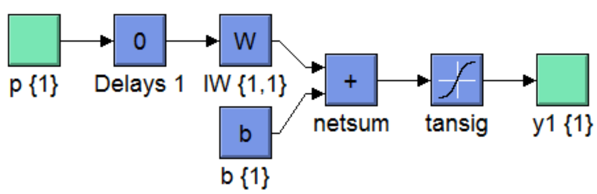

Fig. 3.Input layer simulation.

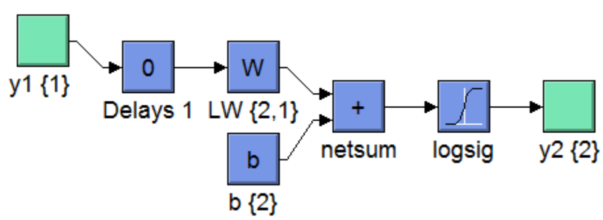

Fig. 4.Hidden layer simulation.

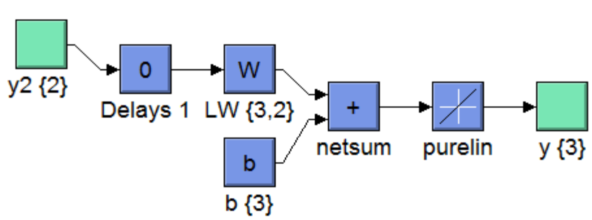

Fig. 5.Output layer simulation.

The transfer functions tansig and logsig used in this study are given in equation (5) and equation (6), respectively.

$$y_i = \frac{2}{1+e^{-2z_i}} - 1, \tag{5}$$

$$y_i = \frac{1}{1+e^{-z_i}}, \tag{6}$$

where z_i is the input of the neuron in the hidden layer and y_i is the output of neuron while calculating z_i, logsig transfer function was calculated a layer's output from its net input [23].

IW, LW, and b are defined as input weight, layer weight, and bias, respectively. In this study, values of IW, LW, and b for NN layers are given in Tables 2, 3, and 4 [23].

Table 2: Weights and bias values for input layer

IW{1,1}					b{1}
-0.0146	-0.1923	0.0820	-0.7444	-0.1297	0.0626
-0.3359	-1.6946	0.3514	-0.9232	0.9588	-1.1541
-0.0231	0.8443	-0.0010	0.2818	-0.9518	-0.1249
0.1286	0.4234	-0.2894	0.1692	-0.4117	-1.5776
0.4185	0.7018	-0.8372	0.2380	-0.4048	1.9692

Table 3: Weights and bias values for hidden layer

LW{2,1}				b{2}
0.3408	-0.4659	0.4341	0.4329	0.0911
-0.7031	1.0237	-0.9640	-0.9616	-0.2155
-0.5071	0.6775	-0.6480	-0.6468	
0.8026	-0.9064	0.8920	0.8926	0.1957
-0.9699	1.1218	-1.1010	-1.1015	0.1947

Table 4: Weights and bias values for output layer

LW{3,2}	b{3}
-1.6987	0.1829
2.2956	
-2.1251	
-2.1241	

The ANN model is summarized in the following equations (7, 8&9) [23];

$$y_1 = tansig\left[IW\{1,1\} * p + b_1\right], \tag{7}$$

$$y_2 = logsig\left[LW\{2,1\} * y_1 + b_2\right], \tag{8}$$

$$y_3 = purelin\left[LW\{3,2\} * y_2 + b_3\right], \tag{9}$$

where y_i are i^{th} output of layers. ANN model output is defined as y_3.

The preliminary results are shown in Fig. 6. The behavior of the network for the test data is shown in the following Fig. 7. As detected from Fig. 7, the network model results are compatible with the observations.

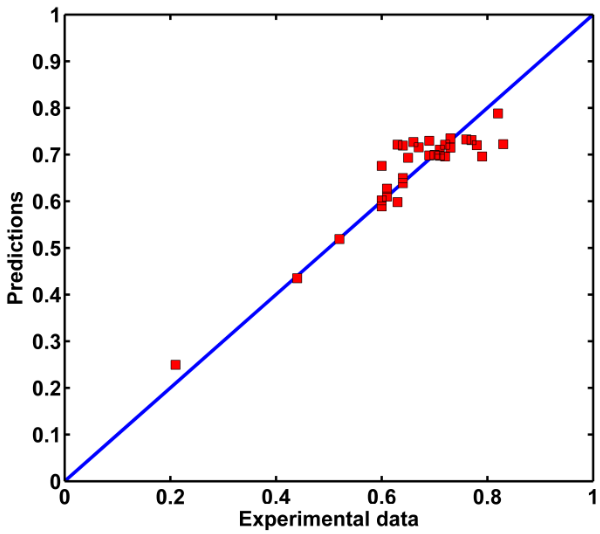

Fig. 6.ANN training results.

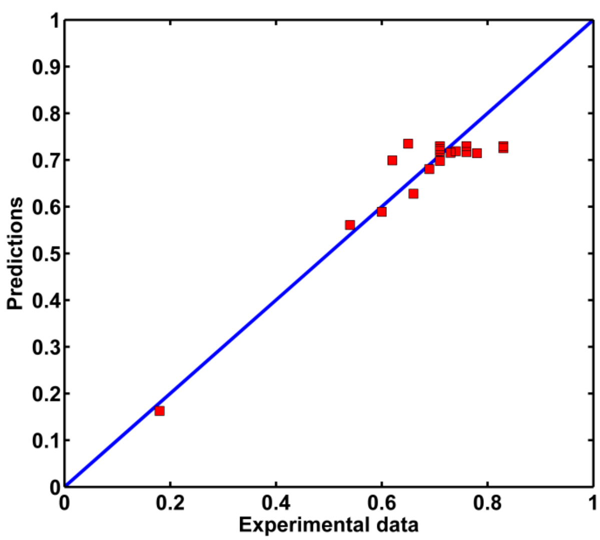

Fig.7. ANN testing results.

The MLSR analysis was performed on the training set, used to develop the neural networks. The regression parameters of the MLSR model are given in Table 5.

Prediction capability of the mechanistic model was performed on the testing data set, used to performance evaluation of the ANN and MLSR. Fig. 9 depicted the results of the mechanistic model.

Table 5: The regression parameters(in equation 2)

i	β_i
0	0.3730
1	0.3131
2	0.0318
3	-0.0022
4	-0.2443
5	-0.0096

The test data set was used to performances of the MLSR equations. The result of MLSR model is shown in Fig. 8.

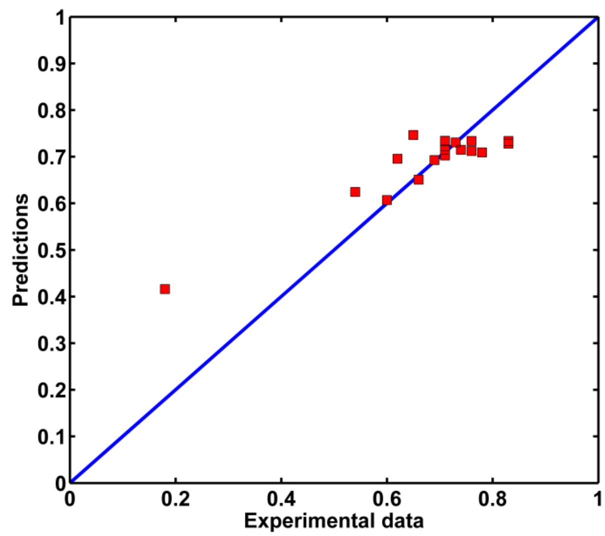

Fig.8.MLSR results for testing data.

Three parameters namely correlation coefficient (R), mean absolute percentage error (MAPE), and root mean square error (RMSE) values were used for the performance evaluation of the models.

A higher value of the correlation coefficient and the smaller values of MAPE and RMSE mean a better performance of the model. Correlation coefficients calculated for training and testing of network were 0.93 and 0.94, respectively. MAPE values were found as 4.67 % and 5.8 %.

The results suggest better performances by the artificial neural network as well as the other two approaches. Moreover, ANN is relatively more accurate than MLSR and the mechanistic model by Abbasov [1] in predicting the cleaning efficiency in the system. The results are tabulated in Table 6.

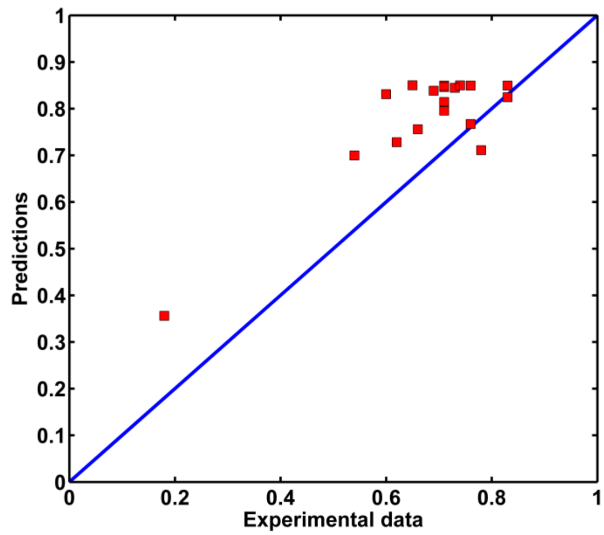

Fig.9.Mechanistic model results for testing data.

Table 6: Performance indexes achieved using ANN, MLSR and Mechanistic model during training and validation periods

	Training data			Test data		
Model	**R**	**MAPE (%)**	**RMSE**	**R**	**MAPE (%)**	**RMSE**
ANN	0.93	4.67	0.042	0.94	5.8	0.050
MLSR	0.74	9.26	0.076	0.92	12.9	0.077
Abbasov[1]	–	–	–	0.86	15.3	0.126

V. CONCLUSIONS

The proposed ANN model predicts the cleaning efficiency (ψ) in the mixtures of water and corrosion particles of low concentrations, when the external magnetic field strength, diameter of the filter elements, filter length, viscosity of the suspension, and the filtration velocity are given. The errors for MLRS (12.9 %) and the mechanistic model (15.3 %) are higher than the error obtained for ANN (5.8 %) as the capability of ANN is more than MLRS and mechanistic model in predicting the quality factor which is a complex and nonlinear process. These results showed that the ANN model is useful for the prediction of cleaning efficiency for electromagnetic filtration process. Estimation of the mechanistic model constants using a powerful optimization techniquecan give better results.

REFERENCES

[1] T. Abbasov, *Electromagnetic Filtration Processes*, 1st ed., Seçkin Publishers, Ankara, 2002.

[2] J. Svoboda, *Magnetic Techniques for the Treatment of Materials*, Kluwer Academic Publishers, USA, 2004.

[3] J. H. P. Watson, "Magnetic Filtration," *J. Appl. Phys.*, vol. 44, pp. 4209-4213, 1973.

[4] A.V. Sandulyak, *Magnetic Filtration of Liquids and Gases*, Ximiya Publishers, Moscow, 1988.

[5] M. Song, S. Kim, and K. Lee, "Development of a Magnetic Filter System using Permanent Magnets for Separating Radioactive Corrosion Products from Nuclear Power Plants," *Sep. Sci. Technol.*, vol. 39, no. 5, pp. 1037-1057, 2005.

[6] G. Gillet, F. Diot, and M. Lenoir, "Removal of Heavy Metal Ions by Superconducting Magnetic Separation,"*Sep. Sci. Technol.,* vol. 34, no. 10, pp. 2023-2037, 1999.

[7] M. Franzreb and W.H. Holl, "Phosphate Removal by High-Gradient Magnetic Separation using Permanent Magnets," *IEEE Trans. Appl. Supercond.,* vol. 10, pp. 923-926, 2000.

[8] F. J. Friedlaender and M.A. Takayasu, "Study of the Mechanism of Particle Build-Up on Single Ferromagnetic Wires and Spheres," *IEEE Trans. Magn.,* vol. 18, no. 3, pp. 817, 1982.

[9] T. Abbasov, "Theoretical Interpretation of the Filtration Process in Magnetized Packed Beds,"*Powder Technol.*,vol. 115, no. 3, pp. 215-220, 2001.

[10] T. Abbasov, "Magnetic Filtration with Magnetized Granular Beds: Basic Principles and Filter Performance,"*Chin. Particuol.,*vol. 5, no. 1-2, pp. 71-83, 2007.

[11] Z. Yıldız, T. Abbasov, and A. Sarımeşeli, "Effect of Some Process Parameters on the Separation of the Dispersed Ferrous Impurities using Cycled Electromagnetic Filter," *J. Dispersion Sci. Technol.*, vol. 31, no. 8, pp. 1072-1076, 2010.

[12] J. H. P. Watson and S.J.P. Watson, "The Ball Matrix Magnetic Separator," *IEEE Trans. Magn*., vol. 19, no. 6, pp. 2698-2704, 1983.

[13] N. A. Ebner, C.S. Gomes, G.T.J. Hobley, O.R.T. Thomas, and M. Franzreb, "Filter Capacity Predictions for the Capture of Magnetic Microparticles by High-Gradient Magnetic Separation," *IEEE Trans. Magn.,* vol. 43, no. 5, pp. 1941-1949, 2007.

[14] T. Abbasov, M. Yuceer, Z. Yildiz, and E.Sener, "Optimization of Electromagnetic Filtration Variables using a Genetic Algorithm,"*International Review of Chemical Engineering, I.RE.CH.E.*,vol. 3, no. 1, pp. 101-104, 2011.

[15] F. Mishimo, S. Takeda, M. Fukushima, and S. Nishijima, "A Superconducting Magnetic Separation System of Ferromagnetic Fine Particles from a Viscous Fluid," Physica C, vol. 463-465, pp. 1302-1305, 2007.

[16] S. Haykin, Neural Networks, *A Comprehensive Foundation*, Prentice Hall Inc., 1999.

[17] R. M. Golden, *Mathematical Methods for Neural Network Analysis and Design*, MIT Press Cambridge: MA, 1996.

[18] I. M. Mujtaba, N. Aziz, and M.A. Hussain, "Neural Network Based Modelling and Control in Batch Reactor," *Chem. Eng. Res. Des.*, vol. 84, no. 8, pp. 635-644, 2006.

[19] A.R. Khataee, G. Dehghan, M. Zarei, E. Ebadi, and M. Pourhassan, "Neural Network Modeling of Biotreatment of TriphenylmethaneDye Solution by a Green Macroalgae," *Chem. Eng. Res. Des.*, vol. 89, no. 2, pp. 172-178, 2011.

[20] I. Atasoy, M. Yuceer, E.O. Ulker, and R. Berber, "Neural Network Based Control of the Acrylonitrile Polymerization Process," *Chem. Eng. Technol.,* vol. 30, no. 11, pp. 1525-1531, 2007.

[21] M. Yuceer, "Artificial NeuralNetwork Models for HFCS Isomerization Process," *Neural Comput. Applic.,* vol. 19, no. 7, pp. 979-986, 2010.

[22] H. Kabir, Y. Cao, and Q. Zhang, "Advances of Neural Network Modeling Methods for RF/Microwave Applications," *Applied Computational Electromagnetic Society (ACES) Journal*, vol. 25, no. 5, 2010.

[23] Mathworks Inc. http://www.mathworks.com

[24] A. Adin and R. Rajagopalan, "Breakthrough Curves in Granular Media Filtration," *J. Environ. Eng.*, vol. 115, no. 4, pp. 785-789, 1989.

[25] K. J. Ives, "Deep Bed Filtration: Theory and Practice," *Filtration Separation,* vol. 17, no. 2, pp. 157-166, 1980.

Lowpass and Bandpass Filter Designs Based on DGS with Complementary Split Ring Resonators

Ghofran E. Al-Omair, Samir F. Mahmoud, and Ayman S. Al-Zayed

Electrical Engineering Department
Kuwait University, P.O. Box 5969, Al-Safat, 13060, Kuwait
alomair_g@hotmail.com, samir.hadi@ku.edu.kw, ayman.alzayed@ku.edu.kw

***Abstract*─** We present novel designs of compact lowpass filters (LPF) and bandpass filters (BPF) based on defected ground structures (DGS) using two complementary split ring resonators (CSRR) that are etched in the ground plane. The geometries of the two CSRRs, of unequal areas, are optimized for a LPF with sharp cutoff and wide stop band. For the design of the BPF, a gap capacitor is added in series with the main transmission line and the two or three etched CSRRs are designed to achieve a given bandwidth, and a wide rejection band. Simulation results on the SEMCAD-X software are compared with circuit models and measurements on fabricated lowpass and bandpass filters.

***Index Terms*─** Defected ground structures, microstrip circuit, microwave filters.

I. INTRODUCTION

Modern wireless communication systems call for compact size, low cost, and high performance components. Microwave filters are essential components in such systems and much effort has been spent recently to design compact lowpass and bandpass filters with sharp cutoff and wide stop band performance. One technique to shape filter response is to include photonic band gap (PBG) structures in filter design. This is done by etching a set of periodic defects in the ground plane of a microstrip structure. These PBG structures have the character of producing band gaps or stop bands that shape the filter response [1-3]. In addition to their stop band behavior, they have the property of slowing down the propagating electromagnetic waves, which tends to reduce the filter dimensions. However, in order to show their band gap effect, the PBG structures require the presence of many periodic cells [4, 5], which ousts the design compactness. Recently, new DGS shapes have been proposed by several authors as means of filter design by using only one or few cells. Commonly used DGS shapes include the dumbbell shape [5], the H-shape [6], the interdigital slot [7] and the split ring resonator [8-14].

A cell of such DGS disturbs the shield current in the ground plane and can increase the inductance and capacitance of the strip line. A single dumbbell defect has been modeled as a parallel L-C circuit connected in series with the line [5] and therefore acts as a one-pole lowpass filter. A similar model has been adopted for the H defect and other defects [15]. The slow wave factor caused by one or more DGS has been studied in [16].

A LPF with wide stop band has been designed on a ground plane with two dumbbell defects in [5] and with three dumbbell defects in [4]. A bandpass filter based on three sections of coupled lines on a three dumbbell defected ground has been presented in [17]. The DGSs enhance the coupling between coupled lines, which increases the filter bandwidth from 14% with no DGSs to 42%.

The use of H-shaped defect is found to result in a more compact LPF compared to one using dumbbell defects [6, 15, 18]. A crescent shape DGS structure has been utilized to design a lowpass filter [19]. A microstrip bandpass filter has been designed based on folded tri-section step impedance resonator and slotted ground defects [20].

The split ring resonator (SRR) is a building block in periodic structures behaving as metamaterial with negative permeability around its resonant frequency [11, 12]. The complimentary split ring resonator (CSRR) has been utilized as a DGS for filter design [13, 14]. The CSRR has

Submitted On: April 4, 2011
Accepted On: Oct. 28, 2011

been modeled as a parallel L-C circuit connected between the line capacitor and the ground [8, 10]. A LPF with sharp rejection has been designed based on the use of 3 CSRRs in [21]. The filter stop band has been increased by properly orienting the CSRR relative to the printed line [22]. A bandpass filter based on a pair of coupled lines and three CSRRs DGS is presented in [23]. The CSRRs tend to increase the coupling between the lines and increase the filter bandwidth. A bandwidth of 1 GHz about a center frequency of 3.5 GHz has been reported [23].

In this paper, we present a simple design of compact LPF using two or three CSRR DGS. The microstrip transmission line joining the input to the output is a uniform 50Ω line with no discontinuities or connected stubs. The distances between the defects and their areas are optimized to obtain a filter with sharp cutoff and wide stop band. In addition, a bandpass filter is designed by using two or three CSRRs and a gap capacitor connected in series with the main printed line.

The proposed LPF is introduced in the next section along with an equivalent circuit model. The latter is compared with simulation results taken on SEMCAD-X software. Similarly, the proposed BPF is presented in Section III along with its circuit model and simulation results. The capability of enhancing the rejection band is illustrated in this section by adding a third CSRR defect. Several versions of the LPF and BPF are built and tested. Measurements on both filters are compared with simulations in Section IV. The conclusions are drawn in Section V.

II. DESIGN AND GEOMETRY OF THE LOWPASS FILTER

The geometry of the proposed LPF is shown in Fig. 1a, where a 50 Ω strip line is printed on the dielectric layer surface and two CSRRs are etched in the ground plane. The two complementary SRRs are similar to one another except that the smaller ring (A2) is rotated by 90° relative to the larger ring (A1). The area of both rings and the spacing between them are design parameters that must be properly chosen in order to obtain a favorable filter response. The CSRR main parameters are shown in the inset of Fig. 1a. These are the slot width (t), the slot gap (g), the spacing (c) between inner and outer rings, and the side length (a). The role of these parameters in shaping the LPF response has been studied in [8, 16]. The circuit model of the LPF is shown in Fig. 1b, where each ring is modeled by a parallel L-C circuit (L3, C3 and L4, C4) connected in series with the line capacitance [8]. The distance between the centers of the CSRRs is modeled by a transmission line (TL) of a given electrical length (θ) at the cutoff frequency.

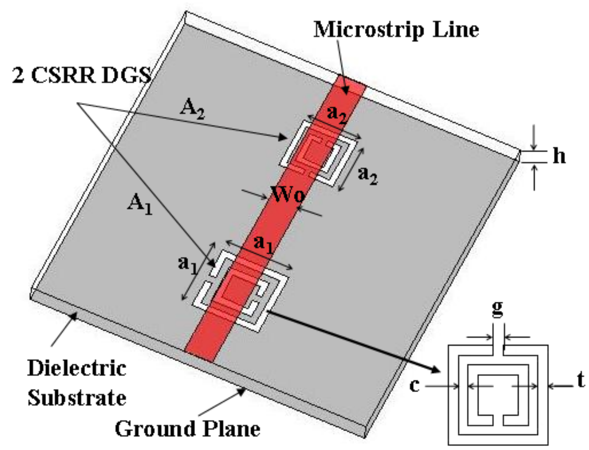

(a)

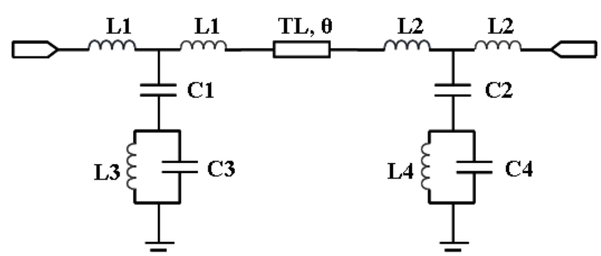

(b)

Fig. 1. (a) Geometry of the proposed lowpass filter. (b) Equivalent circuit model.

Using the simulation tool SEMCAD X, we have designed a LPF with the response shown in Fig. 2. The notch frequency of S_{21} at f =2.7 GHz is mainly determined by the dimensions of ring (A1), which is the first (larger) CSRR. The second notch frequency at 3.45 GHz is mainly determined by ring (A2) whose linear dimensions are 85% of ring (A1). The dimensions of ring (A2) influence the stop band, which extends up to 4.75 GHz. The flatness of the pass band response is affected by the dimensions (t), (g), and (c) of the two CSRRs. The simulated S_{11} response lies below -10 dB in the passband. The dimensions of the two CSRRs used in the LPF of Fig. 2 are tabulated in Table 1 along with the spacing (D) between the centers of the two rings. It is important to note that the rotation of the smaller CSRR by 90° relative to the first one has a major role in achieving the low response level over the wide stop band of the filter. The total length of the filter is about 40 mm. This amounts to one third of the free space wavelength at the 3-dB cutoff frequency (2.5 GHz).

To obtain the equivalent circuit model of the presented LPF, we optimize the circuit elements of Fig. 1b on the Agilent's advanced design system (ADS) software so as to match the simulated S_{21} response. The inferred circuit model S_{21} response is compared with the simulated one in Fig. 2. A good match is observed, particularly in the pass band region. The corresponding values of the circuit elements are tabulated in Table 2. In particular, we note that the electrical length between the centers of the two CSRRs is 140 degrees at 2 GHz. This is certainly influenced by the slow wave effect caused by the CSRR defects [10]. Namely, the effective relative permittivity is about 4.66 in the presence of the defects. Finally, we note that as (A2) is reduced in area while (A1) is kept fixed, the stop band extends to higher frequencies, but the response can exceed the -10 dB limit. A good design ratio of a2/a1 is found to lie between 0.75 and 0.85.

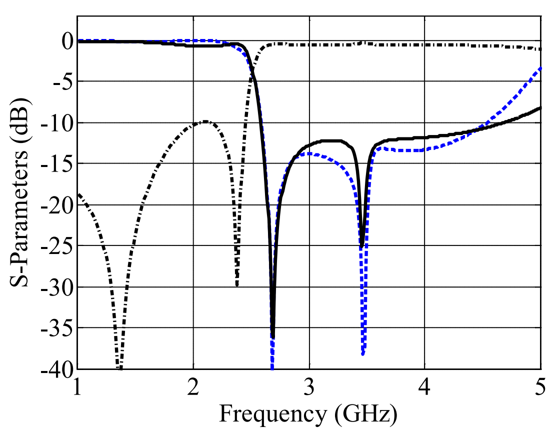

Fig. 2. Comparison between simulated S_{21} (solid line) and circuit model (dashed line) results of the proposed lowpass filter. The simulated S_{11} is shown as dash-dot line. The substrate used has thickness h=1.5 mm and dielectric constant of 2.55.

Table 1: Geometric design parameter details of the proposed lowpass filter in millimeter

a1	t1	s1	c1		
10	1	1	1		
a2	t2	s2	c2	W_o	D
8.5	0.85	0.85	0.85	4.19	27

Table 2: Extracted equivalent circuit parameters of the proposed lowpass filter (Capacitors in (pF), Inductors in (nH))

C1	L1	C2	L2	
0.912	2.5	1.02	2.16	
C3	L3	C4	L4	θ
1.26	1.62	1.136	0.973	140°

It is worth comparing our lowpass filter response with that introduced in [8]. While the two filter responses are comparable to each other our proposed filter does not require any open stubs loading the conductor line.

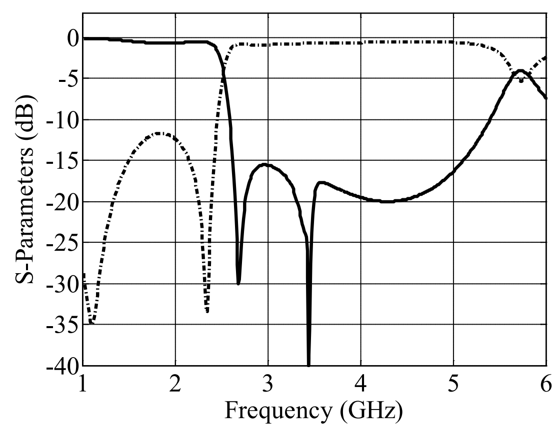

Fig. 3. Simulation results of S_{21} and S_{11} of the three CSRRs LPF. The third ring is 97% of the second ring and is spaced by 20 mm from the second ring.

In order to extend the stop band to higher frequencies, a third CSRR is etched down the line. The added ring size and distance from the second ring are optimized for extended stop band. The simulated result for S_{21} and S_{11} is shown in Fig. 3. The S_{21} is maintained below -15.5 dB in the stop band that extends to 5.1 GHz. This is a definite improvement to the two-CSRR design. The total length of the filter has been increased by 55% compared with the filter using two CSRR defects. It is instructive to compare our three-CSRR with that given in [21] in which the same number of

CSRR's is used. The frequency responses are comparable except that the transition to the stop band is sharper in our design In addition; the strip line in our design is uniform in contrast with the non-uniform line in [21].

III. DESIGN AND GEOMETRY OF THE BANDPASS FILTER

The geometry of the proposed bandpass filter (BPF) is shown in Fig. 4a, where a 50 Ohm line is printed on the dielectric layer and two CSRRs are etched in the metallic ground plane. The line has a series capacitance in the form of an L-shaped gap as shown in the inset of the figure. The two CSRRs are similar in shape and orientation, but have different areas; the second one down the line being the smaller ring ($b_2/b_1<1$). The design parameters shown in Fig. 4a can be carefully adjusted to obtain the desired bandpass filter response.

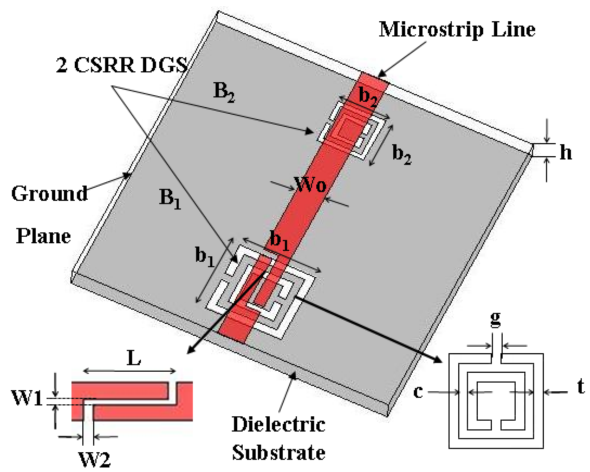

(a)

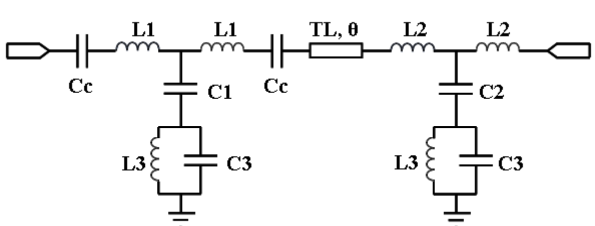

(b)

Fig. 4. (a) Geometry of the proposed bandpass filter. (b) Equivalent circuit model.

The design parameters given in Table 3 are the result of a series of simulations using SEMCAD-X software to reach the bandpass response shown in Fig. 5. The L like gap and the large CSRR (B1) influence the low frequency notch at 1.8 GHz, and the attenuation level of the lower band. The smaller CSRR (B2) determines the second notch at 3.7 GHz. It should be pointed out that the two CSRRs must have the same orientation in order to obtain a flat bandpass response. The EM simulated S_{11} is well below -10 dB in the passband. The total filter length is about 45 mm, which amounts to 0.41 of the free wavelength at the midband frequency (2.75 GHz).

An equivalent circuit model of the proposed bandpass filter is shown in Fig. 4b. It clearly resembles that of the LPF (in Fig.1b) except for the added series capacitor (Cc) that represents the L cut. The values of the equivalent inductors, capacitors, as well as the transmission line length between the centers of the two rings were optimized so as to match the simulated S_{21} filter response by using the ADS software. The optimized circuit parameters are summarized in Table 4. The response of the simulated and modeled bandpass filter show good agreement of S_{21} as observed in Fig. 5.

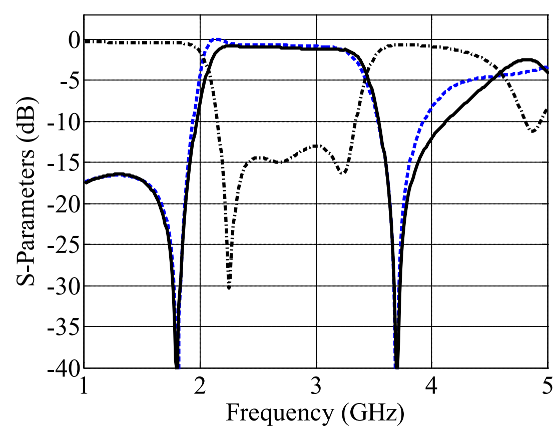

Fig. 5. Comparison between simulation (solid line) and circuit model (dashed line) results for S_{21} of the proposed bandpass filter. The simulated S_{11} is shown by the dash-dotted line. The substrate used has thickness h=1.5 mm and dielectric constant of 2.55.

In an attempt to extend the stop band to higher frequencies, we have added a third CSRR defect down the line. The added CSRR has smaller dimensions and is rotated by 90° relative to the other two rings. This result is an extension of the stop band up to 5.52 GHz compared to 4.5 GHz for the case of two rings; the attenuation level was also improved as shown in Fig. 6.

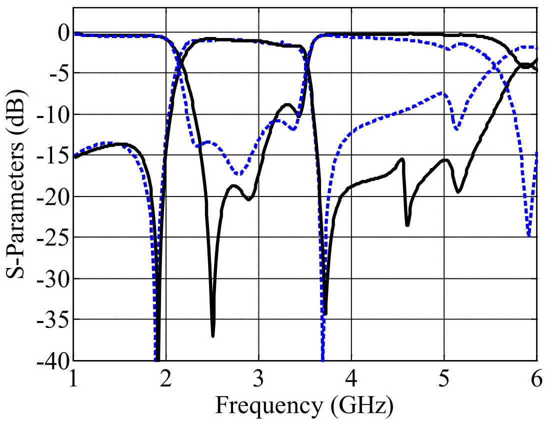

Fig. 6. Simulation results of S_{21} and S_{11} of the three CSRRs BPF with wide stop band (solid lines) compared to the two CSRRs BPF (dotted lines). The third ring is 86.67% of the second ring and is spaced by 21 mm from the second ring.

Table 3: Geometric design parameter details of the proposed bandpass filter in millimeter

b1	t1	s1	c1	b2	t2	s2
12	1.2	1.2	1.2	7.5	0.75	0.75

c2	W_o	D	L	W1	W2
0.75	4.19	31	10	0.6	1

Table 4: Extracted equivalent circuit parameters of the proposed bandpass filter (Capacitors in (pF), Inductors in (nH))

C1	L1	C2	L2	C3
1.77	2.86	0.73	1.82	1.44

L3	C4	L4	Cc	θ
2.43	0.91	1.13	0.86	111.6°

IV. FABRICATIONS AND MEASUREMENTS

In order to verify the design method of the proposed filters, several lowpass and bandpass filters were fabricated and tested using a network analyzer. All of the lowpass and bandpass filter designs were implemented on Taconix/TLX-8 substrate with dielectric constant εr =2.55, height h=1.5 mm, and loss tangent = 0.002. These values are the same as those used for all of the simulations.

Figure 7 shows photographs of the top side (a) and bottom side (b) of the manufactured lowpass. The 90 degree rotation of the smaller CSRR can be seen. Two lowpass filters were fabricated and measured. The first one is the implementation of the one given in Fig. 2. The second fabricated lowpass filter has a larger ring (A1) which was scaled up by about 15% (so that a_2 was increased from 10 to 11.5 mm). The electromagnetic simulation and the measured results of these two filters are shown in Fig. 8a and 8b, respectively. A good agreement is observed between the measurements and simulations. We note that the cutoff frequency of the second LPF (Fig. 8b) is lower than that for the one in Fig. 8a. This is a result of the larger dimensions of the (A1) ring.

Figure 9 shows photographs of the top side (a) and bottom side (b) of the fabricated bandpass filter of Fig. 5 with the parameters listed in Table 3. The simulated and measured results for this bandpass filter are presented in Fig. 10a and good agreement is observed. The measured 3dB bandwidth of the first filter is 1.38 GHz, while the best insertion loss is 0.86 dB measured at 2.06 GHz.

Another BPF with scaled down second ring (B2) by 6.7% (b_2 is reduced 7 mm) is built and measured. The simulation and measurement results of this filter are shown in Fig. 10b. Notice that the second notch frequency is shifted to a higher frequency relative to that in Fig. 10a as one would expect. The measured 3dB bandwidth of this filter is 1.6 GHz, while the best insertion loss is 0.82 dB measured at 2.25 GHz.

V. CONCLUSION

We have presented novel and simple designs of compact LPF and BPF based on DGS using two or three CSRRs of different areas. The desired filter responses are achieved by using a simple 50 ohms transmission line, without the need for step impedances or any junction discontinuity which yield design simplicity. The performance of these filters has been verified by simulations, circuit models, and measurements on fabricated prototypes. The smaller CSRR in the proposed LPF is rotated by 90° relative to the larger one. This is necessary to obtain an acceptable stop band response. It is demonstrated that the cutoff frequency of the LPF is mainly controlled by the geometry and the area of the larger CSRR, while the second CSRR determines the extent of the stop band. Adding a third ring will extend the stop band as well as improve the attenuation level in the rejection band.

The proposed BPF contains two CSRR ground defects of different areas but having the same orientation. In addition, a gap capacitor is connected in a series with the main printed line. It is demonstrated that the gap capacitor and the first CSRR defect (B1) control the low frequency response and the first cutoff frequency (fc1) while the second CSRR defect (B2) controls the higher cutoff frequency (fc2), hence the filter bandwidth. It has been demonstrated that a third smaller CSRR defect, added down the line, can significantly improve the upper stop band and extends it to higher frequencies (Fig. 6). The measured filter responses on manufactured LPFs and BPFs have shown excellent agreement with simulated results.

ACKNOWLEDGEMENT

Dr. Ayman Al-Zayed would like to acknowledge Kuwait University for their support and making his sabbatical leave during the academic year 2010-2011 successful.

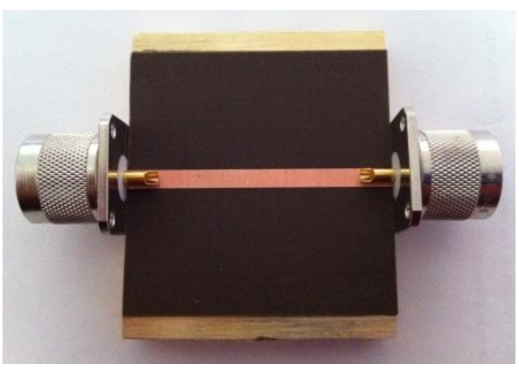

(a)

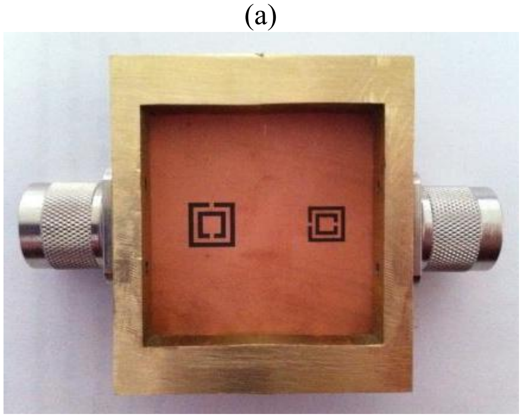

(b)

Fig. 7. Photographs of the fabricated lowpass filter (a) Top side. (b) Bottom side.

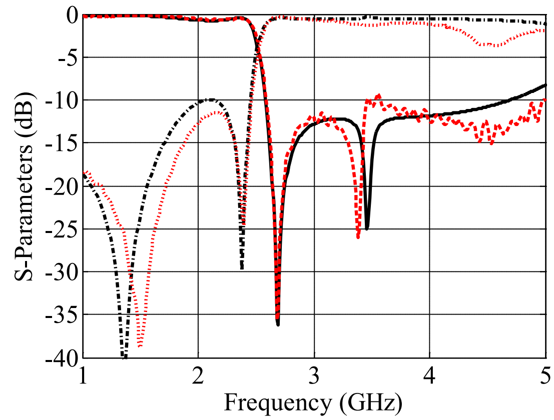

Fig. 8a. Simulation results compared to measured results of the proposed lowpass filter of Fig. 2. Simulated S_{21} and S_{11} are shown as (solid), (dash-dot) lines, respectively. Measured S_{21} and S_{11} are shown as (dashed) and (dotted) lines, respectively.

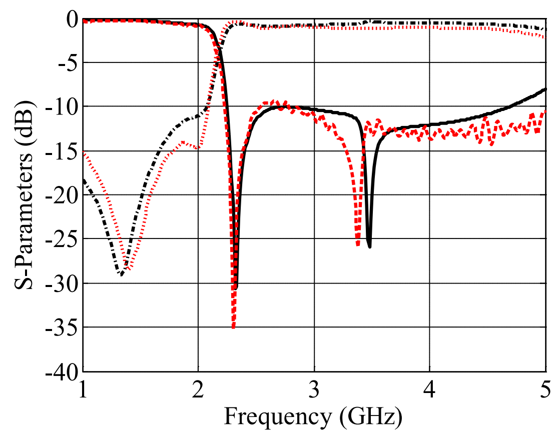

Fig. 8b. Same as Fig. 8a except for a larger A_1 ring (a_1 is increased from 10 to 11.5 mm)

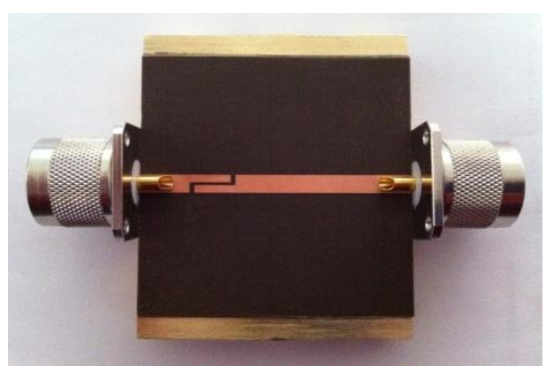

Fig. 9a. Photographs of the top side of fabricated bandpass filter.

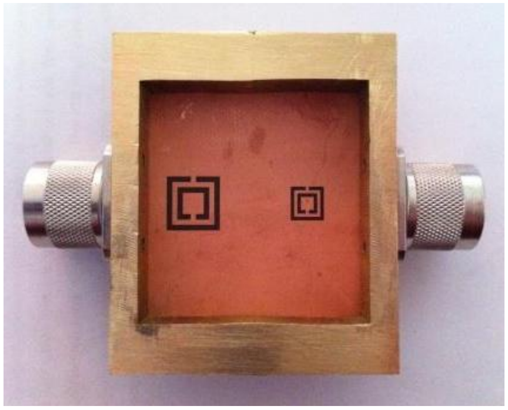

Fig. 9b. Photographs of the bottom side of fabricated bandpass filter.

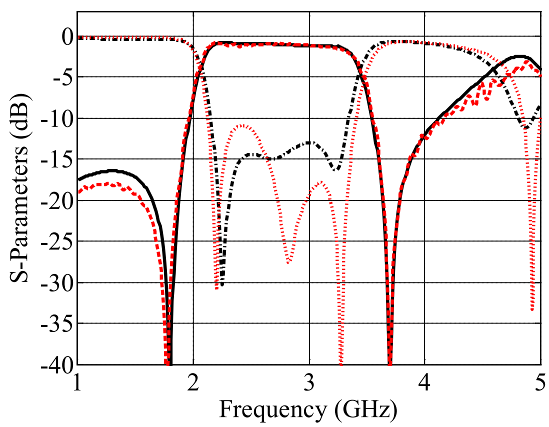

Fig. 10a. Simulation results compared to measured results of the proposed bandpass filters of Fig. 5. Simulated S_{21} and S_{11} are shown as (solid), (dash-dot) lines, respectively. Measured S_{21} and S_{11} are shown as (dashed) and (dotted) lines, respectively.

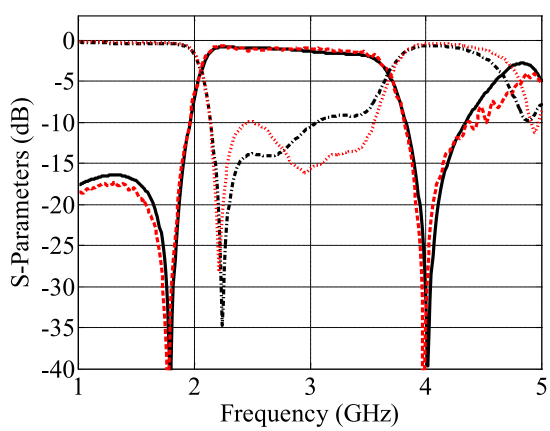

Fig. 10b. Same as Fig. 10a except for a larger (B2) ring.

REFERENCES

[1] V. Radisic, Y. Qian, R. Coccioli, and T. Itoh, "Novel 2-D Photonic Bandgap Structure for Microstrip Lines," *IEEE Microwave Guide Wave Lett.*, vol. 8, pp. 69 – 71, 1998.

[2] F. R. Yang, K. P. Ma, Y. Qian, and T. Itoh, "A Uniplanar Compact Photonic-Bandgap (UC-PBG) Structure and Its Applications for Microwave Circuits," *IEEE Trans. Microw. Theory Tech.*, vol. 47, no. 8, pp. 1509 – 1514, 1999.

[3] Y. Yang, Qian, R. Coccioli, and T. Itoh, "A Novel Low Loss Slow-Wave Microstrip Structure," *IEEE IEEE Microwave Guide Wave Lett.*, vol. 47, no. 8, pp. 372 – 374, 1998.

[4] J. S. Lim, C.-S. Kim, D. Ahn, Y.-C. Jeong, and S. Nam, "Design of Low-Pass Filters using Defected Ground Structure," *IEEE Transactions On Microwave Theory And Tech.*, vol. 53, no. 8, pp. 2539 – 2545, 2005.

[5] D. Ahn, J.-S. Park, C.-S. Kim, J. Kim, Y. Qian, and T. Itoh, "A Design of the Low-Pass Filter using the Novel Microstrip Defected Ground Structure," *IEEE Transactions On Microwave Theory And Tech.*, vol. 49, no. 1, pp. 86 – 93, 2001.

[6] M. K. Mandal and S. Sanyal, "A Novel Defected Ground Structure for Planar Circuits," *IEEE Microwave Compon. Lett.*, vol. 16, no. 1, pp. 93 – 95, 2006.

[7] H. Liu, Z. Li, and X. Sun, "Compact Defected Ground Structure in Microstrip Technology," *Electron. Lett.*, vol. 41, no. 3, pp. 132 – 134, 2005.

[8] B. Wu, B. Li, T. Su, and C.-H. Liang, "Study on Transmission Characteristic of Split-Ring Resonator Defected Ground Structure," *Progress In Electromagnetics Research*, vol. 2, no. 6, pp. 710 – 714, 2006.

[9] Z. –Z. Hou, X. –X. Li, and C. –K. Hao, "Design of Wideband Filter Using Split-ring Resonator DGS," *Progress In Electromagnetics Research Symposium, Hangzhou, China*, pp. 33-36, 2008.

[10] C Li and F. Li, "Characterization and Modelling of a Microstrip Line Loaded with Complementary Split-Ring Resonators (CSRRs) and its Application to Highpass Filters," *Journal of Physics D: Applied Physics*, vol. 40, pp. 3780 – 3787, 2007.

[11] J. B. Pendry, A. J. Holden, D. J. Robbins, and W. J. Stewart, "Magnetism from Conductors and Enhanced Nonlinear Phenomena," *IEEE Transactions on Microwave Theory and Tech.*, vol. 47, no. 11, pp. 2075 – 2084, 1999.

[12] F. Falcone, T. Lopetegi, M. A. G. Laso, J. D. Baena, J. Bonache, M. Beruete, R. Marque´s, F. Martı´n, and M. Sorolla, "Babinet Principle Applied to the Design of Metasurfaces and Metamaterials," *Physical Review Letters,* vol. 93, no. 19, pp. 197401-1 – 197401-4, 2004.

[13] M. Beruete, M. Sorolla, R. Marques, J. D. Baena, and M. Freire, "Resonance and Cross-Polarization Effects in Conventional and Complementary Split Ring Resonator Periodic Screens," *Electromagnetics*, vol. 26, Iss. 3 and 4, pp. 247-260, 2006.

[14] N. Ortiz, J. D. Baena, M. Beruete, F. Falcone, M. A. G. Laso, T. Lopetegi, R. Marque´s, F. Martin, J. Garcia-Garcia, and M. Sorolla, "Complementary Split-Ring Resonator for Compact Waveguide Filter Desing," *Journal of Microwaves, Optoelectronics and Electromagnetic Applications*, vol. 46, no. 1, pp. 88 – 92, 2005.

[15] L. H. Weng, Y. C. Guo, X. W. Shi, and X. Q. Chen, "An Overview on Defected Ground Structure," *IEEE Progress In Electromagnetics Research B*, vol. 7, pp.173 – 189, 2008.

[16] H.-W. Liu, Z.-F. Li, X.-W. Sun, S. Kurachi, J. Chen, and T. Yoshimasu, "Theoretical Analysis of Dispersion Characteristics of Microstrip Lines with Defected Ground Structure," *J. of Active and Passive Electronic Devices*, vol. 2, pp. 315 – 322, 2007.

[17] S. K. Parui and S. Das, "Improvement of Passband Characteristics of Microstrip Band Pass Filter by Defected Ground Structures," *The National Conference on Communications*, pp. 341 – 344, 2007.

[18] A. Boutejdar, A. Elsherbini, and A. Omar, "Design of a Novel Ultra-Wide Stopband Lowpass Filter using H-Defected Ground Structure," *Journal of Microwaves, Optoelectronics and Electromagnetic Applications*, vol. 50, no. 3, pp. 771 – 775, 2008.

[19] M. Al Sharkawy, A. Boutejdar, F. Alhefnawi, and O. Luxor, "Improvement of Compactness of Lowpass/Bandpass Filter Using a New Electromagnetic Coupled Crescent Defected Ground Structure Resonators," *Applied Computational Electromagnetic Society (ACES) Journal*, vol. 25, no. 7, pp. 570–577, July 2010.

[20] N. M. Garmjani and N. Komjani, "Improved Microstrip Folded Tri-Section Stepped Impedance Resonator Bandpass Filter using Defected Ground Structure," *Applied Computational Electromagnetic Society (ACES) Journal*, vol. 25, no. 11, pp. 975–983, November 2010.

[21] J. Zhang, B. Cui, S. Lin, and X.-W. Sun, "Sharp-Rejection Low-Pass Filter with Controllable Transmission Zero using Complementary Split Ring Resonators (CSRRs)," *Progress In Electromagnetics Research*, PIER 69, pp. 219 – 226, 2007.

[22] S. N. Khan, X. G. Liu, L. X. Shao, and Y. Wang, "Complementary Split Ring Resonators of Large Stop Bandwidth," *Progress In Electromagnetics Research Letters*, vol. 14, pp. 127 – 132, 2010.

[23] X. Lai, Q. Li, P. Y. Qin, B. Wu, and C.-H. Liang, "A Novel Wideband Bandpass Filter Based on Complementary Split-Ring Resonator," *Progress In Electromagnetics Research C*, vol. 1, pp. 177 – 184, 2008.

[24] S. K. Parui and S. Das, "Modeling of Split-Ring Type Defected Ground Structure and its Filtering Applications," *Journal of Microwaves, Optoelectronics and Electromagnetic Applications*, vol. 8, no. 1, pp. 6 – 12, 2009.

Full-Wave Analysis of Loaded Dipole Antennas using Mode-Matching Theory

Amir Jafargholi and Manouchehr Kamyab

Department of Electrical Engineering
K. N. Toosi University of Technology, P.O.Box 16315-1355. Tehran, Iran
Jafargholi@ee.kntu.ac.ir, Kamyab@kntu.ac.ir

Abstract **─** The influence of the material inclusions on the input impedance of the loaded dipoles excited by a delta function is analytically investigated. Novel and accurate analytical expressions for the input impedance of the loaded dipoles are proposed based on the mode matching technique. The boundary conditions are also enforced to obtain several simultaneous equations for the discrete modal coefficients inside the radiating region. Study of the input impedance of the whole multilayered structure is accomplished by the cascade connection of mediums as characterized by their constitutive parameters. The derived formulas are successfully validated through a proper comparison with the results obtained with the commercial software CST Microwave Studio.

Index Terms **─** Loaded dipole, mode-matching.

I. INTRODUCTION

In recent years, the introduction of metamaterials (MTMs) opened the way for many research groups to enhance antenna performances. Due to unique electromagnetic properties, MTMs have been widely considered in monopole and dipole antennas to improve their performance [1-5]. The problem of dielectric loaded wire antenna is heretofore analyzed using numerical methods, e.g., method of moment (MoM) [6], finite difference time domain (FDTD) [7], and simulations based on commercial software [8]. However, the analytical analysis of the dielectric loaded dipole antennas has not been reported in the literature.

The novelty of this paper is to introduce a mode-matching analysis of a dipole antenna loaded with material inclusions. The concept of the MTM loaded dipole is very important and, as to the authors' best knowledge, there are no papers reporting analytical expressions and full-wave analysis of this class of loaded antennas. In this paper, a theoretical formulation for a multiply dielectric loaded slotted spherical antenna is proposed based on the mode-matching method, to predict the behavior of the loaded dipole. It is worth noting that the radiation pattern of a finite length small angle biconical antenna differs only slightly from the pattern of a dipole [9]. Here, since the biconical antenna can be exactly analyzed and it also reduces, in the limiting case, to a cylindrical dipole antenna [10], this structure is considered for the analytical investigations. The obtained analytical formulas confirm the general conclusions recently presented in [7, 8], regarding the effect of material inclusions on the dipole antenna performance. It is demonstrated that the inclusion influence on the input impedance of a dipole is significant only for double-negative (DNG) MTM inclusions. The analytical results have been successfully validated through a comparison with the numerical results. The CST MICROWAVE is adopted for the simulations.

II. FIELD ANALYSIS

Figure 1a, illustrates a slotted dielectric loaded hollow conducting sphere of radius a, containing a Hertzian dipole $\bar{J} = \hat{z}J\delta(\bar{r} - \bar{r}')$, placed at the center ($r = r', \theta = 0, \varphi$), here (r, θ, φ) are the spherical coordinates and δ is a delta function. The time convention is $e^{-j\omega t}$ suppressed throughout. Due to

Submitted On: Aug. 15, 2011
Accepted On: Dec. 18, 2011

azimuthally symmetry, the fields depend on (r,θ) and the fields are then TM waves, which can be expressed in terms of magnetic vector potentials. The total magnetic vector potential for the un-slotted sphere (First region, I) is a sum of the primary and secondary magnetic vector potentials, [11].

$$A^i(r,\theta)=\hat{z}A_z^p(r,\theta)+\hat{r}A_r^s(r,\theta), \tag{1}$$

while, the primary magnetic vector potential is a free-space Green's function as

$$A_z^p(r,\theta)=\frac{\mu_1 J}{4\pi}\frac{e^{ik_1R}}{R}, \tag{2}$$

$\hat{z}$ and $\hat{r}$ are the unit vectors and $R=\sqrt{r^2+r'^2-2rr'\cos\theta}$. And the secondary magnetic vector potential is

$$A_r^s(r,\theta)=\sum_{n=0}^{\infty}a_n\hat{J}_n(k_1r)P_n(\cos\theta), \tag{3}$$

where $\hat{J}_n(.)$ and $P_n(.)$ are the spherical Bessel and Legendre functions, respectively, and [11]

$$a_n=\frac{\mu_1 aJ}{8\pi k_1\hat{J}'_n(k_1a)}\frac{2n+1}{n(n+1)}\int_0^{\pi}\Omega\frac{\partial P_n(\cos\theta)}{\partial\theta}\sin^2\theta d\theta$$
$$\Omega=\begin{Bmatrix}\left(a^2-2r'^2+ar'\cos\theta\right)\left(ik_1\tilde{R}-1\right)\\+k_1^2\tilde{R}^2\left(a^2-ar'\cos\theta\right)\end{Bmatrix}\frac{e^{ik_1\tilde{R}}}{\tilde{R}^5}. \tag{4}$$

Now consider a slotted conducting sphere, as shown in Fig. 1a. The total magnetic vector potential in region (I) consists of the incident A^i and scattered A_r^I potentials as

$$A_r^I(r,\theta)=\sum_{n=0}^{\infty}C_n\hat{J}_n(k_Ir)P_n(\cos\theta). \tag{5}$$

Here, C_n is an unknown modal coefficient. The *r*-component of the magnetic vector potential in region (II, III, IV, and V) of the *l*-th slot is

$$A_r^{\gamma}(r,\theta)=\sum_{v=0}^{\infty}R_v^{l,\gamma}(\cos\theta)\left[D_v^{l,\gamma}\hat{J}_{\xi_v^l}(k_\gamma r)+E_v^{l,\gamma}\hat{N}_{\xi_v^l}(k_\gamma r)\right], \tag{6}$$

where $\gamma=II,III,IV,V$ and

$$R_v^{l,\gamma}(\cos\theta)=\begin{cases}Q_{\xi_v^l}(\cos\theta) & v=0\\ Q_{\xi_v^l}(\cos\alpha_2^l)P_{\xi_v^l}(\cos\theta)- & \\ P_{\xi_v^l}(\cos\alpha_2^l)Q_{\xi_v^l}(\cos\theta) & v\geq 1\\ P_{\xi_v^l}(\cos\theta)+G_{\xi_v^l}^{\gamma}Q_{\xi_v^l}(\cos\theta) & III,IV\end{cases} \tag{7}$$

The *r*-component of the magnetic vector potential in region (VI) is

$$A_r^{VI}(r,\theta)=\sum_{v=0}^{\infty}F_n\hat{H}_n^{(2)}(k_{VI}r)P_n(\cos\theta), \tag{8}$$

where F_n is an unknown modal coefficient and $\hat{H}_n^{(2)}(.)$ is the spherical Hankel function of the second kind.

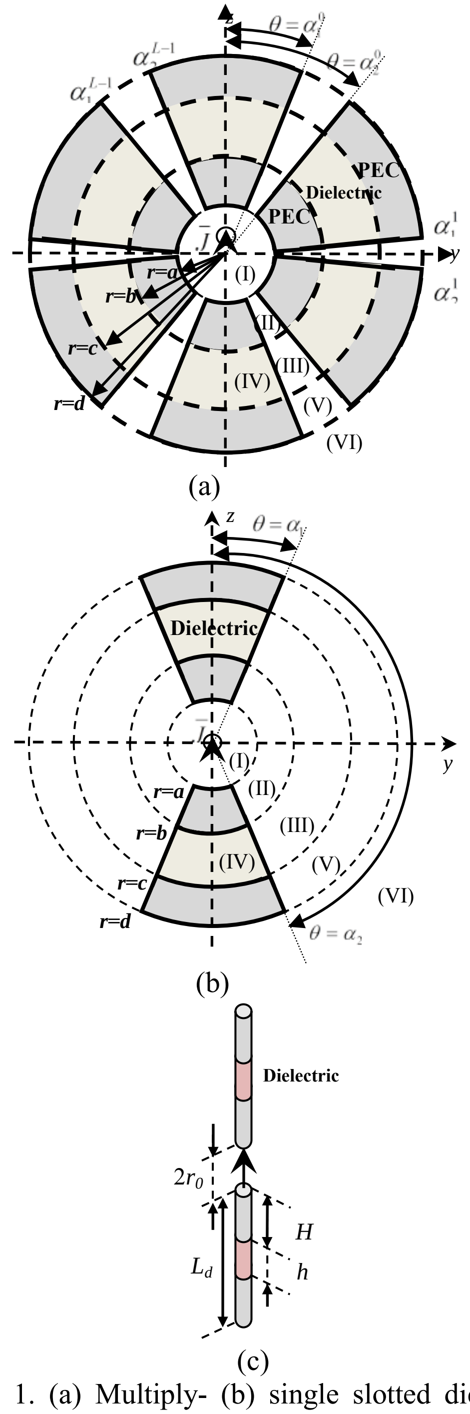

Fig. 1. (a) Multiply- (b) single slotted dielectric loaded conducting hollow sphere, and (c) dielectric loaded dipole antenna: cross-sectional view, *a*=0.1mm, *b*=2.5mm, *h*=|*c*-*b*|=0.5mm, *d*=5mm, r_0=0.1mm, *H*=2.4mm, L_d=4.9mm, and the dipole radius, r_d, is equal to 0.1mm.

To determine the modal coefficients, we enforce the field continuities as Table 1.

Table 1: Boundary conditions

Layer	Electric Field	Magnetic Field	Limit
I,II	$E_\theta^{II}=\begin{cases}E_\theta^{I} & \alpha_1^q<\theta<\alpha_2^q\\ 0 & otherwise\end{cases}$	$H_\varphi^{i}+H_\varphi^{I}=H_\varphi^{II}$	$r=a$
II, III	$E_\theta^{III}=\begin{cases}E_\theta^{II} & \alpha_1^q<\theta<\alpha_2^q\\ 0 & otherwise\end{cases}$	$H_\varphi^{III}=H_\varphi^{II}$	$r=b$
III, V	$E_\theta^{III}=\begin{cases}E_\theta^{V} & \alpha_1^q<\theta<\alpha_2^q\\ 0 & otherwise\end{cases}$	$H_\varphi^{III}=H_\varphi^{V}$	$r=c$
VI, V	$E_\theta^{VI}=\begin{cases}E_\theta^{V} & \alpha_1^q<\theta<\alpha_2^q\\ 0 & otherwise\end{cases}$	$H_\varphi^{VI}=H_\varphi^{V}$	$r=d$
III, IV	$E_r^{IV}=E_r^{III}$	$H_\varphi^{VI}=H_\varphi^{III}$	$b<r<c$, $\theta=\alpha_{1,2}^q$

Applying orthogonal integrals and mathematical manipulation some can write the equations as follow, [18]

$$C_n=-\sqrt{\frac{\mu_I\varepsilon_I}{\mu_{II}\varepsilon_{II}}}\frac{2n+1}{2n(n+1)}\frac{1}{\hat{J}'_n(k_I a)}\sum_{l=0}^{L-1}\sum_{v=0}^{\infty}\left[D_v^{l,II}\hat{J}'_{\xi_v^l}(k_{II}a)+E_v^{l,II}\hat{N}'_{\xi_v^l}(k_{II}a)\right]I_{vn}^{l,II}, \tag{9}$$

$$\sum_{l=0}^{L-1}\sum_{v=0}^{\infty}\left\{\begin{aligned}&D_v^{l,II}\left[\hat{J}'_{\xi_v^l}(k_{II}a)X_{uv}^{ql}-\hat{J}_{\xi_v^l}(k_{II}a)K_v^{l,II}\delta_{ql}\delta_{uv}\right]\\&+E_v^{l,II}\left[\hat{N}'_{\xi_v^l}(k_{II}a)X_{uv}^{ql}-\hat{N}_{\xi_v^l}(k_{II}a)K_v^{l,II}\delta_{ql}\delta_{uv}\right]\end{aligned}\right\} \tag{10}$$
$$=-\frac{\mu_{II}Ja^2}{4\pi}L_u^q+\frac{\mu_{II}}{\mu_I}\sum_{n=0}^{\infty}a_n\hat{J}_n(k_I a)I_{un}^{q,II},$$

$$\sum_{l=0}^{L-1}\sum_{v=0}^{\infty}\left[D_v^{l,\gamma}\hat{J}'_{\xi_v^l}(k_\gamma r)+E_v^{l,\gamma}\hat{N}'_{\xi_v^l}(k_\gamma r)\right]K_v^{l,\gamma}$$
$$=\sqrt{\frac{\mu_\gamma\varepsilon_\gamma}{\mu_{\gamma'}\varepsilon_{\gamma'}}}\sum_{l=0}^{L-1}\sum_{v'=0}^{\infty}\begin{bmatrix}D_{v'}^{l,\gamma'}\hat{J}'_{\xi_{v'}^l}(k_{\gamma'}r)\\+E_{v'}^{l,\gamma'}\hat{N}'_{\xi_{v'}^l}(k_{\gamma'}r)\end{bmatrix}K_{v'}^{l,\gamma\gamma'}, \tag{11}$$

$$\sum_{l=0}^{L-1}\sum_{v=0}^{\infty}\left[D_v^{l,\gamma}\hat{J}_{\xi_v^l}(k_\gamma r)+E_v^{l,\gamma}\hat{N}_{\xi_v^l}(k_\gamma r)\right]K_v^{l,\gamma}$$
$$=\frac{\mu_\gamma}{\mu_{\gamma'}}\sum_{l=0}^{L-1}\sum_{v'=0}^{\infty}\begin{bmatrix}D_{v'}^{l,\gamma'}\hat{J}_{\xi_{v'}^l}(k_{\gamma'}r)\\+E_{v'}^{l,\gamma'}\hat{N}_{\xi_{v'}^l}(k_{\gamma'}r)\end{bmatrix}K_{v'}^{l,\gamma\gamma'}, \tag{12}$$

$$\sum_{v=0}^{\infty}\xi_v^l\left(\xi_v^l+1\right)\begin{bmatrix}D_v^{l,III}U_v\\+E_v^{l,III}U_{vw}\end{bmatrix}R_v^{l,III}(\cos\theta_0)=$$
$$\frac{\mu_{III}\varepsilon_{III}}{\mu_{IV}\varepsilon_{IV}}\sum_{v'=0}^{\infty}\xi_{v'}^l\left(\xi_{v'}^l+1\right)\begin{bmatrix}D_{v'}^{l,IV}U_{v'v}\\+E_{v'}^{l,IV}U_{v'w}\end{bmatrix}R_{v'}^{l,IV}(\cos\theta_0), \tag{13}$$

$$\sum_{l=0}^{L-1}\sum_{v=0}^{\infty}\left\{\begin{aligned}&D_v^{l,V}\left[\hat{J}'_{\xi_v^l}(k_V d)\Psi_{uv}^{ql}-\hat{J}_{\xi_v^l}(k_V d)K_v^{l,V}\delta_{ql}\delta_{uv}\right]\\&+E_v^{l,V}\left[\hat{N}'_{\xi_v^l}(k_V d)\Psi_{uv}^{ql}-\hat{N}_{\xi_v^l}(k_V d)K_v^{l,V}\delta_{ql}\delta_{uv}\right]\end{aligned}\right\}=0, \tag{14}$$

$$F_n=-\sqrt{\frac{\mu_{VI}\varepsilon_{VI}}{\mu_V\varepsilon_V}}\frac{2n+1}{2n(n+1)}\frac{1}{\hat{H}_n'^{(1)}(k_{VI}d)}\sum_{l=0}^{L-1}\sum_{v=0}^{\infty}\left[D_v^{l,V}\hat{J}'_{\xi_v^l}(k_V d)+E_v^{l,V}\hat{N}'_{\xi_v^l}(k_V d)\right]I_{vn}^{l,V}, \tag{15}$$

where $\gamma=II,V,\ \gamma'=III,\ r=b,c,\ and\ \theta_0=\alpha_1^l,\alpha_2^l$.

The required definitions are illustrated in the appendix. For a single slot configuration (biconical antenna loaded with a dielectric, Fig.1-b), due to the magnetic field boundary condition between region III and IV, $R_v^{l,\gamma}(\cos\theta)$ has been simplified as

$$R_v^{1,\gamma}(\cos\theta)=\begin{cases}\begin{cases}Q_{\xi_v^l}(\cos\theta) & v=0\\ Q_{\xi_v^l}(\cos\alpha_2)P_{\xi_v^l}(\cos\theta)-P_{\xi_v^l}(\cos\alpha_2)Q_{\xi_v^l}(\cos\theta) & v\geq 1\end{cases} & II,V\\[2ex] P_{\xi_v^l}(\cos\theta)+\left(\frac{\mu_{III}}{\mu_{IV}}-1\right)\left[\frac{P'_{\xi_v^l}(\cos\alpha_1)-P'_{\xi_v^l}(\cos\alpha_2)}{Q'_{\xi_v^l}(\cos\alpha_1)-Q'_{\xi_v^l}(\cos\alpha_2)}\right]Q_{\xi_v^l}(\cos\theta) & III\\[2ex] P_{\xi_v^l}(\cos\theta) & IV\end{cases}. \tag{16}$$

Finally, the unknown coefficients are
C_n, D_v^{II}, E_v^{II}, D_v^{III}, E_v^{III}, D_v^{IV}, E_v^{IV}, D_v^{V}, E_v^{V}, F_n.

III. NUMERICAL ANALYSIS

From the formulas presented in the previous section, it is straightforward to write short programs that illustrate the difference between the different types of material inclusions. To this aim, the cone angle of the biconical antenna is selected to be as small as possible, e.g., $2\alpha_1$=2.5 degree. It should be noted that, based on [12-13], it is well known that the input impedance of a biconical antenna changes significantly by changing cone angle. Hence the input impedance of a biconical antenna is investigated with regards to its cone angle. The inverse radiation impedance Z_v for biconical antennas is given by [11]

$$Z_v=\frac{j\eta_2\sin\alpha_1\ln\left(\cot\frac{\alpha_1}{2}\right)\sum_{v=0}^{\infty}\begin{bmatrix}D_v^{II}\hat{J}_{\xi_v}(k_{II}b)\\+E_v^{II}\hat{N}_{\xi_v}(k_{II}b)\end{bmatrix}\left.\frac{\partial R_{\xi_v}(\cos\theta)}{\partial\theta}\right|_{\theta=\alpha_1}}{\pi\left[D_0^{II}\hat{J}'_0(k_{II}b)+E_0^{II}\hat{N}'_0(k_{II}b)\right]}. \tag{17}$$

The analytic simulations have been compared with the CST simulation results of an equivalent dipole antenna (radius, r_d). The results have been presented in Fig. 2. According to this figure, for the antenna radius r_d <0.01λ (≈biconical antenna $2\alpha_1$≤3.4 degree, with regards to f=25GHz as main frequency) the loaded dipole may be considered as a limit case of a loaded biconical antenna (the approximation meet numerical simulations with good agreement). The simulation parameters are: a=0.1mm, b=2.5mm, h=0.5mm, d=5mm, r_0=0.1mm, H=2.4mm, L_d=4.9mm, ε_r=2.2, and μ_r=1. For the radius $0.01\lambda<r_d<0.02\lambda$, the antenna input impedance has been extracted approximately, and larger values cause significant errors in impedance computations.

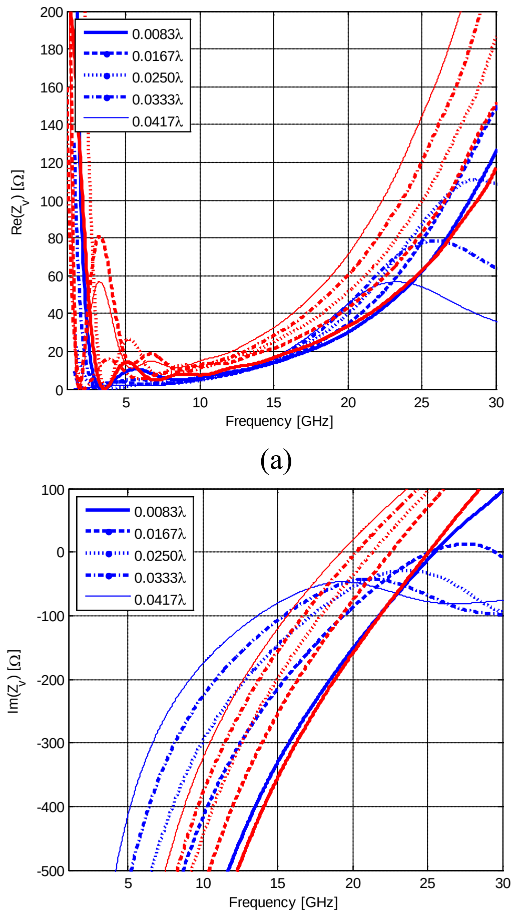

(a)

(b)

Fig. 2. Input impedance of a DPS-loaded dipole v.s. dipole radius, (a) real, and (b) imaginary parts: analytical (Blue) against numerical results (Red). Analytical results are obtained using proposed analytical expressions; while the numerical results are extracted using CST software.

A. Dielectric-covered biconical antennas

To validate the proposed method, it is useful to consider a conventional covered biconical antenna (Fig. 3) as the first limiting case. The input impedance of a thin biconical antenna embedded in dielectric material has been derived by Tai [14]. A slightly more general expression applicable to a biconical antenna embedded in a lossless material of arbitrary permeability and permittivity has been given by [15]. Assuming $L=1$, the region III fills by PEC, and $k_1 a << 1$; the slotted sphere becomes a simple biconical antenna, (Fig. 3). In Fig. 4, the effects of the numbers of modes in computation convergence have been depicted. It is clear that good convergence has been achieved.

In Fig. 5, the analytic results for the return loss of a biconical antenna have been compared with CST simulation results. As it is stated before, the antenna cone angle is $2\alpha_1$=2.5 degree. According to this figure, a good agreement has been achieved between analytic and numeric simulations.

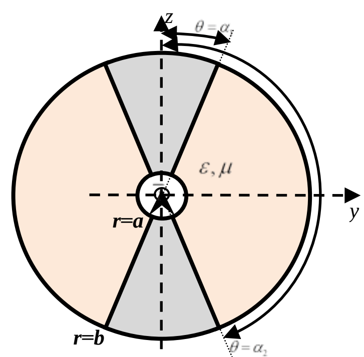

Fig. 3. Dielectric-covered biconical antenna: cross-sectional view, a=0.1mm, b=5mm, $\varepsilon_r=\mu_r=1$.

B. Dielectric-loaded biconical antennas

In order to demonstrate the capability of the MTM loading to realize a miniaturized antenna, two examples are studied here. The first one is a dipole antenna filled with double positive (DPS) material inclusions, (ε_r=2.2 and μ_r=1). A DNG-loaded dipole antenna, whose parameters are labeled in Fig. 1-c, is also studied.

Here, the Drude model [16] is used to simulate the MTM inclusions, since it can yield a negative real part of the permittivity/permeability over a wide frequency range. For the DNG inclusions, both μ and ε obey the Drude model (with plasma frequency $\omega_p=15\times10^{10}$ rad/s and collision frequency f_c=0.01GHz) as

$$\xi_r(\omega)=\xi_\infty-\frac{\omega_p^2}{\omega(\omega-iv_c)}\quad \xi\in\{\varepsilon,\mu\}. \tag{18}$$

It should be noted that, this selection has been affected by all the other relative parameters, e.g., *k*, [17]. In Fig. 6, the effects of the numbers of modes in computation convergence have been presented. Again, it is clear that good convergence has been obtained. The analytical and simulated results for the reflection coefficient of the DPS- and DNG-loaded dipole antennas are presented in Fig. 7. As can be seen from this figure, the analytical results for the reflection coefficient of a loaded dipole are in good agreement with the CST simulation results. Simulations show that for the dipole antenna loaded with DNG-inclusions, an additional resonance frequency is introduced at the frequencies lower than the antenna resonant frequency where the antenna radiates an omnidirectional radiation pattern.

In contrast, for the dipoles loaded with DPS-inclusions, changing DPS locations on the antenna arms causes no resonances at frequencies lower than the main resonant frequency. An important advantage of the proposed antenna is that the dipole length does not need to be increased to lower the resonant frequency. Consequently, a compact antenna is obtained. The proposed method, suggested a bandwidth of 0.3% at 2.2GHz (which is wider than the bandwidth of other miniaturized MTM loaded dipoles [1-2]) while it means 11.8 times frequency reduction with regards to resonance frequency of DPS loaded antenna (26GHz). Since changing the locations and dimensions of the DPS/DNG materials does not have any significant effect on the antenna radiation patterns, the proposed antennas radiate omnidirectional radiation patterns at all resonant frequencies. However, these are not plotted here for the sake of brevity.

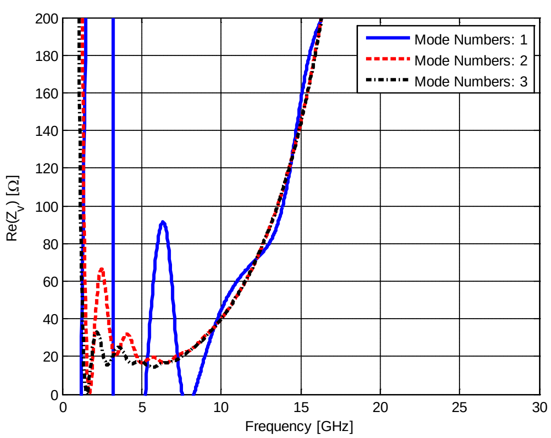

(a)

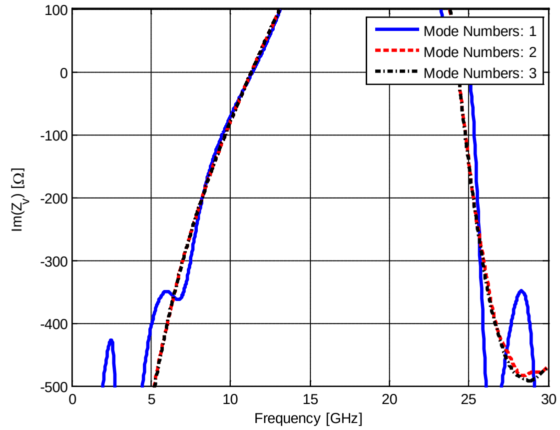

(b)

Fig. 4. Convergence analysis of the dielectric-covered biconical antenna, input impedance, (a) real, and (b) imaginary parts.

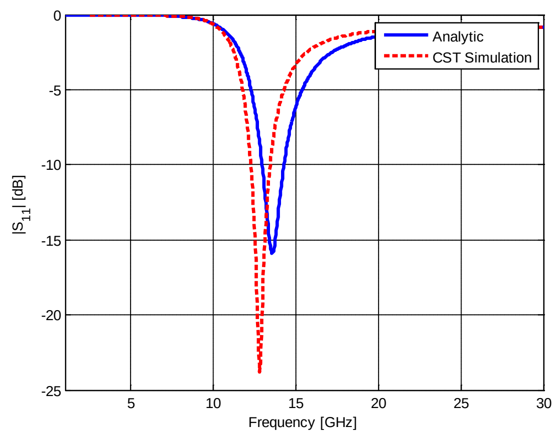

Fig. 5. $|S_{11}|$ [dB] of a dielectric-covered biconical antenna: analytical against numerical results. Analytical results are obtained using proposed analytical expressions; numerical results are computed by CST software.

IV. CONCLUSION

The behavior of a biconical/dipole antenna loaded with MTM inclusions has been examined both analytically and numerically. The theory is compared with different simulation results resulting in a very good agreement between them. The analytical investigations also reveal that embedding DNG-inclusions in a simple biconical/dipole antenna can provide an opportunity to design miniaturized antenna.

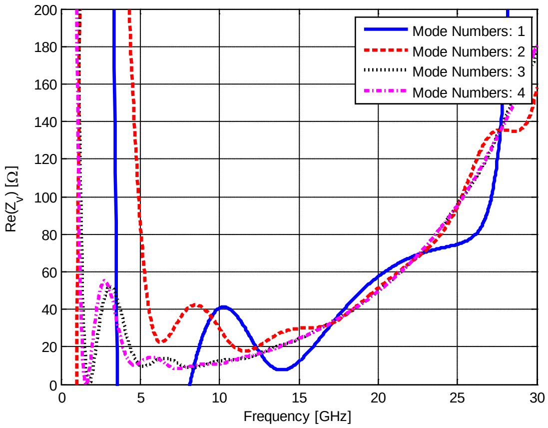

(a)

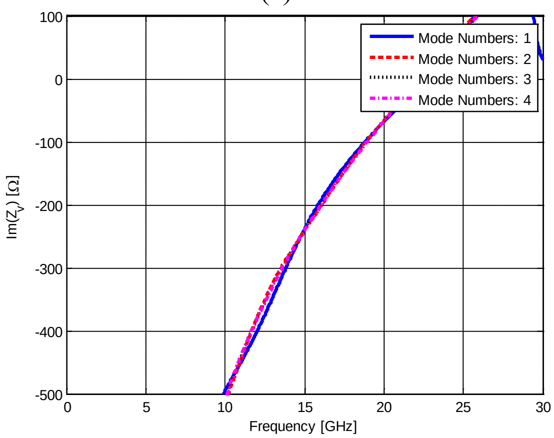

(b)

Fig. 6. Convergence analysis of the dielectric-loaded biconical antenna, input impedance (a) real, and (b) imaginary parts.

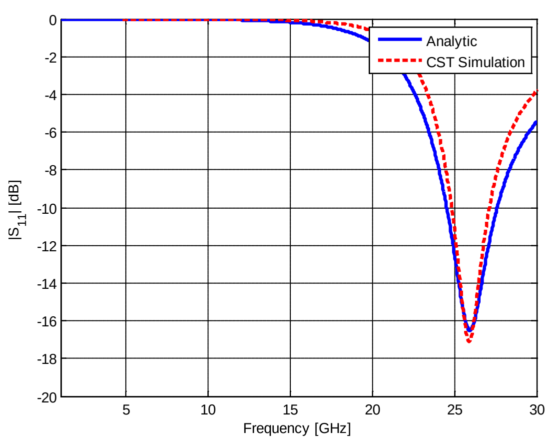

(a)

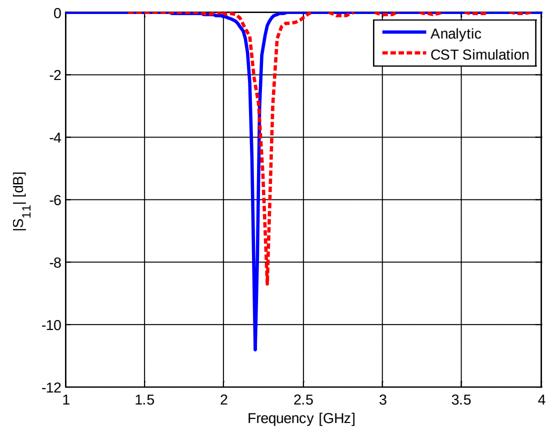

(b)

Fig. 7. $|S_{11}|$ [dB] of a (a) dielectric, and (b) DNG-loaded biconical antenna: analytical against numerical results. Analytical results are obtained using proposed analytical expressions; numerical results are computed by CST software.

ACKNOWLEDGMENT

The authors would like to thank Iran Telecommunication Research Centre (ITRC) for its financial supports.

APPENDIX

In Eqs. (9)-(15) the required definitions are defined as follow:

$$I_{vn} = -\int_{\alpha_1}^{\alpha_2} \frac{\partial}{\partial\theta} R_v(\cos\theta) \frac{\partial}{\partial\theta} P_n(\cos\theta) \sin\theta d\theta, \quad \text{(A-1)}$$

$$X_{uv}^{ql} = \sqrt{\frac{\mu_{II}\varepsilon_I}{\mu_I\varepsilon_{II}}} \sum_{n=1}^{\infty} \frac{2n+1}{2n(n+1)} \frac{\hat{J}_n(k_I a)}{\hat{J}_n'(k_I a)} I_{un}^{q,II} I_{vn}^{l,II}, \quad \text{(A-2)}$$

$$L_u^q = \int_{\alpha_1^l}^{\alpha_2^l} \frac{\partial}{\partial\theta}\left(\frac{e^{ik_I R}}{R}\right) \frac{\partial R_u^q(\cos\theta)}{\partial\theta} \sin\theta d\theta, \quad \text{(A-3)}$$

$$K_v^{l,\gamma} = \int_{\alpha_1^l}^{\alpha_2^l} \frac{\partial}{\partial\theta} R_v^{l,\gamma}(\cos\theta) \frac{\partial}{\partial\theta} R_{v'}^{l,\gamma}(\cos\theta) \sin\theta d\theta, \quad \gamma = II, V \quad \text{(A-4)}$$

$$= \begin{cases} Q_0(\cos\alpha_2^l) - Q_0(\cos\alpha_1^l) & v = 0 \\ \xi_v^l(\xi_v^l + 1) \int_{\alpha_1^l}^{\alpha_2^l} \left[R_v^{l,\gamma}(\cos\theta)\right]^2 \sin\theta d\theta & v \geq 1 \end{cases}, \gamma = II, V,$$

$$K_v^{l,\gamma\gamma'} = \int_{\alpha_1^l}^{\alpha_2^l} \frac{\partial}{\partial\theta} R_v^{l,\gamma}(\cos\theta) \frac{\partial}{\partial\theta} R_{v'}^{l,\gamma'}(\cos\theta) \sin\theta d\theta, \begin{matrix} \gamma = II, V \\ \gamma' = III \end{matrix}, \quad \text{(A-5)}$$

$$\Psi_{uv}^{ql} = \sqrt{\frac{\mu_V\varepsilon_{VI}}{\mu_{VI}\varepsilon_V}} \sum_{n=1}^{\infty} \frac{2n+1}{2n(n+1)} \frac{\hat{H}_n^{(2)}(k_{VI} d)}{\hat{H}_n'^{(2)}(k_{VI} d)} I_{un}^{q,V} I_{vn}^{l,V}. \quad \text{(A-6)}$$

REFERENCES

[1] Q. Liu, P. S. Hall, and A. L. Borja, "Efficiency of electrically small dipole antennas loaded with

left-handed transmission lines," *IEEE Trans. Antennas Propag.*, vol. 57, no. 10, pp. 3009-3017, 2009.
[2] H. Iizuka and P. S. Hall, "Left-handed dipole antennas and their implementations," *IEEE Trans. Antennas Propag.*, vol. 55, no. 5, pp. 1246-1253, 2007.
[3] A. Jafargholi, M. Kamyab, and M. Veysi, "Artificial magnetic conductor loaded monopole antenna" *IEEE Antennas Wireless Propag. Lett.*, vol. 9, pp. 211-214, 2010.
[4] A. Jafargholi, M. Kamyab, M. Rafaei, M. Veysi, "A compact dual-band printed dipole antenna loaded with CLL-based metamaterials", *International Review of Electrical Engineering*, vol. 5, no. 6, pp. 2710-2714, 2010.
[5] M. Rafaei Booket, M. Kamyab, A. Jafargholi, and S. M. Mousavi, "Analytical modeling of the printed dipole antenna loaded with CRLH structures," *Progress In Electromagnetics Research B*, vol. 20, pp. 167-186, 2010.
[6] K. M. Z. Shams and M. Ali, "Analyses of a Dipole Antenna Loaded by a Cylindrical Shell of Double Negative (DNG) Metamaterial, "*International Journal of Antennas and Propagation*, Article ID 97481, 10 pages, 2007.
[7] R. Beggs, J. Luebbers, and K. Chamberlin, "Finite difference time-domain calculation of transients in antennas with nonlinear loads," *IEEE Trans. Antennas Propag*., vol. 41, no. 5, p. 566, May 1993.
[8] T. F. Kennedy, K. D. Fasenfest, S. A. Long and J. T. Williams, "Modification and Control of Currents on Electrically Large Wire Structures Using Composite Dielectric Bead Elements, "*IEEE Trans. Antennas Propag*., vol. 54, no. 12, pp. 3608–3613, 2006.
[9] J. D. Kraus, and R. J. Marhefka, *Antennas for All Applications*, McGraw-Hill, 2002.
[10] R. E. Collin, and F. J. Zucker, *Antenna Theory*, McGraw-Hill, 1969.
[11] J. S. Ock, and H. J. Eom, "Radiation of a Hertzian Dipole in a Slotted Conducting Sphere," *IEEE Trans. Antennas Propagat*., vol. 57, no. 12, pp. 3847–3851, 2009.
[12] R. W. king and G. S. Smith, *Antenna in Matter, Fundamentals, Theory, and Applications*, MIT Press, 1981.
[13] S. Saoudy and M. Hamid, "Input Admittance of a Biconical Antenna with Wide Feed Gap," *IEEE Trans. Antennas Propag*., vol. 38, no. 11, pp. 1784–1790, 1990.
[14] C. T. Tai, "On the theon; of biconical antennas," *J. of Appl. Phys*., vol. 19, pp. 1155-1160, 1958.
[15] C. Polk, "Resonance and Supergain Effects in Small Ferromagnetically or Dielectrically Loaded Biconical Antennas, "*IRE Trans. Antennas Propag*., pp. 414-423, 1959.
[16] M. Rafaei Booket, A. Jafargholi, M. Kamyab, H. Eskandari, M. Veysi, and S. M. Mousavi, "A Compact Multi-Band Printed Dipole Antenna Loaded with Single-Cell MTM," pending publication in *IET Microwave Antenna Propag*., 2011.
[17] N. Engheta and R. Ziolkowski, *Metamaterials: Physics and Engineering Explorations*, Wiley, 2006.
[18] A. Jafargholi, and M. Kamyab, *Metamaterials in Antenna Engineering, Theory and Applications*, LAP Lambert Academic Publishing, Germany, 2011.

Amir Jafargholi received the Ph.D. degree in Electrical Engineering from K.N. Toosi University of Technology, Tehran, Iran, in 2011. He is the coauthor of about 50 scientific contributions published in international books, journals and peer-reviewed conference proceedings. His research interest includes the applications of metamaterials in the analysis and synthesis of antennas. Dr. Jafargholi was a recipient of a Student's Best Thesis National Festival award for his BS thesis, on May 2006. He was a recipient of the 22nd Khawarizmi International and 13th Khawarizmi Youth Award on Jan. 2009 and Oct. 2011, respectively. He was also the recipient of Research Grant Awarded in Metamaterial 2010.

Manouchehr Kamyab received the B.S. and M.S. from the University of Tehran, Tehran, Iran, and the PhD degree from Michigan State University, in 1982, in Electrical Engineering. His research interest includes the metamaterials and their applications in antenna engineering, electrically small antennas, microwave and millimeter-wave circuits, and mobile communication systems. He is currently an associate professor in the Department of Electrical Engineering, K.N. Toosi University of Technology, Tehran, Iran. Dr. Kamyab is leading a group of graduate students in the areas of negative-refraction metamaterials and their microwave applications, integrated antennas and components for broad-band wireless telecommunications, novel antenna beam-steering techniques, millimeter and submillimeter-wave circuits, as well as scattering and inverse scattering problems.

Analysis of Microstrip Antennas using The Volume Surface Integral Equation Formulation and the Pre-Corrected Fast Fourier Transform Method

Ke Xiao, Ya-Nan Li, Fei Zhao, Shun-Lian Chai, and Jun-Jie Mao

College of Electronic Science and Engineering
National University of Defense Technology, Changsha, Hunan, 410073, China
xiaoke_e@hotmail.com, maojj_43@163.com

Abstract **─** A rigorous and effective analysis based on the volume-surface integral equation (VSIE) formulation and pre-corrected-fast Fourier transform method (P-FFT) is presented for the problems of finite microstrip antennas which are modeled by combined conducting and dielectric materials. Several typical microstrip antennas and conformal microstrip antenna arrays are reconsidered; the comparisons of results from calculation and measurement validate the algorithm. Different feed methods are also considered to excite the antennas and conformal arrays. All the problems could be solved on a small computer with high efficiency and good precision.

Index Terms **─** Conformal antenna, microstrip antenna, precorrected-fast Fourier transform method, volume-surface integral equation.

I. INTRODUCTION

Microstrip patch antennas have been widely used in satellite communications, aircrafts, radars, biomedical applications, and reflector feeds, due to their advantages of low profile, simple structure, low cost and compatibility with integrated circuits. It is important to develop an efficient electromagnetic numerical method to analyze antennas with good precision.

There are always two approaches to analyze microstrip antennas, one approach is to model the antenna with infinite ground and substrate, derive the Green's function to the special multilayer structure of the antenna [1]; then, the unknown surface currents of the patch can be solved by full-wave method. This approach does not account for the edge effects of a finite antenna, and it will be very difficult to get the related Green's function when the microstrip antenna is conformed onto a host with sophisticated and irregular shapes [2]. Another approach is to deal with the finite antenna directly by full-wave method, one of the popular numerical methods for this problem is based on the surface integral equation (SIE) formulation [3] or the hybrid volume-surface integral equation (VSIE) [4,5] formulation, for thin dielectric sheet problem, the volume integral approach seems a better alternative than the surface integral approach to the thin sheet problem [6]. In this paper, the VSIE formulation is applied to solve problems consisting of arbitrarily composite conducting-dielectric objects.

But this approach is considerably difficult for electrical large antenna arrays because of the necessity of solving a large matrix equation, which requires a large computer memory and CPU time. Domain decomposition method (DDM) [7], characteristic basis function method (CBFM) [8], and parallel computation techniques [9] could be applied to decompose the large problems to many smaller problems and alleviate the problem by assigning the memory requirements and CPU time. Fast solvers could also be used to reduce the storage memory and CPU time to some reasonable extent, such as conjugate gradient fast Fourier transform method (CG-FFT) [10], fast multipole algorithm (FMM), or multilevel fast multipole algorithm (MLFMA) [11,12], adaptive integral method (AIM) [13] and pre-corrected-fast Fourier transform method (p-FFT) [14,15].

Submitted On: Oct. 25, 2010
Accepted On: Aug. 21, 2011

Among these types of fast algorithms, FFT-form algorithms have relatively simple implementation on personal computers as compared to the FMM. CG-FFT method requires the integral equation to be discretized on rectangular grids which has limited its usage to conformal antenna objects, and as compared in [16], p-FFT can use larger grid spacing than the AIM, so the p-FFT algorithm is applied in this paper.

Several typical microstrip antennas or arrays including wideband microstrip antenna, microstrip patch antenna, and microstrip conformal arrays are characterized, and their respective numerical results are presented to demonstrate good accuracy and efficiency of the present design. Two feeding models are used in the examples including probe feed model [15,17] and microstrip line feed model [18], in which, the probe feed model use the uniform prism as demonstrated in [17], so RWG basis can be used for probe junction modeling.

II. FORMULATIONS AND EUQATIONS

Formulations for VSIE [5, 19, 20] and the main progress of p-FFT method are discussed here. The method in [21] is used to solve the singularity problems of potential integrations. Incomplete LU factorization with threshold (ILUT) pre-conditioner [22] is applied to improve the condition number of the impedance matrix, and the generalized minimum residual method (GMRES) is employed to solve the matrix equation for a faster convergence [22].

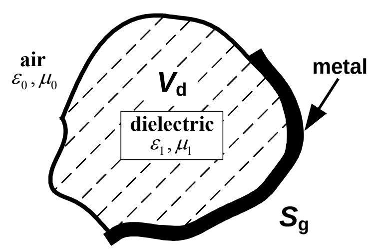

Fig. 1. Composite dielectric and metal model.

A. Coupled volume-surface integral equation

The mixed conduction-dielectric problem is considered here as shown in Fig. 1. To the dielectric obstacles, the volume equivalence theorem is used [23], then the scattered fields are produced by the equivalent volume polarization currents $\boldsymbol{J}_d$. To consider the scattering of perfectly conducting surfaces, the physical equivalent theorem can be used [23], and the fields are best determined using surface equivalent current densities $\boldsymbol{J}_c$. For all these currents are situated in free space, so the free-space dyadic Green's function could be utilized in the computation of the scattered fields $\boldsymbol{E}^s(\boldsymbol{r})$, which could be expressed as

$$\boldsymbol{E}_\alpha^s = i\omega\mu_b \int_\alpha \overline{\overline{G}}(\boldsymbol{r},\boldsymbol{r}')\bullet\boldsymbol{J}_\alpha d\boldsymbol{r}', \ \alpha = S \text{ or } V, \quad (1)$$

where $\overline{\overline{G}}(\boldsymbol{r},\boldsymbol{r}')$ is the dyadic Green's function, expressed as

$$\overline{\overline{G}}(\boldsymbol{r},\boldsymbol{r}') = \left(\overline{\overline{I}} + \nabla\nabla/k_b^2\right)\frac{e^{ik_b|\boldsymbol{r}-\boldsymbol{r}'|}}{4\pi|\boldsymbol{r}-\boldsymbol{r}'|}. \quad (2)$$

k_b is the wave number for the background media.

Using boundary condition, the field integral equations are given by

$$\frac{\boldsymbol{D}(\boldsymbol{r})}{\varepsilon_1(\boldsymbol{r})} = \boldsymbol{E}^i(\boldsymbol{r}) + \boldsymbol{E}^s(\boldsymbol{r}) \qquad in \ V_d, \quad (3)$$

$$\boldsymbol{E}_{\tan}^i = -\boldsymbol{E}_{\tan}^s \qquad on \ S_g, \quad (4)$$

where V_d is the volume of the dielectric substrate, S_g is the surfaces of the metal. $\boldsymbol{D}(\boldsymbol{r})$ is the electric flux density in the dielectric region. $\boldsymbol{E}^i$ is the field due to the impressed source. As expressed in (1), $\boldsymbol{E}^s$ is the scattered field due to the currents of the conductors $\boldsymbol{J}_c$ and the equivalent volume currents $\boldsymbol{J}_d$ in the dielectric region, which are expanded as follows

$$\boldsymbol{J}_c(\boldsymbol{r}) = \sum_{n=1}^{N_s} I_n^S f_n^S(\boldsymbol{r}), \quad \boldsymbol{r} \text{ on } S_g, \quad (5)$$

$$\boldsymbol{J}_d(\boldsymbol{r}) = j\omega\sum_{n=1}^{N_V} I_n^V \kappa(\boldsymbol{r}) f_n^V(\boldsymbol{r}), \quad \boldsymbol{r} \text{ in } V_d. \quad (6)$$

RWG basis functions [19] and SWG basis functions [20] are used here to discretize the models. Galerkin's method [24] is used for MoM, then the matrix equation is built for the solution of the unknown surface and volume currents. To solve the problem directly, the memory requirement is of the order $O(N^2)$, and the CPU is of the order $O(N^3)$. For electrically large problems, it is inefficient to use MoM directly, while p-FFT method could be used to alleviate the problem to some extent.

B. Pre-corrected-FFT solution of VSIE

The pre-corrected-FFT method considers the near- and far- zone interactions separately when evaluating a matrix-vector product, namely

$$\boldsymbol{Z} \cdot \boldsymbol{I} = \boldsymbol{Z}^{near} \cdot \boldsymbol{I} + \boldsymbol{Z}^{far} \cdot \boldsymbol{I}. \qquad (7)$$

The near-zone interactions within an appropriate separation between the source and observation points are computed directly and stored. The far-zone interactions beyond the predefined separation are calculated using an approximate four-step (projection, FFT, interpolation, and pre-correction) procedure. Exactly, for surface integral equation (SIE), the memory requirement and computational complexity are of $O\left(N^{1.5}\right)$ and $O\left(N^{1.5}\log N\right)$, respectively, and for a solution to volume integral equation (VIE) requires $O\left(N\right)$ and $O\left(N\log N\right)$ operations, respectively.

III. DESIGN OF MICROSTRIP ANTENNAS

In this section, some typical microstrip antennas are analyzed using the method mentioned above, examples include E-shaped patch antenna [25], microstrip patch antenna [26], and conformal microstrip patch array [27] are reconsidered.

A. E-shaped antenna

This sub-section reconsiders the wideband E-shaped antenna proposed in [25]. Figure 2 shows the meshed model and dimensions of the antenna, the distance between the E-shaped patch and ground is 15 mm. To mesh the conductor 2155 triangular patches are used in 3348 unknowns. The calculated results are compared with the simulated results based on the commercial software (Ansoft HFSS) as shown in Fig. 3. From the results of MoM, the second resonant frequency has an offset of about 120 MHz to the measured result, and about 50 MHz to the HFSS results. The same problem exists in the following example, and will be explained then.

B. Microstrip patch antenna

The example considered here is from [26] as shown in Fig. 4. The thickness of the substrate to the antenna is 0.794 mm, the relative permittivity $\varepsilon_r = 2.2$. In order to build an accurate model to simulate the port of a microstrip line, a two-dimension eigenmode problem on the port's surface should be solved firstly [28]. Here, a simplified port model is used as shown in Fig. 4, where, the field at the port's face is compared near the excited gaps, a lumped voltage source is applied at the gaps. In the model, the feed strip line is shorted to the ground, which will introduce a self-inductor to the microstrip input port [28].

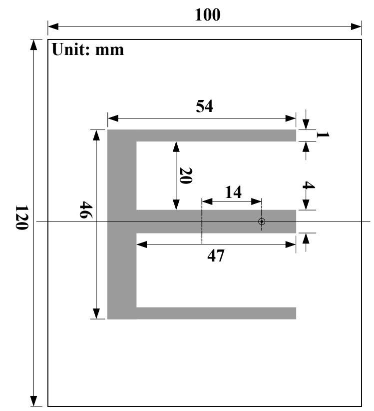

Fig. 2. Model of E-shaped antenna.

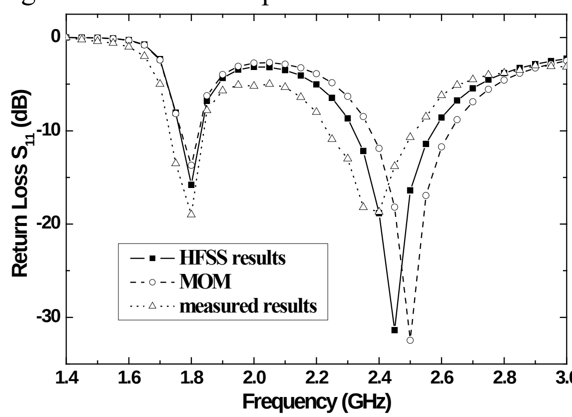

Fig. 3. Compared results of S_{11} (dB).

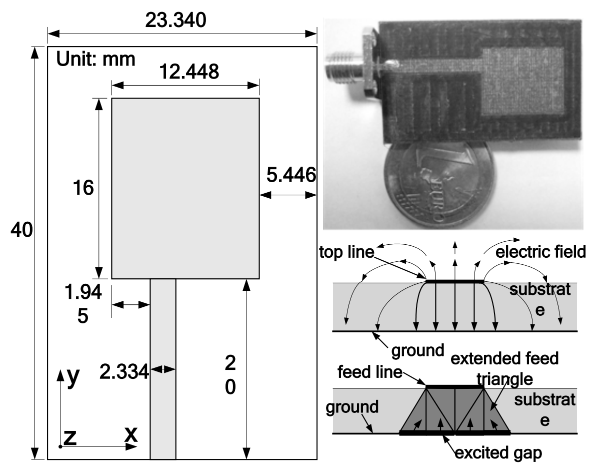

Fig. 4. Microstrip patch antenna model.

The antenna in Fig. 4 is modeled by 2299 tetrahedral elements and 962 triangular patches, with 6795 unknowns to the whole problem. At a frequency of 7.78 GHz, the p-FFT accelerated method needs about 412 MB memory with the near-zone threshold distance set to 0.27λ, number of near field interactions is 12,935,915. Time for per iteration is 0.147s, a tolerance of 0.1% for GMRES can be achieved in only 21 iterations, total CPU time is 9.25 minutes for the solution. The generalized pencil-of-function method (GPOF) is used to retrieve the input impedance of the antenna [29].

The calculated return loss results are compared with the measured results in Fig. 5. A positive offset of about 180 MHz in the resonant frequency can be observed in Fig. 5. Except for the reasons of meshes density and fabrication error, the error relates to the nature of SWG and RWG or other low-order basis functions. SWG or other low-order dielectric basis functions are unable to exactly satisfy the boundary condition of the vanishing tangential E-field component on the metal-dielectric surface [17]. And for RWG or other low-order surface basis functions, it is difficult to express the fringing currents of conducting patches, according to the fringing effects of patch antenna, the inductive currents change very quickly near the fringe of a patch, and the fringing currents focus to the patch edge which will cause a much more higher current density near the fringe, but RWG basis function can not render the fringe effecting phenomenon very well, that's why the resonant frequency calculated by MoM always has a positive offset to the actual resonant frequency. Another reason is that the feed model used in Fig. 4 has introduced a self-inductance and caused frequency shift due to the strip shorted to the ground. The losses of dielectric and metal are also not considered in the numerical method.

In Fig. 6, the radiation patterns of the calculated results using the method in the paper are compared to the measured results and numerical results using the FDTD [26] and PMCHWT [30] methods, as shown in the diagram, very good agreements are obtained by comparing the calculated results using the method of the paper to the measured results. While in some angles, the results from FDTD method in [26] and PMCHWT method in [30] have a lot of differences from the measured results, the reason for the lack of agreement is that, the finite ground plane is not modeled in the FDTD and PMCHWT solutions [26, 30].

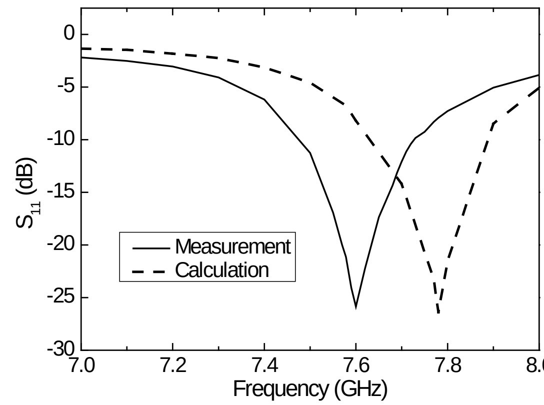

Fig. 5. S_{11} (dB) results comparison.

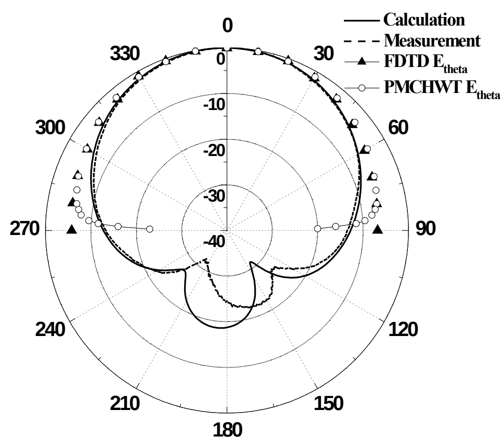

(a) *xoz* plane, E_θ component

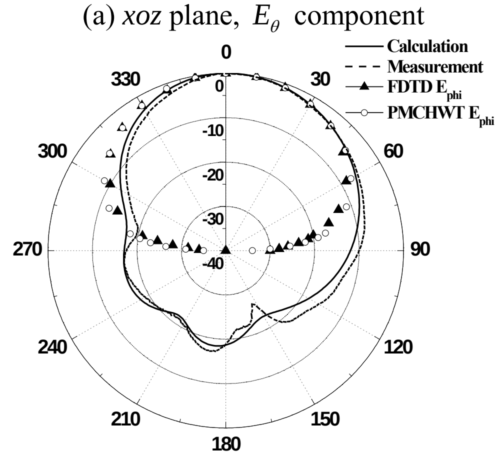

(b) *yoz* plane, E_ϕ component

Fig. 6. Radiation patterns comparison at the resonant frequency, the calculated results are compared with measured results, calculated results based on FDTD in [26] and the numerical results

based on the PMCHWT method in [30]. E_θ component in *xoz* plane and E_Φ component in *yoz* plane are calculated and compared with the measurement.

C. Cylindrical microstrip arrays

Conformal microstrip antenna arrays are usually utilized in reality on surfaces of aircrafts, missiles, or many other land vehicles, which conform to prescribed shapes such as cylinders, cones, spheres, or some other complex geometries. Design of conformal array is a challenging problem for it is much more flexible than designing a planar array.

In [27], two examples of conformal cylindrical arrays were analyzed, assuming that the cylindrical ground plane and substrates have an infinite extent in the axial directions, and the patch surface currents orthogonal to the excitation polarization in each element were neglected, the mutual couplings between array elements were also ignored. In this paper, radiation characteristics of conformal array with different radii (chosen as 50mm, 76mm, and 106mm, respectively) are analyzed and compared.

As shown in Fig. 7, a 4×4 patch antenna array is conformed to a PEC cylinder with finite boundary. The geometry and dimensions of the cylindrical microstrip array calculated are shown in Fig. 7*a*. The interelement spacing is selected to be the same in the $\phi-$ and $z-$ directions. As shown in Fig. 7*a*, the length and width of the microstrip feed line are 4 mm and 1 mm, respectively, the feed point locates with a distance of 0.5 mm to the end of the microstrip feed line. The probe feed model is shown in Fig. 7*b* [17]. For the limitation of our computation condition, in order to reduce the unknowns and memory required, the cylinder is cut by two planes as shown in Fig. 7*a*. The dielectric substrate of array has a thickness of h with relative permittivity $\varepsilon_r = 2.94$. The calculated E-plane (*xoz* plane) and H-plane (*xoy* plane) patterns of the three cases ($a=106$ mm, $a=76$ mm, and $a=50$ mm) are compared as shown in Fig. 8, along with the, measured results provided in [27].

It is observed that the three radiation patterns are almost the same in the E-plane, the relative level of side-lobe will increase as the curvature increases. For the microstrip feeding method, the calculated directive gains of the three cases are 20.36, 19.74, and 17.76, respectively, which will decrease as the curvature increases, Memory requirements and CPU time for p-FFT fast solver used to calculate the examples $a=106$ mm and $a=76$ mm are listed in Table 1. From Table 1, less than 1 GB memories are used to solve the problems. It should be pointed out that, for the limitation of our computation resource, less than 1.2 GB memories could be used, and pre-conditioner is not used in the conformal cases, which causes a lot of time for computation convergence. For all these cases, the tolerance for GMRES is set to 0.01. The convergence rates of probe fed cases are much lower than the microstrip fed cases, as more dense meshes should be applied to model the probe, which resulted in a larger condition number of the matrix.

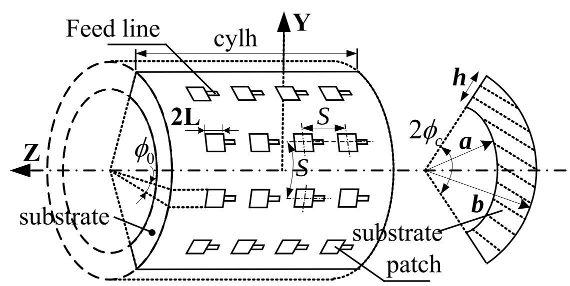

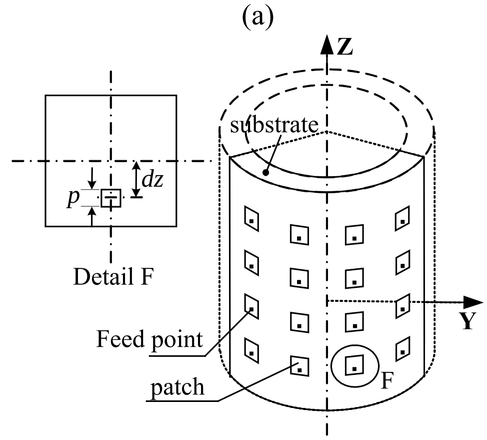

Fig. 7. Geometry of the cylindrical microstrip antenna array, frequency is at 16.2 GHz; a=76 mm, h=0.254 mm, b=a+h, S=15 mm, $2L$=7.2 mm, $2b\phi_0 = 5$ mm, *cylh*=66 mm, $2\phi_c = 46^o$, dz=1 mm, p=0.2 mm. (a) Microstrip-line fed, (b) probe fed.

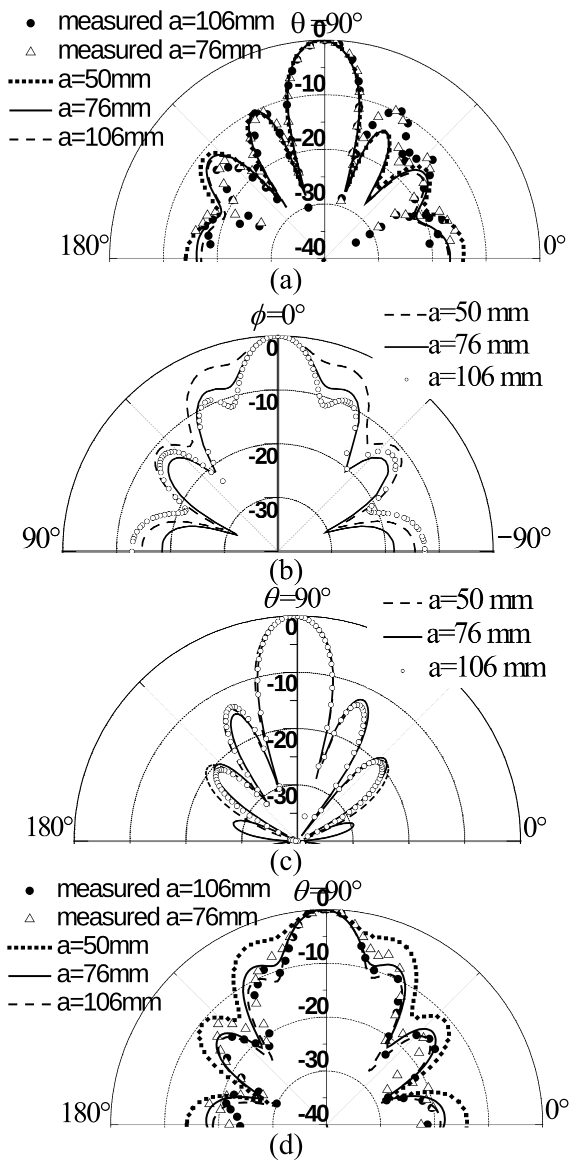

Fig. 8. Calculated and measured patterns [27].
(a) probe feed, E-plane, E_θ component.
(b) probe feed, H-plane, E_θ component.
(c) microstrip-line feed, *E*-plane, E_θ component.
(d) microstrip line feed, *H*-plane, E_θ component.

Table 1: Memory required and CPU time for the calculation of cylindrical arrays

		Cylindrical array			
		a=76mm		*a*=106mm	
		Probe	strip	probe	strip
Unknowns		45939	51224	46544	47158
Near-zone threshold (λ_0)		0.23	0.22	0.245	0.26
Memory (MB)	P-FFT	645	799	737	834
	MoM	55648	60059	49586	50903
Per iteration time (s)		0.82	1.26	1.12	0.87
Total CPU time (h)		12.83	0.87	15.97	1.75

IV. CONCLUSION

The numerical method based on the volume-surface integral equation (VSIE) formulation and pre-corrected-fast Fourier transform method (p-FFT) fast solver is used to analyze the radiation problems of microstrip antennas, probe feed and microstrip line feed methods are both applied in the paper to excite the antennas or arrays. Numerical examples demonstrate that the p-FFT method yields an effective reduction of memory requirement and computational cost for large problems. At the same time, good agreements between calculated results and measured results are obtained. The reasons for the resonant frequency offset problem are analyzed in the paper and the problem remains to be solved.

REFERENCES

[1] C. T. Tai, *Dyadic Green's Functions in Electromagnetic Theory*, CA: Intext Educational Publishers, San Francisco, 1971.

[2] B. R. Piper and N. V. Shuley, “The Design of Spherical Conformal Antennas using Customized Techiniques Based on NURBS,” *IEEE Antennas Propagat. Magazine*, vol. 51, no. 2, pp. 48-60, 2009.

[3] W. J. Zhao, L. W. Li, and K. Xiao, “Analysis of Electromagnetic Scattering and Radiation from Finite Microstrip Structures using an EFIE-PMCHWT Formulation,” *IEEE Trans. Antennas Propagat.*, vol. 58, no. 7, pp. 2468-2473, 2010.

[4] T. W. Dawson, S. Velamparambil, and M. A. Stuchly, “Hybrid Integral Equation and Finite Difference Method for Low-Frequency Electric Induction,” *Applied Computational Electromagnetics Society Journal*, vol. 16, no. 3, pp. 218-227, Nov. 2001.

[5] T. K. Sarkar and E. Arvas, “An Integral Equation Approach to the Analysis of Finite Microstrip Antennas: Volume/Surface Formulation,” *IEEE Trans. Antennas Propagat.*, vol. 38, no. 3, pp. 305-312, 1990.

[6] C. C. Lu and C. Luo, “Comparison of Iteration Convergences of SIE and VSIE for Solving Electromagnetic Scattering Problems for Coated Objects,” *Radio Sci.,* vol. 38, no. 2, pp. 11-1-11-9, 2003.

[7] M. -K. Li and W. C. Chew, “Wave-Field Interaction with Complex Structures using Equivalence Principle Algorithm,” *IEEE Trans. Antennas Propagat.*, vol. 55, no. 1, pp. 130-138, 2007.

[8] R. Mittra, “Characteristic Basis Function Method (CBFM)- An Iteration-Free Domain

Decomposition Approach in Computational Electromagentics," *Applied Computational Electromagnetics Society Journal*, vol. 24, no. 2, pp. 204-223, Apr. 2009.

[9] C. Tom, P. Jonathan, and P. Jean, "Method of Moment Solutions to Scattering Problems in a Parallel Processing Environment," *IEEE Trans. on Magnetics*., vol. 27, no. 5, pp. 3837-3840, 1991.

[10] F. C. Manuel, G. Emilio, and N. Luis, "A Numerical Scheme to Obtain the RCS of Three – Dimensional Bodies of Resonant Size using the Conjugate Gradient Method and the Fast Fourier Transform," *IEEE Trans. Antennas Propagat*., vol. 37, no. 5, pp. 528-537, 1989.

[11] N. Engheta, W. D. Murphy, V. Rokhlin, and M. S. Vassiliou, "The Fast Multipole Method (FMM) for Electromagnetic Scattering Problems," *IEEE Trans. Antennas Propagat*., vol. 40, no. 6, pp. 634-641, 1992.

[12] J. M. Song, C. C. Lu, and W. C. Chew, "Multilevel Fast Multipole Algorithm for Electromagnetic Scattering by Large Complex Objects," *IEEE Trans. Antennas Propagat*., vol. 45, no. 10, pp. 1488-1493, 1997.

[13] E. Bleszynski, M. Bleszynski, and T. Jaroszewicz, "Adaptive Integral Method for Solving Large-Scale Electromagnetic Scattering and Radiation Problems," *Radio Sci*., vol. 31, no. 5, pp. 1225-1251, 1996.

[14] N. Yuan, T. S. Yeo, X. C. Nie, Y. B. Gan, and L. -W. Li, "A Fast Analysis of Scattering and Radiation of Large Microstrip Antenna Arrays," *IEEE Trans. Antennas Propagat*., vol. 51, no. 9, pp. 2218-2226, 2003.

[15] N. Yuan, T. S. Yeo, X. C. Nie, Y. B. Gan, and L. –W. Li, "Analysis of Probe-Fed Conformal Microstrip Antennas on Finite Grounded Substrate," *IEEE Trans. Antennas Propagat.,* vol. 54, no. 2, pp. 554-563, 2006.

[16] X. C. Nie, L. –W. Li, and N. Yuan, "Precorrected-FFT Algorithm for Solving Combined Field Integral Equations in Electromagnetic Scattering," *Journal of Electromagnetic Waves and Applications*, vol. 16, no. 8, pp. 1171-1187, 2002.

[17] S. N. Makarov, S. D. Kulkarni, A. G. Marut, and L. C. Kempel, "Method of Moments Solution for a Printed Patch/Slot Antenna on a Thin Finite Dielectric Substrate using the Volume Integral Equation," *IEEE Trans. Antennas Propagat*., vol. 54, no. 4, pp. 1174-1183, 2006.

[18] Z. A. Maricevic and T. K. Sarkar, "Analysis and Measurements of Arbitrarily Shaped Open Microstrip Structures," *Progress in Electromagnetics Research*, *PIER*, vol. 15, pp. 253-301, 1997.

[19] S. M. Rao, D. R. Wilton, and A. W. Glisson, "Electromagnetic Scattering by Surfaces of Arbitrary Shape," *IEEE Trans. Antennas Propagat.*, vol. 30, no. 3, pp. 409-418, 1982.

[20] D. H. Schaubert, D. R. Wilton, and A. W. Glisson, "A Tetrahedral Modeling Method for Electromagnetic Scattering by Arbitrarily Shaped Inhomogeneous Dielectric Bodies," *IEEE Trans. Antennas Propagat*., vol. 32, no. 1, pp. 77-85, 1984.

[21] D. R. Wilton, S. M. Rao, A. W. Glisson, D. H. Schaubert, O. M. Al-Bundak, and C. M. Butler, "Potential Integrals for Uniform and Linear Source Distributions on Polygonal and Polyhedral Domains," *IEEE Trans. Antennas Propagat*., vol. 32, no. 3, pp. 276-281, 1984.

[22] Y. Saad, *Iterative methods for sparse linear systems*, *Philadelphia: SIAM*, 2nd ed. 2003.

[23] C. A. Balanis, *Advanced Engineering Electromagentics*, John Wiley & Sons, New York, 1989.

[24] R. F. Harrington, *Field Computation by Moment Methods*, New York, Macmillan, 1968.

[25] N. –B. Jin and Y. Rahmat-Samii, "Parallel Particle Swarm Optimization and Finite-Difference Time-Domain (PSO/FDTD) Algorithm for Multi-Band and Wide-Band Patch Antenna Designs," *IEEE Trans. Antennas Propagat*., vol. 53, no. 11, pp. 3459-3468, 2005.

[26] K. Tatsuya, O. Teruo, and F. Ichiro, "Analysis of Microstrip Antennas on a Curved Surface using the Conformal Grids FD-TD Method," *IEEE Trans. Antennas Propagat.*, vol. 42, no. 3, pp. 423-427, 1994.

[27] K. –L. Wong and G. –B. Hsieh, "Curvature Effects on the Radiation Patterns of Cylindrical Microstrip Arrays," *Microwave Opt. Technol. lett*., vol. 18, no. 3, pp. 206-209, 1998.

[28] T. Weiland, M. Timm, and I. Munteanu, "A Practical Guide to 3-D Simulation," *IEEE Microwave Magazine*, vol. 9, no. 6, pp. 62-75, 2008.

[29] Z. A. Maricevic and T. K. Sarkar, "Analysis and Measurements of Arbitrarily Shaped Open Microstrip Structures," *Progress In Electromagnetics Research*, *PIER,* vol. 15, pp. 253-301, 1997.

[30] N. Yuan, T. S. Yeo, X. C. Nie, L. –W. Li, and Y. B. Gan, "Efficient Analysis of Electromagnetic Scattering and Radiation from Patches on Finite, Arbitrarily Curved, Grounded Substrates," *Radio Sci.*, vol. 39, no. 3, pp. RS3003-1- RS3003-13, 2004.

Ke Xiao was born in Hunan, China, in 1979. He received the B.S. and M.S. degrees in college of Electronic Science and Engineering from National Univ. of Defense Tech. in 2003 and 2005, respectively. From 2006, he is working toward the Ph.D degree at the same university, and from 2008 to 2010, he studied in National Univ. of Singapore as a scholar afforded by Chinese Scholarship Council. His research interests include electromagnetic numerical computation, metamaterials and broadband miniature antennas.

Ya Nan Li was born in Anhui, China, in 1983. She is currently working toward the Ph.D. degree at National Univ. of Defense Tech., her research interests include inverse scattering, SAR imaging.

Fei Zhao was born in Shanxi, China, in 1983. He is currently working toward the Ph.D. degree at National Univ. of Defense Tech., his research interests include conformal antennas, microwave circuit system.

Shun Lian Chai was born in Hubei, China, in 1969. Now, he is a professor in National Univ. of Defense Tech., his research interest includes numerical electromagnetic method, fast algorithms, and integrated circuit simulations.

Jun Jie Mao was born in Hunan, China, in 1943. He is a professor in National Univ. of Defense Tech., and a senior member of the Chinese Institute of Electronics (CIE).

Effect of Curvature on the Performance of a Cylindrically-Conformal Cavity-Backed E-patch Antenna

Chad M. Gardner[1], Edward J. Rothwell[1], Leo C. Kempel[1], Jose A. Hejase[1], Raoul O. Ouedraogo[1], and Stephen W. Schneider[2]

[1] Department of Electrical and Computer Engineering
Michigan State University, East Lansing, MI 48824, USA
chadula@gmail.com, rothwell@egr.msu.edu, kempel@egr.msu.edu, hejasejo@msu.edu, ojunior82@gmail.com

[2] Air Force Research Laboratory, Wright Patterson AFB, OH 45433, USA
Stephen.Schneider@wpafb.af.mil

Abstract **─** The behavior of a cavity-backed E-patch antenna placed conformal to a cylindrical conducting surface is explored through simulations and experiment to determine the effects of curvature on antenna performance. It is shown that introducing a cavity backing reduces the bandwidth of an E-patch, but that the curvature of a conformal antenna partly compensates for the loss of performance. It is further shown that the curvature of a conformal antenna strongly affects both the co- and cross-polarization gain patterns.

Index Terms **─** Aircraft antennas, antenna measurements, antenna radiation patterns, conformal antennas, multifrequency antennas.

I. INTRODUCTION

E-patch antennas were introduced in [1] as a novel way to increase the bandwidth of conventional rectangular patch antennas. A typical E-patch is positioned on top of a low-permittivity spacer above a ground plane and fed through a coaxial probe. Use of a low permittivity dielectric (possibly air) produces maximal bandwidth. Since cavity-backed antennas are used in a wide variety of applications [2-4], a variant of this antenna explored here is to position the E-patch at the aperture of a rectangular dielectric-filled cavity as shown in Figure 1. Two parallel slots are cut into the patch in vertical symmetry with respect to the feed point so as to excite Mode 2 of the antenna (as described in [1]). The slot length L_s, slot width W_s, slot placement P_s, and cavity height h are all crucial to controlling the bandwidth of the antenna. The slots of the E-patch antenna allow it to resonate at two frequencies, and the bandwidth is determined primarily by the separation of the frequencies.

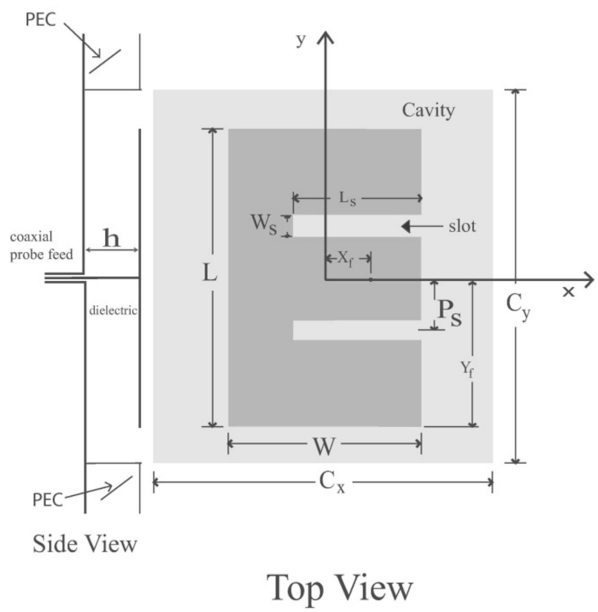

Fig. 1. Geometry of a planar cavity-backed E-patch antenna.

Patch antennas are appealing for aerospace applications because they may be easily conformed to a curved surface, such as an airplane wing or fuselage [5-9]. It is also possible to install a cavity-backed E-patch conformally, but the

Submitted On: Aug. 16, 2011
Accepted On: Nov. 1, 2011

1054-4887 © 2011 ACES

effect of surface curvature on the performance of an E-patch has not yet been investigated. It is important, in particular, to determine whether conformal installation has a deleterious effect on the enhanced bandwidth of the E-patch. In [10], the effect of conforming a rectangular patch antenna to the surface of a cylinder was investigated and the authors found that the bandwidth of the antenna increased and the pattern broadened. They did not, however, include a backing cavity, so it remains to understand how a backing cavity influences the fields and impedance of a conformal E-patch. To explore these effects, a cavity-backed E-patch is placed conformal to the surface of a perfectly conducting cylinder, and the properties of the antenna are examined through simulation as the radius of the cylinder is altered. The characteristics of a typical conformal cavity-backed E-patch are also examined experimentally, by installing a prototype antenna in an aluminum-coated tube.

II. TRADITIONAL AND CAVITY-BACKED E-PATCH ANTENNAS FOR L-BAND OPERATION

To serve as a baseline for comparison with the conformal cavity-backed E-patch, a traditional air-dielectric E-patch antenna was designed to operate with a return loss of at least 10 dB within the L-band frequency range 1200-1600 MHz. This covers the entire range between the L2 (1227.6 MHz) and L1 (1575.42 MHz) GPS operating frequencies. The design equations given in [11] were used as a starting point, and then trial and error was used to obtain the antenna with the dimensions shown in Table 1. The reflection coefficient (negative of the return loss in dB), as computed using the commercial solver Sonnet, is shown in Figure 2. It can be seen that the 10-dB bandwidth of the antenna extends from 1150-1650 MHz and thus meets the desired bandwidth criterion. Note that in the simulations, a ground plane of infinite extent was employed.

An air-filled backing cavity was then added to the E-patch and the dimensions of the antenna and cavity were adjusted in an attempt to produce the same 10-dB bandwidth (1200-1600 MHz) as with the traditional E-patch. Here computations were carried out using an in-house solver based on the finite-element boundary-integral method, again with a ground plane of infinite extent. Unfortunately, a trial-and-error approach was unable to achieve a return loss of 10 dB or greater over this band. So, Taguchi's optimization method [12,13] was implemented to adjust the dimensional parameters to try to meet the bandwidth criterion. The optimal design, with the dimensions shown in Table 2, has the reflection coefficient marked “Rectangular” in Fig. 3. It is seen that even after optimization, the cavity-backed antenna is not able to meet a 10-dB minimum return loss over the entire band 1200-1600 MHz. Operation near the L1 and L2 GPS frequencies is acceptable, but the return loss drops to about 6 dB at frequencies intermediate to these. It is thus concluded that a backing cavity has a somewhat deleterious effect on the wideband performance of an E-patch antenna.

Table 1: Dimensions of a traditional E-patch antenna designed for operation within the band 1200-1600 MHz

Dimension	Value in mm
L	107.1
W	91.2
X_f	5.5
Y_f	53.6
L_s	84.8
W_s	5.6
P_s	11.0
h	11.7

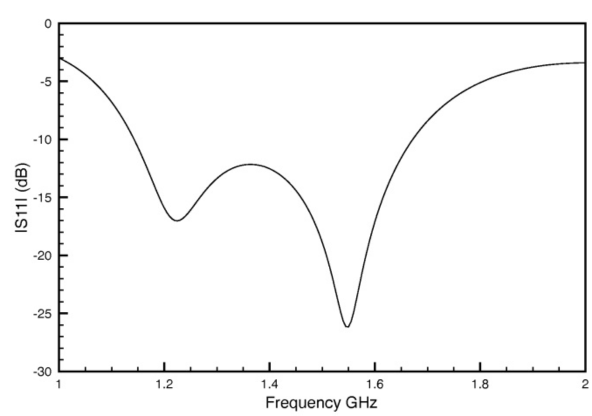

Fig. 2. Reflection coefficient for a traditional E-patch antenna. System impedance is 50Ω.

Table 2: Dimensions of a rectangular cavity-backed E-patch antenna designed for operation within the band 1200-1600 MHz

Dimension	Value in mm
L	96
W	83
X_f	37.5
Y_f	48
L_s	65
W_s	7
P_s	13
h	15.6
C_x	200
C_y	200

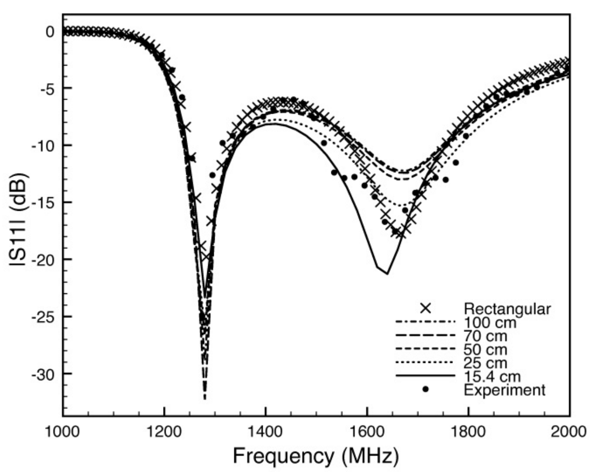

Fig. 3. Reflection coefficient for a cavity-backed E-patch antenna. Cavity is either planar, or conformed to the surface of a cylinder with various radii ρ. System impedance is 50Ω. Radius for the experimental antenna is 15.4 cm.

III. GEOMETRY OF A CYLINDRICALLY-CONFORMAL CAVITY-BACKED E-PATCH ANTENNA

Figure 4 depicts the geometry of a cavity-backed E-patch antenna placed conformal to the surface of a cylinder. In order to analyze how the curvature of the cylinder affects antenna performance, it is useful to start with the planar cavity-backed E-patch as a baseline. The manner in which the dimensions of the planar antenna given in Table 2 are maintained for the conformal E-patch can be seen by comparing Fig. 1 to Fig. 4. Dimensions of the planar antenna measured along y are maintained for the conformal antenna as dimensions measured along z. Dimensions measured along x become the curved distances measured as arc lengths given by $s = \rho\phi$, where ρ is the cylinder radius and ϕ is the angle subtended. Dimensions of the planar antenna measured along z, such as the cavity height h, are specified for the conformal antenna as a radial distance.

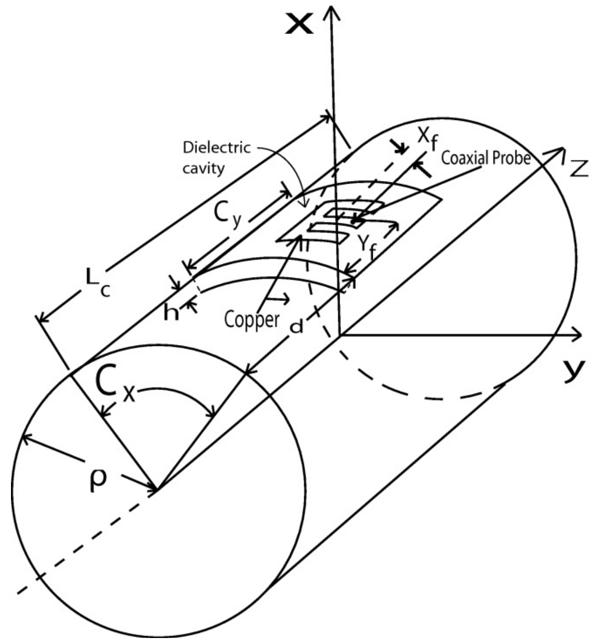

Fig. 4. Geometry of the cavity-backed E-patch antenna conformal to the surface of a cylinder of radius ρ.

IV. EFFECTS OF CURVATURE ON RETURN LOSS

The commercial EM solver HFSS was used to analyze both the planar cavity-backed E-patch antenna shown in Fig. 1 and the cylindrically-conformal cavity-backed E-patch shown in Fig. 4. The reflection coefficients found for various cylinder radii are shown in Fig. 3, referenced to 50Ω, with a cylinder length of $L_c = 100$ cm (except for the 15.4 cm radius case, which has $L_c = 122$ cm to match the experimental antenna). The largest radius of curvature (100 cm) produces a return loss near the second resonance significantly lower than the planar case (12 dB versus 18 dB at 1650 MHz). At the first resonance, the return loss is similar to that of the planar case, and at frequencies in between the resonances the return losses are also nearly the same at about 6 dB. Thus, like the planar cavity-backed antenna, the curved cavity-backed antenna cannot meet the bandwidth criterion. As radius is decreased, however, the return loss at the second resonance increases, as does the return loss between resonances. At a radius of 15.4 cm the return losses at the two resonances are nearly the same (although the frequency of the second resonance has decreased), and the return loss between the resonances has increased to about 8 dB. The effect of a highly curved surface is thus to improve the performance of the antenna between the L2 and L1 frequencies, although the 10 dB bandwidth criterion is still not met. Improved return loss bandwidth is probably due to a reduction in antenna Q produced by the enhanced radiation dampening introduced by the cylinder curvature.

V. EFFECTS OF CURVATURE ON GAIN PATTERNS

Figures 5 and 6 show the co-polarized gain patterns for a cavity-backed E-patch antenna conformal to a cylinder of various radii, simulated at 1300 MHz using HFSS. For cuts taken in the X-Z plane, negative values of θ indicate observations in the $x < 0$ plane, while positive values correspond to the $x > 0$ plane.

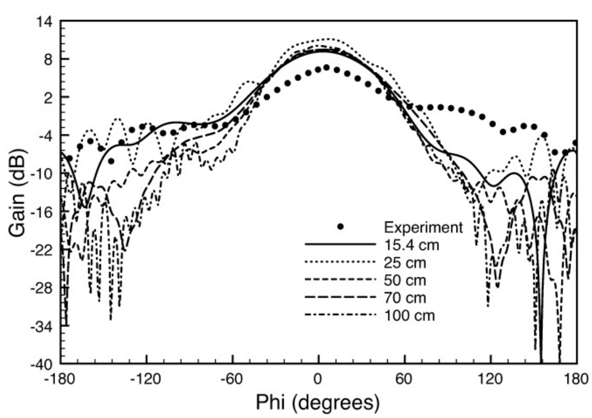

Fig. 5. Co-polarized gain pattern in the X-Y plane of a cylindrically conformal cavity-backed E-patch antenna at $f = 1300$ MHz. Radius of experimental antenna is 15.4 cm.

For cuts in the X-Y plane, curvature has very little effect (1 or 2 dB) on the broadside ($\phi = 0^\circ$) gain. However, as the radius of curvature is decreased, the gain away from broadside is significantly increased at most angles. At a radius of 15.4 cm, the front-to-back ratio (gain at $\phi = 0^\circ$ minus the gain at $\phi = 180^\circ$) is only 14 dB. Similar effects are seen for cuts in the X-Z plane, where the gain away from broadside increases and flattens considerably as the radius of curvature is reduced.

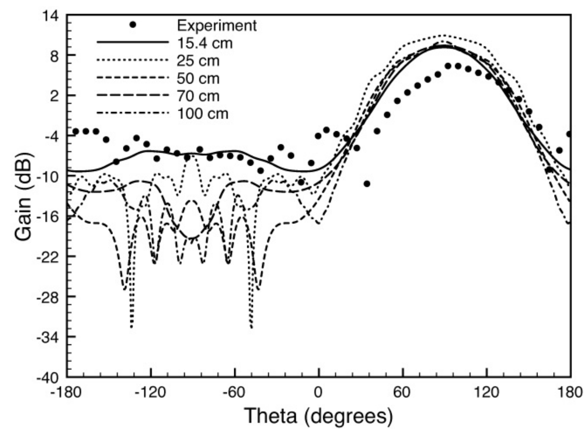

Fig. 6. Co-polarized gain pattern in the X-Z plane of the simulated cylindrically conformal cavity-backed E-patch antenna at $f = 1300$ MHz. Radius of experimental antenna is 15.4 cm.

Similar effects on pattern were described in [2] for a rectangular patch antenna placed conformal to a circular cylinder. With a patch radiating edge length of about 60% of the cylinder radius, similar to the E-patch case of $\rho = 15.4$ cm, a front-to-back ratio of 15 dB was found. Pattern filling away from broadside is probably due to the fact that as the cylinder radius becomes comparable to the patch edge size, the radiating edges of the patch become significantly closer together, reducing the directivity and increasing the side lobes.

Effects of curvature on the cross-polarized gain patterns are more pronounced, but in all cases the cross-polarized gain is significantly below the co-polarized gain. The largest cross-polarized gain was seen in the X-Z plane at broadside, with a value of about -5 dB. In the X-Y plane the cross-polarized gain never rises above -20 dB, regardless of the radius of curvature.

Although not shown here, similar effects of curvature on gain pattern can be observed at the second resonance frequency.

VI. COMPARISON TO EXPERIMENT

To verify the results predicted by simulation, a prototype conformal cavity-backed antenna was constructed using an 122 cm long, 15.4 cm radius tube covered by aluminum foil (see Fig. 7). An aperture was cut into the tube, and a cavity was constructed as shown in Fig. 4 using high-density Styrofoam and copper tape. A copper E-patch was placed in the aperture on top of the Styrofoam and the center conductor of a coaxial feed was passed through the cavity from inside the cylinder and soldered to the patch. All dimensions of the prototype correspond to the values used in the simulations as shown in Table 2.

Fig. 7. Photo of prototype. Radius of cylinder is 15.4 cm.

The reflection coefficient for the prototype antenna measured with a 50Ω system is shown in Fig. 3 and compared with the results for the simulated antenna. The measured return loss is very close to that of the antenna simulated on a 15.4 cm radius cylinder, except near the second resonance where there is some discrepancy, probably due to standing waves in the aperture caused by the copper tape used to attach the cavity to the aluminum tube. In any event, the measured return loss verifies that placing the antenna conformal to the curved surface does not have a deleterious effect on the bandwidth.

The measured co-polarized X-Y and X-Z plane gain patterns of the prototype are shown in Figs. 5 and 6, respectively. Although the measured patterns show slightly less gain at broadside than the simulations (about 3 dB less), they verify that the gain of the strongly-curved antenna is fairly high and quite flat away from broadside, and that the front-to-back ratio is not large (about 12 dB, or slightly less than predicted in the simulations). The cross-polarization patterns could not be measured accurately away from broadside due to the limited dynamic range of the measurement system, but showed trends similar to the simulations near broadside.

VII. CONCLUSION

The effects of curvature on a cylindrically-conformal cavity-backed E-patch antenna are examined experimentally and through simulations. It is shown that it is difficult to achieve the same wideband return loss with a cavity-backed antenna as with a classic planar E-patch. However, when the cavity-backed antenna is conformed to a cylinder, the curvature of the antenna may be used to improve the bandwidth and approach the performance of the traditional E-patch antenna. In contrast, high curvature degrades the patterns of the conformal antenna somewhat, producing gain patterns with a reduced co-polarized front-to-back ratio and significant cross-polarization gain at broadside.

ACKNOWLEDGMENT

This work was supported by the Air Force Research Laboratory under contract FA8650-09-C-1619.

REFERENCES

[1] F. Yang, X.-X. Zhang, and Y. Rahmat-Samii, “Wide-band E-shaped patch antennas for wireless communications,” *IEEE Trans. Antennas Propagat.*, vol. 49, no. 7, pp. 1094-1100, July 2001.

[2] N. Rahman, A. Sharma, M. Asfar, S. Palreddy, R. Cheung, "Dielectric characterization and optimization of wide-band, cavity-backed spiral antennas," *Applied Computational Electromagnetics Society (ACES) Journal*, vol. 26, no. 2, pp. 123 - 130, February 2011.

[3] D. Caratelli, A. Yarovoy, "Design and Full-Wave Analysis of Cavity-Backed Resistively Loaded Circular-End Bow-Tie Antennas for GPR Applications – Part I," *Applied Computational Electromagnetics Society (ACES) Journal*, vol. 25, no. 10, pp. 809 - 817, October 2010.

[4] D. Caratelli, A. Yarovoy, "Design and Full-Wave Analysis of Cavity-Backed Resistively Loaded Circular-End Bow-Tie Antennas for GPR Applications - Part II," *Applied Computational Electromagnetics Society (ACES) Journal*, vol. 25, no. 10, pp. 818 - 829, October 2010.

[5] K. M. Luk, K. F. Lee, and I. S. Dahele, "Analysis of the cylindrical rectangular patch antenna," *IEEE Trans. Antennas Propagat.*, vol. AP-37, no. 2, pp. 143-147, Feb. 1989.

[6] X. Liu, Y. Chen, Y. Jiao, and F. Zhang, "Conformal low-profile E-shaped patch antenna with unequal thickness substrate," *Symposium on Microwave, Antenna, Propagation and EMC Technologies for Wireless Communications*, 16-17 August, Hangzhou, China, pp. 624-627, 2007.

[7] R. T. Jacobs, A. Kost, H. Igarashi, and A. J. Sangster, "Analysis of planar and curved microstrip antennas," *J. Microwaves and Optoelectronics,* vol. 6, no. 1, pp. 96-110, 2007.

[8] M. Redondo Gonzalez, "Analysis of conformal antennas for avionics aplications," Master's Thesis, Chalmers University of Technology, Gothenburg, Sweden, January 2007.

[9] D. H. Werner, R. J. Allard, R. A. Martin, and R. Mittra, "A reciprocity approach for calculating radiation patterns of arbitrarily shaped microstrip antennas mounted on circularly cylindrical platforms," *IEEE Trans. Antennas Propagat.*, vol. 51, no. 4, pp. 730-738, April 2003.

[10] J. S. Dahele, R. J. Mitchell, K. M. Luk, and K. F. Lee, "Effect of curvature on characteristics of rectangular patch antenna," *Electronics Letters*, vol. 23, no. 14, pp. 748-749, July 2, 1987.

[11] A. Bzeih, S. A. Chahine, K. Y. Kabalan, A. El-Hajj, A. Chehab, "Empirical formulation and design of a broadband enhanced E-patch antenna," *National Radio Science Conference*, Cairo, Egypt, pp. 1-9, March 13-15, 2007.

[12] W.-C. Weng, F. Yang, V. Demir, and A. Z. Elsherbeni, "Linear antenna array synthesis using Taguchi's method: a novel optimization technique in electromagnetics," *IEEE Trans. Antennas Prpagat.*, vol. 55, no. 3, pp. 723-730, March 2007.

[13] Gardner, "A Conformal Taguchi Optimized E-patch Antenna," M.S. Thesis, Michigan State University, East Lansing, MI, Dec. 2010.

Chad M. Gardner is originally from Elkton, MI. He received the B.S. degree in Electrical Engineering in 2007 and the M.S. degree in Electrical Engineering in 2010, both from Michigan State University. Before completing his Masters, he worked for Naval Air Systems Command (NAVAIR) in Cherry Point, NC, where he worked on the Av-8B, H-46, H-53, and H-60 aircraft. He currently is working for Space and Naval Warfare Systems Command (SPAWAR) in Charleston SC, where he is involved with critical protection for national assets. His interests include acoustics, antennas, and microwave measurement techniques.

Edward J. Rothwell was born in Grand Rapids, MI. He received the B.S. degree in Electrical Engineering from Michigan Technological University, Houghton, in 1979, the M.S. degree in Electrical Engineering and the degree of Electrical Engineer from Stanford University, Stanford, CA, in 1980 and 1982, and the Ph.D. degree in Electrical Engineering from Michigan State University, East Lansing, MI, in 1985, where he held the Dean's Distinguished Fellowship.

He worked for Raytheon Co., Microwave and Power Tube Division, Waltham, MA, from 1979-1982 on low power traveling wave tubes, and for MIT Lincoln Laboratory, Lexington, MA, in 1985. He has been at Michigan State University from 1985-1990 as an assistant professor of electrical engineering, from 1990-1998 as an associate professor, and from 1998 as professor. He received the John D. Withrow award for teaching excellence from the College of Engineering at Michigan State University in 1991, 1996 and 2006, the Withrow Distinguished Scholar Award in 2007, and the MSU Alumni Club of Mid-Michigan Quality in Undergraduate Teaching Award in 2003. He was a joint recipient of the Best Technical Paper Award at the 2003 Antenna Measurement Techniques Association Symposium, and in 2005 he received the Southeast Michigan IEEE Section Award for Most Outstanding Professional.

Dr. Rothwell is a Fellow of the IEEE, and is a member of Phi Kappa Phi, Sigma Xi, and Commission B of URSI. He is co-author of the book *Electromagnetics* (Boca Raton, FL: CRC Press, 2001; 2nd edition 2008).

Leo C. Kempel was born in Akron, OH. He earned his B.S.E.E. at the University of Cincinnati in 1989 as well as the M.S.E.E. and Ph.D. degrees at the University of Michigan in 1990 and 1994, respectively.

After a brief Post-Doctoral appointment at the University of Michigan, Dr. Kempel joined Mission Research Corporation in 1994 as a Senior Research Engineer. He led several projects involving the design of conformal antennas, computational electromagnetics, scattering analysis, and high power/ultrawideband microwaves. He joined Michigan State University in 1998 as an Assistant Professor. He is currently a Professor of Electrical and Computer Engineering and Associate Dean for Research for the College of Engineering at Michigan State University. His research interests are in applied electromagnetics including theoretical, computational, and experimental methods. He is the co-author of *Finite Element Method for Electromagnetics with Application to Antennas, Microwave Circuits, and Scattering*, published by IEEE Press.

Professor Kempel was awarded a CAREER award by the National Science Foundation and the Teacher-Scholar award by Michigan State University in 2002. He also received the MSU College of Engineering's Withrow Distinguished Scholar (Junior Faculty) Award in 2001. He was elected as a Fellow of the Applied Computational Electromagnetics Society (ACES) and as a Fellow of the Institute of Electrical and Electronics Engineers in 2009, and was an elected member of the ACES Board of Directors for 2003-2006 and served as Secretary to the board for that period. He is also a Senior Member of the Antenna Measurement Techniques Association (AMTA).

Jose A. Hejase received his B.S. in Electrical Engineering (cum laude) from Oakland University, Rochester Hills, MI, USA in 2006 and his M.S. in Electrical and Computer Engineering from Michigan State University, East Lansing, MI, USA in 2009 and is currently pursuing his Ph.D. in Electrical and Computer Engineering at Michigan State University.

Currently, he is a member of the Electromagnetics Research Group at Michigan State University and specifically associated with the Terahertz Systems Laboratory. His research interests lie in applied electromagnetics with focus towards electromagnetic sensors design, material characterization measurement techniques and extraction algorithms, and electromagnetic nondestructive evaluation.

Mr. Hejase is a student member of IEEE, National Electrical Engineering Honor Society (Eta Kappa Nu) and The Golden Key International Honor Society.

Raoul O. Ouedraogo was born in Ouagadougou, Burkina Faso, in 1982. He received the B.S. degree from Southern Illinois University, Carbondale, IL, in 2006, the M.S. degree from Michigan State University, East Lansing, in 2008, and is currently working toward the Ph.D. degree at Michigan State University, all in Electrical Engineering. His current research interests include metamaterials, small antennas, self-structuring devices, electromagnetic radiation, and scattering.

Stephen W. Schneider received his B.S.E.E. from Arizona State University (1985), and his M.S. (1988) and Ph.D. (1992) in Electrical Engineering from the Ohio State University. He has over 25 years of experience in the area of applied electromagnetics. From 1985 to 1992, Dr. Schneider was employed at the Ohio State University ElectroScience Laboratory where he was involved in the analysis, design and measurement of periodic surfaces for frequency selective surfaces and phased arrays. Since 1992, he has been with the U.S. Air Force Research Laboratory (AFRL), Wright-Patterson AFB, Ohio, where he currently is a member of the scientific and professional cadre of senior executives, serving as a the Senior Scientist for the AFRL Sensors Directorate. Dr. Schneider is an internationally recognized scientific expert, who provides authoritarian counsel and advice to AFRL management and the professional staff as well as to other government organizations.

Dr. Schneider is a Fellow of AFRL and IEEE, and a Senior Member of the Antenna Measurement Techniques Association (AMTA).

Optimized Design of Cylindrical Corner Reflectors for Applications on TV Broadband Antennas

J. A. Romo, I. F. Anitzine, and J. Garate

Department of Electronics and Telecommunications
University of the Basque Country
Alameda Urquijo s/n, Bilbao, Spain
juanantonio.romo@ehu.es; ignacio.anitzine@ehu.es; jgarate001@ehu.es

Abstract ─ The increasing of digital TV channels throughout the UHF band leads to use antennas with greater directive gain and improved response in higher bandwidth. For this purpose, in this paper an optimized design for a cylindrical corner reflector is presented. A comparative study between the radiation patterns in the UHF band for different commonly used reflectors is therefore carried out. Based on this study, a modified Yagi-Uda antenna with a cylindrical corner reflector has been suggested and implemented.

Index Terms ─ Antennas, TV Broadcasting Antennas, Reflector Antennas, Yagi-Uda Antennas.

I. INTRODUCTION

Antennas derived from the Yagi-Uda configuration are extensively used as general-purpose antennas in the UHF band. These types of antennas are composed by simple elements: driven element, reflector, and director element. [1]

Bandwidth is basically delimited by the reflector and feeder system. Director element is intended to increase the directivity of the antenna in the forward direction.

The reflector is a parasitic element that re-radiates impinged radiation, either from or going to the active feeder, into free space. Thus, it has a close relationship with the gain of the antenna.

For these purposes, reflectors are usually formed by equidistant wires, which are generally longer than the feeder element. Reflectors more commonly used in Yagi antennas are parabolic and corner reflectors.

The use of parabolic reflectors was introduced by Wheeler, presenting a wide study of the radiation characteristics, depending on the physical dimension. [2]

There are some variations of the parabolic reflectors. The parabolic cylinder is the most used of them in the UHF band. It provides a narrow beamwidth in the plane of the axis of reflector. The essential parameters in the design of this reflector are: diameter, D, and focal distance, f. The rest of parameters can be determined from them. When D > 4f a major efficiency is obtained in practice. [3-4]

Corner reflectors were introduced by Kraus [5]. They are formed by planar reflective sheets joined together forming an angle, α. Radiation pattern is a function of geometric dimensions: distance between vertex and feeder, s, and length, l, and height, h, of planar surface.

Investigations and improvements in the radiation patterns have been widely studied since the introduction of corner reflectors. [6,7,8]

A more complex reflecting structure is the Cylindrical-corner mix. It is composed by three conductive surfaces: two planes forming a corner reflector and the third one forming a cylindrical section. [9]

Design of this reflector is a more complex task than in the case of the conventional one. Multiple variables can influence an optimized design: radius of cylinder, aperture angle, position of the cylinder with regard to the corner panels and position of the feeder. In recent years, some studies on this topic have been carried out. Some of them have analyzed different feeding

Submitted On: July 19, 2011
Accepted On: Oct. 15, 2011

configurations [10] and others dealt with the performance of the reflector. [11]

With the aim of improving the performance of the Yagi-Uda antenna regarding the radiation bandwidth in TV applications, from 470 to 862 MHz, by means of the use of cylindrical-corner reflector, we have carried out an optimization study of the parameters of this kind of reflector. The results have been compared with the performance obtained with the rest of the most commonly used reflectors. From these facts, an improved implementation of the Yagi-Uda antenna based on the cylindrical-corner reflector is presented.

Programs based on the moment method, MoM, have been used in both processes, in the prototype design, and in the performance simulations. This well known method determines the element currents through numerical techniques. [12-13]

II. CONSIDERATIONS ABOUT FEEDER

In order to carry out the methodology on the comparative analysis and optimization for the reflector, a common feeder for all prototypes has been selected. Some different feeders have been studied with regard to directivity and radiation pattern: dipole, folded dipole, and different more complex configurations.

According to previous investigations, the feeder showed in Figure 1 has been chosen. The most important features of this feeder are summarized in the next paragraph: it is constructed by planar sheets of width equals to 0.5mm. It is connected through a balun 1:4. Length varies between approximately 0.54λ at the lowest frequency and 0.99 λ at the highest frequency of the bandwidth. Directivity gain is greater than 2dB with regard to simple elements.

The radiation pattern is symmetric as shown in Figure 2. Taking into account the whole involved variables, final prototype is shown in Figure 3 and its characteristics are: summarized in the next paragraph. Aperture angle of corner structure is 90º, elements uniform spacing of 5 cm, diameter of the cylindrical surface of 16 cm, distance between center of cylindrical surface and corner vertex is 5.5 cm, and gap between feeder and reflector is 6 cm.

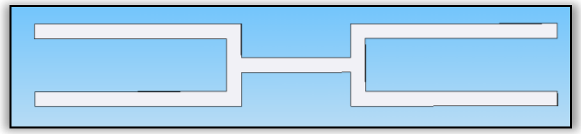

Fig. 1. Drawing of used feeder.

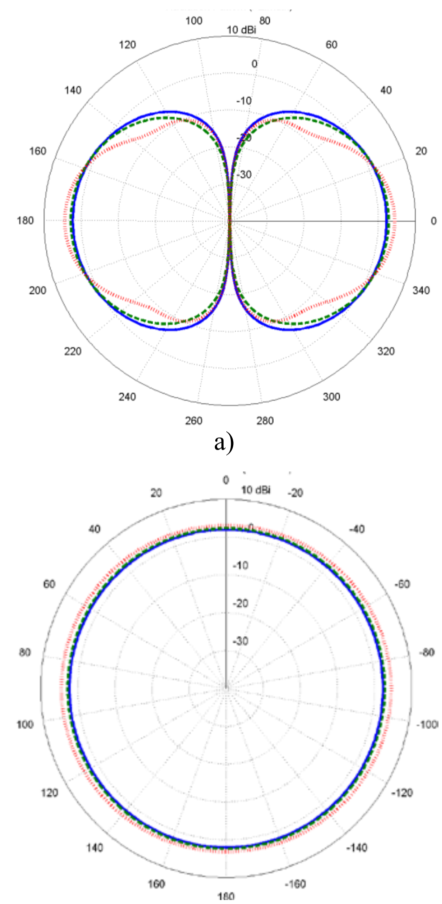

a)

b)

— 450 MHz. --- 600 MHz. ••• 900MHz.

Fig. 2. Radiation pattern of feeder: a) azimuthal plane, b) zenithal plane.

III. FORMATTING OF EQUATION, FIGURE, AND REFERENCE

The used methodology of optimization is founded on the steepest descent algorithm. It is based on a weighted function of diverse variables: gain, bandwidth, front to back ratio, VSWR, and impedance. The algorithm is carried out to determine the optimum position of every element of the antenna, mainly intersection angle and position, and dimensions of cylindrical surface, during the design process, as well as in successive improvement processes. Tables 1 and 2 show the comparative most significant results of simulation process in terms of gain for different frequencies.

Table 1: Gain of cylindrical corner reflector prototype for different configurations

Configurations		Gain (dB) for different frequencies (MHz)				
Angle	**Diameter (cm)**	**470**	**550**	**650**	**750**	**862**
90º	13	9.27	9.8	10.89	12.28	13.14
	19	9.07	9.41	10.16	10.96	11.07
120º	13	9.9	9.91	9.84	9.68	8.88
	19	8.97	8.63	7.51	5.84	6.74

Table 2: Gain of cylindrical corner reflector prototype for different configurations

Radii (cm)	Gain (dB) for different frequencies (MHz)				
	470MHz	**550MHz**	**650MHz**	**750MHz**	**860MHz**
16	9.14	9.59	10.54	11.65	12.21
13	9.27	9.8	10.89	12.28	13.14
9	9.12	9.7	10.86	12.31	13.35
6	8.99	9.58	10.73	12.3	13.32

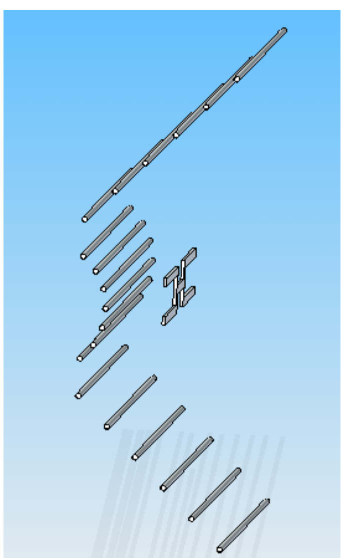

Fig. 3. Picture of prototype of cylindrical-corner reflector and feeder.

IV. DESIGN OF CORNER AND PARABOLIC CYLINDRICAL REFLECTORS

A comparative study between radiation characteristics of cylindrical corner reflector and radiation characteristics of corner of 90º, corner of 120º, and parabolic cylindrical reflectors have been made. In order to carry out a reliable comparative, every reflector has been designed and positioned in an optimum way, in relation to the best possible behavior of gain and directivity in each reflector. The process of optimization in every case is similar to the one explained in the previous paragraph. The obtained results are summarized in the following paragraphs.

A. Corner reflectors

Two corner reflectors, with intersection angles of 90º and 120º respectively, have been analyzed. Gain has been simulated with varying the following geometric parameters: dimensions of elements, inter-element spacing, distance between feeder and vertex, s, and length.

The minimal separation of “s” is determined by the impedance of the system and the maximal value is defined by the antenna directivity and by the appearance of side lobes. In Table 3, the main parameters of the selected corner reflectors are shown.

Table 3: Parameters of corner reflectors

Parameter	90º Corner reflector	120º Corner reflector
Diameter of elements	0.6 mm	
Inter-element spacing	No homogeneous, increasing from vertex. From 0.08λ to 0.18λ at central frequency of UHF band.	
Distance between feeder and corner vertex, s	18.5 cm	14.5 cm
Distance between vertex and last element	1.74s	2.15s
Length of elements, l	57 cm	

Variations of gain of 120º corner reflector versus the frequency of the UHF band for different values of “s”, are shown in Table 4.

Table 4: Gain of corner reflector with intersection angle of 120º

s (cm)	Gain in dB for frequencies in MHz				
	470MHz	550MHz	650MHz	750MHz	860MHz
14.5	9.14	9.59	10.54	11.65	12.21
16.5	9.27	9.8	10.89	12.28	13.14
18.5	9.12	9.7	10.86	12.31	13.35

B. Parabolic cylindrical reflector

The parameters which define the radiation response of the parabolic cylindrical reflector are: dimensions of elements, diameter of cylinder, D, inter-element spacing, and focal distance, f. Tables 5 and 6 show directive gain as function of frequency for different focal distances.

Table 5: Directive gain of parabolic cylindrical reflector versus frequency for several focal distances

f(cm)	Gain in dB for different focal distances				
	470MHz	550MHz	650MHz	750MHz	860MHz
18	7.2	7.28	7.37	6.03	2.01
14	7.26	7.55	8.04	8.83	7.93
12	7.2	7.54	8.12	8.7	8.87

Table 6: Directive gain versus frequency for focal distance of 12 cm

f/D (cm)	Gain in dB for different f/D values				
	470MHz	550MHz	650MHz	750MHz	860MHz
0.25	8.89	9.46	10.39	11.63	12.02
0.3	8.48	8.98	9.81	11.05	11.22
0.4	7.86	8.29	9	9.86	10.1
0.53	7.2	7.54	8.12	9.07	8.87

In Table 7, the most significant characteristics of parabolic cylindrical reflector prototype are shown.

Table 7: Parameters of parabolic cylindrical reflector prototype

Parameter	Parabolic Cylindrical Reflector
Diameter of elements	0.6 mm
Focal distance, f	12 cm: From 0.18λ at lowest frequencies to 0.34λ at highest frequencies of working bandwidth
f/D	0,25

V. COMPARATIVE STUDY OF THE REFLECTORS

A comparative study of the directive gain and radiation pattern characteristics in UHF band for four different reflectors, corner of 90º and 120º, parabolic cylindrical and cylindrical corner, is implemented. The used prototypes for this comparative have been designed in accordance with the criteria exposed in previous paragraphs. Figure 4 plots the directive gain as a function of the frequency in range of the UHF band for TV applications.

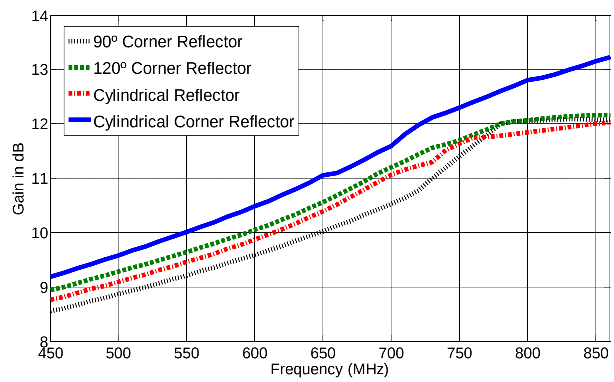

Fig. 4. Directive gain for different prototypes.

For low frequencies, all the reflectors have comparable responses. Nevertheless for higher frequencies, the cylindrical corner reflector has better gain, enhancing the antenna response in the upper frequencies of the UHF band.

Radiation patterns for frequencies of 750 and 850 MHz are plotted in Figures 5 and 6. Where the half-power beamwidth decreases for high frequencies of the band and the side lobes have been improved for cylindrical corner reflector in relation with the other reflectors.

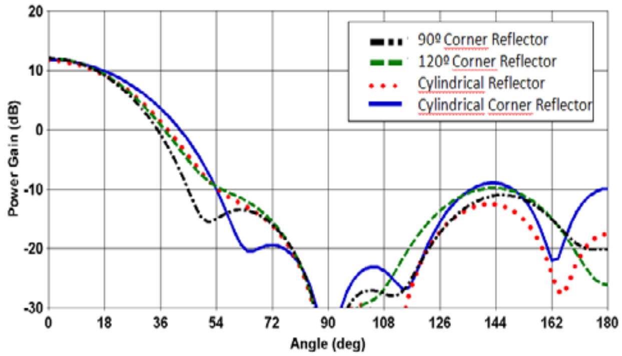

Fig. 5. Radiation pattern for 750MHz.

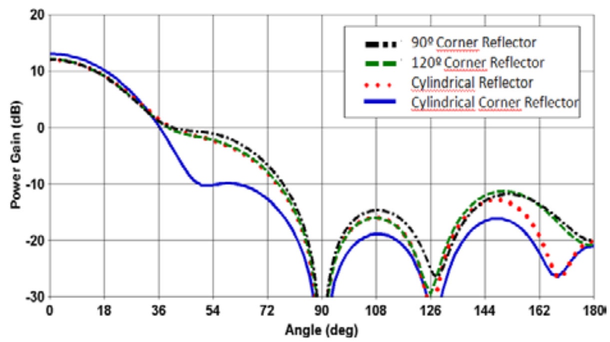

Fig. 6. Radiation pattern for 850MHz.

The directivity is improved in the case of cylindrical corner in relation with the rest of reflectors. This conclusion can be also deduced from Figures 7 and 8. In these figures, half-power beamwidth is represented for the azimuthal and zenithal plane, respectively.

As it can be observed from these figures, cylinder corner reflector presents the best response in all radiation characteristics.

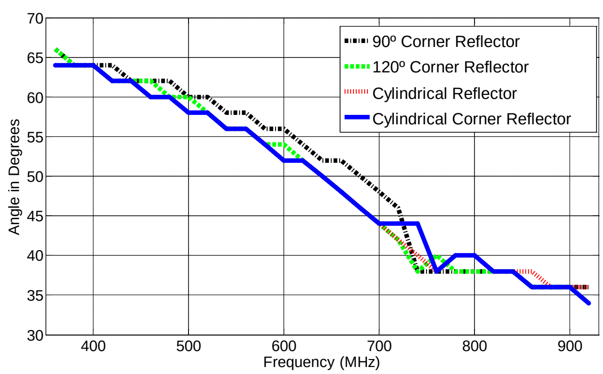

Fig. 7. Half-power beamwidth for the azimuthal plane.

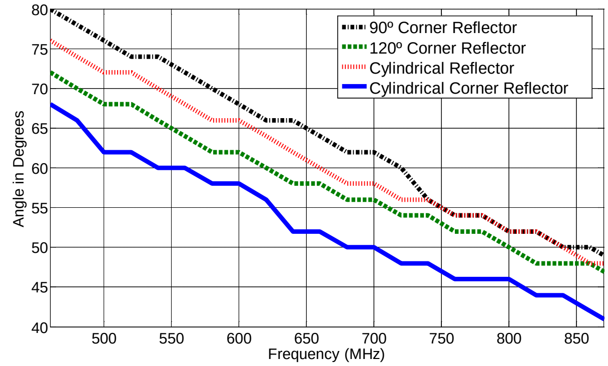

Fig. 8. Half-power beamwidth for the zenithal plane.

VI. IMPLEMENTATION OF YAGI-UDA BROADBAND ANTENNA

Based on the previous design of feeder and cylindrical corner reflector, an implementation of a modified Yagi-Uda antenna is carried out. To control the impedance of the antennas in the complete bandwidth, antenna design have been optimized with passive elements. A rhombic structure with twelve pairs of director elements of 12.2 cm, has been implemented. The distance between elements for each couple is 2.4 cm. See Figure 9.

Fig. 9. Picture of optimized antenna

Directive gain and voltage standing wave ratio (VSWR) as a function of frequency in the UHF band are shown in Figures 10 and 11, respectively for the optimized antenna.

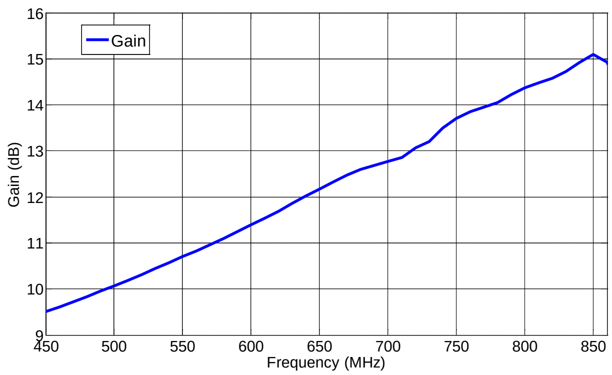

Fig. 10. Obtained directive gain for the antenna.

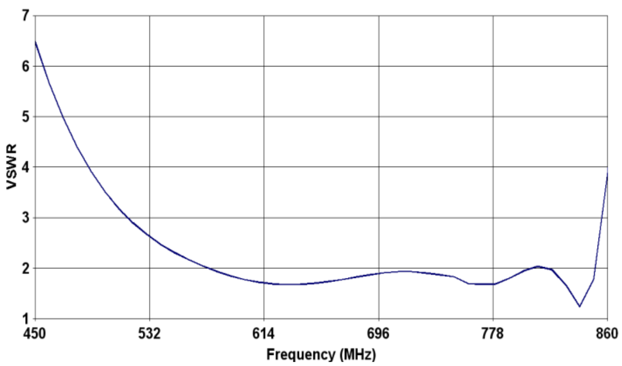

Fig. 11. Obtained VSWR for the antenna.

These figures show how the directivity gain is nearly 15dB for upper frequencies, and greater than 9.5 dB for lower frequencies. The values of VSWR lead to bandwidth of nearly one octave.

Radiation patterns for different frequencies and for azimuthal and zenithal planes are plotted in Figures 12 and 13.

In order to evaluate the performance of the designed antenna, these previous characteristics have been compared with two widely known digital TV antennas. They are formed by similar feeders and 120º corner reflectors. The first antenna is a conventional Yagi-Uda with 14 director elements. The second antenna has the same passive elements with a rhombic structure. A comparative graphic of VSWR and radiation pattern for horizontal and vertical plane are respectively shown in Figures 14, 15, and 16.

From the measured and calculated results it can be seen that the side lobe level of the designed antenna is better than the other kinds of compared antennas.

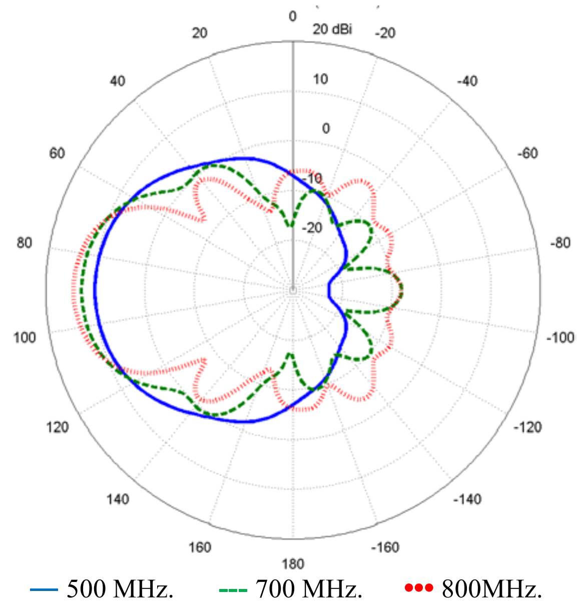

Fig. 12. Radiation pattern for optimized antenna in zenithal plane.

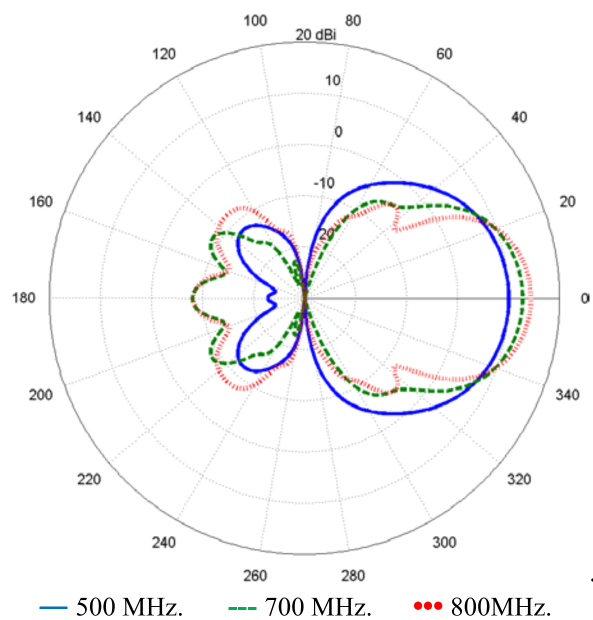

Fig. 13. Radiation pattern for optimized antenna in azimuthal plane.

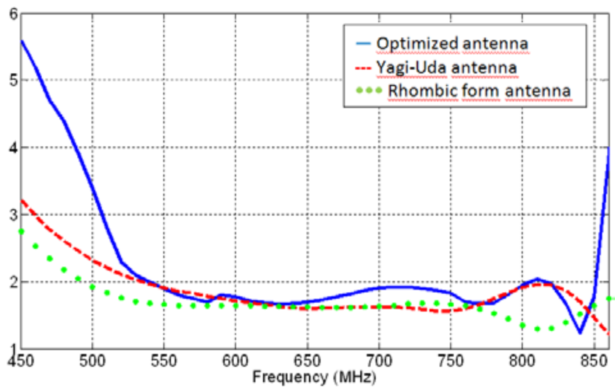

Fig. 14. VSWR.

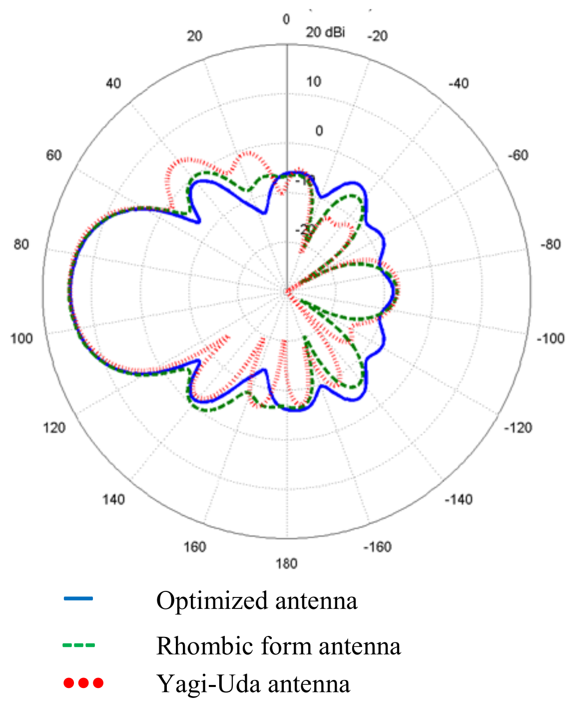

Fig. 15. Radiation pattern in zenithal plane.

VII. CONCLUSION

The design of cylindrical corner reflector has been optimized taking into account the bandwidth response for the application on broadband antennas in UHF band. Comparison with the three most used reflectors in the market, corner of 90º and 120º and parabolic cylindrical reflectors, has been made. The results show a significant enhanced directive gain in the UHF bandwidth. This cylindrical corner reflector design has been used in an implementation of broadband Yagi-Uda antenna.

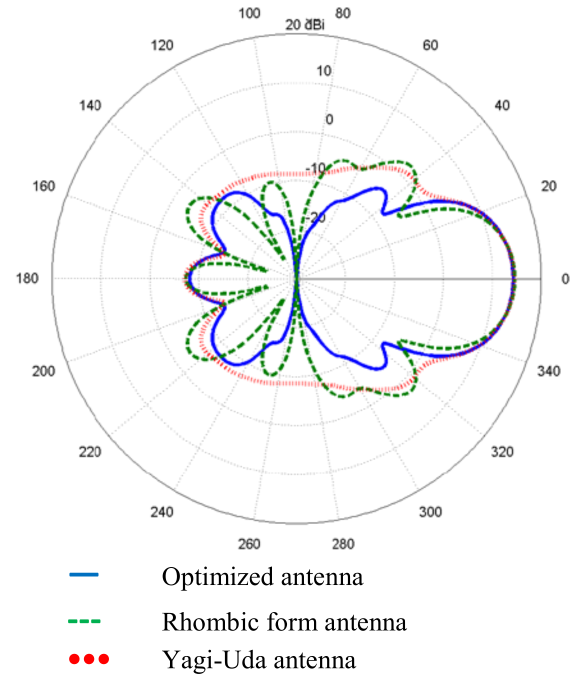

Fig. 16. Radiation pattern in azimuthal plane.

REFERENCES

[1] C. A. Balanis, *Antenna Theory: Analysis and Design*, Third edition, John Wiley & Sons, Inc., Hoboken, New Jersey, 2005.

[2] A. Wheeler Nagy, "An Experimental Study of Parasitic Wire Reflectors on 2.5 Meters," *Proceedings of the Institute of Radio Engineers*, vol. 24, no. 2, February 1936.

[3] Z. M. Xie and R. X. Zhang. "Gain Factor of Horn Array Feed Offset Parabolic Cylindrical Reflector Antenna for Spatial Power Combining," *Microwave and Optical Technology Letters*, vol. 52, no. 8, August 2010.

[4] M. Fazaelifar, "Design, Fabrication and Test of Parabolic Cylinder Reflector and Horn for Increasing the Gain of Vlasov Antenna," *Progress in Electromagnetics Research Letters*, vol. 4, pp. 191-203, 2008.

[5] J. D. Kraus, *The Corner Reflector Antenna*, ffg*Proceedings of the I.R.E*, November 1940.

[6] A. C. Wilson and H. V. Cottony. "Radiation Patterns of Finite-Size Corner-Reflector Antennas," *IRE Transactions on Antennas and Propagation*, March 1960.

[7] G. A. Thiele, "Analysis of Yagi-Uda-type antennas," *IEEE Transactions on Antennas and Propagation*, vol. AP-17, no. 1, January 1969.

[8] Y. Ohba, "On the Radiation Pattern of a Corner Reflector Finite in Width," *IEEE Transactions on Antennas and Propagation*, August 1962.

[9] H. M. Elkamchouchi, "Cylindrical and Three-Dimensional Corner Reflector Antennas," *IEEE Transactions on Antennas and Propagation*, vol. AP-31, no. 3, May 1983.

[10] M. K. Abdelazeez, "Cylindrical Corner Reflector Antenna with Different Feeding Configurations," *IEEE Antennas and Propagation Society International Symposium*, vol. AP 12-9, June 1987.

[11] S. Al Hossain, B. Sharif, and G. Chester, "Improved Corner Reflector Antenna Performance by using Cylindrical Reflectors," *Computation in Electromagnetics*, April 2002.

[12] T. Milligan. *Modern Antenna Design,* Wiley-IEEE Press, pp. 42 -101, 2005.

[13] Y. Zhang, N. K. Nikolova, and M. H. Bakr, "Input Impedance Sensitivity Analysis of Patch Antenna with Discrete Perturbations on Method-of-Moment Grids," *Applied Computational Electromagnetic Society (ACES) Journal*, vol. 25, no. 10, pp. 867-876, October 2010.

Juan Antonio Romo Argota was born in 1958. He has 25 years of experience in diverse areas of telecommunications at manufacturing equipments companies as well as at network operators. Dr. Romo joined the Department of Electronics and Telecommunications of the University of the Basque Country in 1991. He has been coauthor of several research works, papers and conference presentations involved with radio systems planning, antennas, and propagation.

Ignacio Fernández Anitzine joined the Dpt. of Electronics and Telecommunications of the University of the Basque Country in 1988. He has been teaching general telecommunication subjects and antennas and propagation related topics for more than 20 years. His research interests include extensive list of projects and papers in journals and conference presentations in the field of Antennas and propagation.

A New Left-Handed Metamaterial Structure Based on Split-Triangle Resonators (STRs)

Michel A. Abaga Abessolo, N. Aknin, and A. El Moussaoui

Information and Telecommunication Systems Laboratory (LaSIT)
Faculty of Sciences, Abdelmalek Essaadi University, Tetuan, Morocco
Michelabaga1@yahoo.fr, aknin_noura@yahoo.fr, elmoussaoui@uae.ma

Abstract **─** In this paper, small compact split triangle-resonators (STRs) with left-handed metamaterial (LHM) properties is proposed. The parameters of this new resonator are found by using the transfer matrix method and Nicholson-Ross-Weir method. Our results indicate that this structure could be used to realize the refractive index medium. Using the x-direction of the electromagnetic propagation wave, a simultaneous negative permeability and permittivity is obtained. The origin of the negative refractive index is a resonance due to the internal inductance and capacitance of the structure. In addition to simultaneous permittivity and permeability, the copper resonator has the advantage of being positioned on only one side of the FR4 substrate.

Index Terms **─** Metamaterials, split triangle resonators (STRs).

I. INTRODUCTION

The development of artificial materials (metamaterials) with negative refraction index or left-handed materials (LHM) has been a subject of growing interest in recent years. Apart from its exotic electrodynamics properties (such as the reversal of Snell's law, Doppler Effect and Cherenkov radiation), key to this interest is the potential applicability of these metamaterials to the fabrication of RF and microwave components based on left handedness. Due to negative values of effective permittivity and permeability, LHM are negative refractive index (NRI) media with antiparallel phase and group velocities. Namely, the wavevector k forms a left handed triplet with the vectors E and H (the electric and magnetic field intensity) and the wave fronts for propagating EM waves travel towards the source, i.e. opposite to the direction of energy flow [1, 2].

The renewed interest in the subject is due to the rediscovery by Pendry [10] of an old idea by Veselago [11] that materials with simultaneously negative permittivity and permeability can be regarded as negative refractive index materials. Then, a left-handed metamaterial was first implemented in a two dimensional periodic array of split ring resonators and long wire strips by Smith [8].

Recently, there has been growing interest in both the theoretical and experimental study of metamaterials. Many properties and potential applications of left-handed metamaterials (LHM) have been explored and analyzed theoretically. It has been proposed that LHM could be used to build a perfect lens with sub-wavelength resolution [3], and studies have been done on backward waves propagation [4-5], waveguides [21-26], antennas [22, 23, 24] Cerenkov radiation [6], and resonators [7]. The logical approach was to excite the split ring resonators and wire strips in order to force the structure to behave like magnetic and electric dipoles, respectively [9]. Since then, there have been large numbers of experimental investigations on the observation of this phenomenon. SRR/wire-type LHM opens a new field of electromagnetic response with matter. However, there are still some drawbacks such as high losses and limited bandwidth and anisotropic property preventing its further development. These issues prompted researchers to explore new designs such as the Omega pattern [12-13-14], S-Type [27], fishnet [15], and so on.

Submitted On: July 3, 2011
Accepted On: Oct. 21, 2011

1054-4887 © 2011 ACES

In this paper, we present a new LHM resonator with simultaneous negative permittivity and permeability which can be used for conception of microwave antennas and filters design. The structure is composed by two coupled split triangle resonators (STRs) printed on only one side of the FR4 substrate. Therefore, it doesn't need other elements on the opposite side unlike most resonators proposed to date. We study the unit cell of the proposed resonator using two different approaches based on S-parameters that are the standard retrieval method and the Nicholson-Ross-Weir (NRW) approach.

The paper is organized as follows. In Section 2, the design for the constitutive elements of the LHM screen is described. In Section 3, we present the description of the two methods (retrieval and NRW) used. In Section 4, compared results are presented for x direction of propagation. Finally, in Section 5, conclusions are summarized.

II. RESONATOR DESIGN

The STR is formed by two coupled conducting triangles printed on a dielectric slab. Assuming a particle size much smaller than the free space wavelength, the STR's essentially behaves as a quasistatic R*LC* circuit fed by the external magnetic flux linked by the particle.

Figure 1a shows the cubic unit cell of the proposed structure, composed by a 0.5 mm thick substrate of FR4 ($\varepsilon_r = 4.4$, loss tangent of 0.02) and a copper STR positioned on the top side of the substrate. The cubic cell dimension is a=7mm. Figure 1b presents the planar view of the top side of the unit.

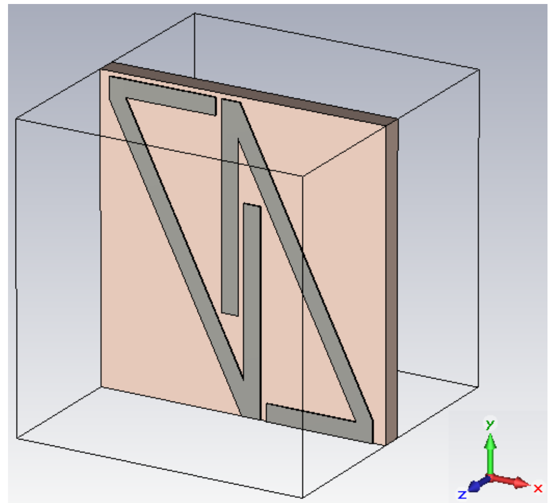

(a)

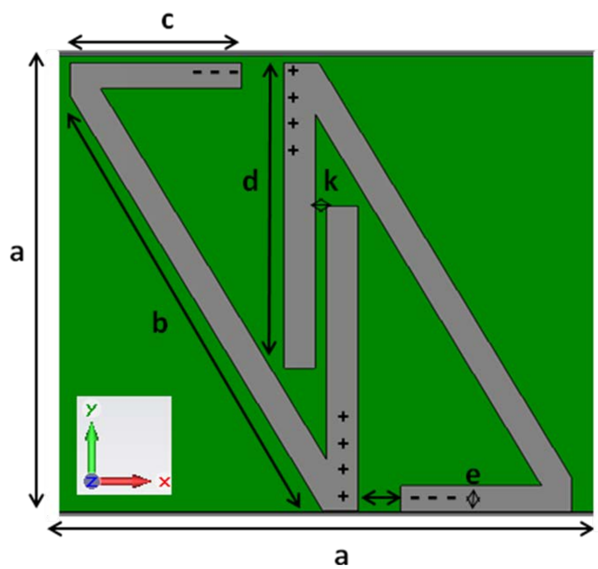

(b)

Fig. 1. Split triangle resonators (STRs): (a) perspective view of the unit cell, (b) planar view of the unit cell, a=7mm; b=7.89mm; c=2.4mm; d=4.3mm; e=0.4mm; P=0.2mm; k=0.2mm.

III. NUMERICAL METHODS DESCRIPTIONS

S-parameters were determined via full-wave simulations. Effective medium parameters (ε, μ) were determined using two methods: the inversion of *S* parameters for the experimental characterization of unknown materials presented by the Nicholson-Ross-Weir approach [16-17] and the standard transfer matrix method [18-19].

A: Standard retrieval method

Assuming a homogeneous medium, knowing the refractive index *n* and wave impedance *z* allows us to find μ and ε. The transfer matrix can be defined from:

$$F' = TF, \tag{1}$$

$$\text{with: } F = \begin{pmatrix} E \\ H_{red} \end{pmatrix}. \tag{2}$$

E and H_{red} are the complex electric and magnetic field amplitudes. Here, the magnetic field assumed throughout is a reduced magnetic field [28] having the normalization $H_{red} = (+i\omega\mu_0 H)$. The transfer matrix for a homogeneous 1D slab has the analytic form

$$\text{And: } T = \begin{pmatrix} \cos(nkd) & -\frac{z}{k}\sin(nkd) \\ \frac{k}{z}\sin(nkd) & \cos(nkd) \end{pmatrix}. \tag{3}$$

The elements of the S matrix can be found from the elements of the T matrix [20].

For a case of homogeneous material, such as the parallelepiped-shape proposed, T11=T22=Ts and det(**T**)=1. We obtain a symmetric S matrix and finally analytic expressions on index and impedance given by:

$$n = \frac{1}{kd}\cos^{-1}\left[\frac{1}{2S_{21}}\left(1 - S_{11}^2 + S_{21}^2\right)\right], \tag{4}$$

$$Z = \sqrt{\frac{(1+S_{11})^2 - S_{21}^2}{(1-S_{11})^2 - S_{21}^2}}, \tag{5}$$

with:

$$\varepsilon = n/z, \tag{6}$$
$$\mu = nz. \tag{7}$$

B: Nicholson-Ross-Weir (NRW) approach

The Nicolson-Ross-Weir (NRW) equations enable the calculation of the complex permeability and permittivity of an unknown material sample entirely filling the cross-section of a reflectionless airline from the measured S-parameters. The relation between measured S-parameters and material properties is derived by considering the multiple reflections of a unit amplitude wave incident upon the air-sample interfaces within the waveguide.

The NRW method begins the expression of the transmission term, T from equation:

$$T = \frac{V_1 - \Gamma}{1 - \Gamma V_1}, \tag{8}$$

with:

$$\Gamma = \frac{T - V_2}{1 - \Gamma V_2}. \tag{9}$$

Γ= reflection coefficient

and:

$$V_1 = S_{21} + S_{11}, \tag{10}$$
$$V_2 = S_{21} - S_{11}, \tag{11}$$

and:

We obtain from (8) and (9) the equation:

$$1 - T = \frac{(1+\Gamma)(1-V_1)}{1 - \Gamma V_1}. \tag{12}$$

Assuming that the electrical thickness of the LHM slab is not large $(i.e., k_{real} d \le 1)$ and aware that the wave number

$$K = \frac{\omega\sqrt{\varepsilon_r \mu_r}}{c} = k_0\sqrt{\varepsilon_r \mu_r}. \tag{13}$$

The transmission term can be written as $T \approx 1 - jkd$ to obtain the approximate results of permittivity and permeability:

$$\varepsilon_r \approx \frac{2}{jk_0 d}\frac{1-V_1}{1+V_1}, \tag{14}$$

$$\mu_r \approx \frac{2}{jk_0 d}\frac{1-V_2}{1+V_2}, \tag{15}$$

where:

$$V_1 = S_{21} + S_{11}, \tag{16}$$
$$V_2 = S_{21} - S_{11}, \tag{17}$$
$$k_0 = \omega / c, \tag{18}$$
$$\omega = \text{radian frequency}.$$

IV. RESULTS AND DISCUSSION

We study the particle along the X propagation. Figures 2a and 2b, show the amplitude and phase information of the calculated S parameters for the metamaterial structure, it can be seen that $S11$ is equal to $S22$, and $S12$ is equal to $S21$, since the structure is symmetric in the x-direction. Accordingly, using the standard retrieval method [18] and the Nicholson-Weir-Ross approach, the results for an impedance, effective refractive index, effective permittivity, and permeability are presented. The impedance shown in Fig. 3a, shows that the structure is indeed roughly matched at 7GHz. Referring to Fig. 3(c) and Fig. 3(d), the range of the simultaneous negative permittivity and permeability starts from 6.9 GHz to 7.6 GHz. Also, Fig. 3(b) confirms the negative index using the two methods in the same band. The deviation between the results obtained from the two extraction methods in Fig. 3b and Fig. 3c is due to the approximation of equations of ε and μ in NRW extraction.

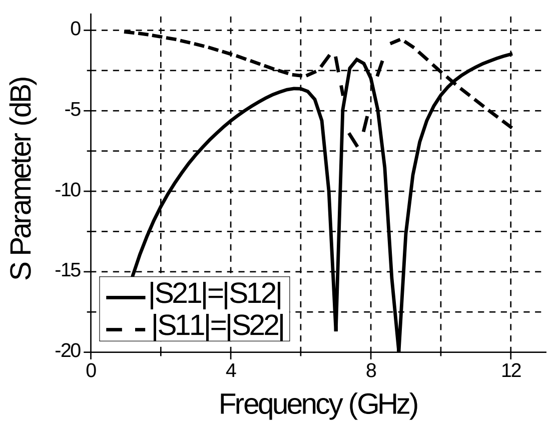

(a)

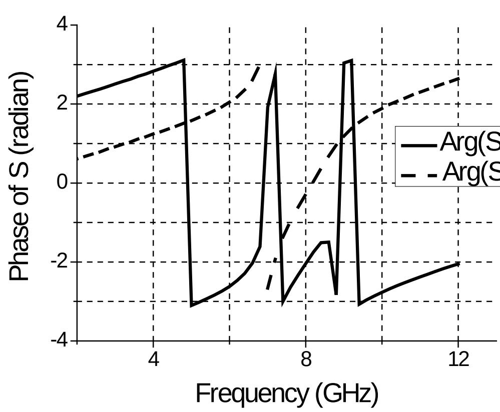

(b)

Fig. 2. (a) Magnitude and (b) phase of the simulated S parameters for the unit cell in Fig. 1a.

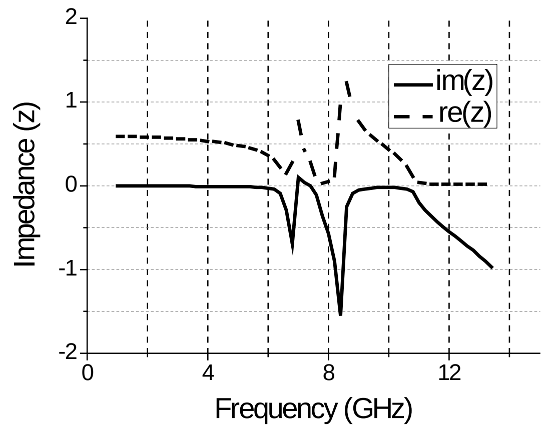

(a)

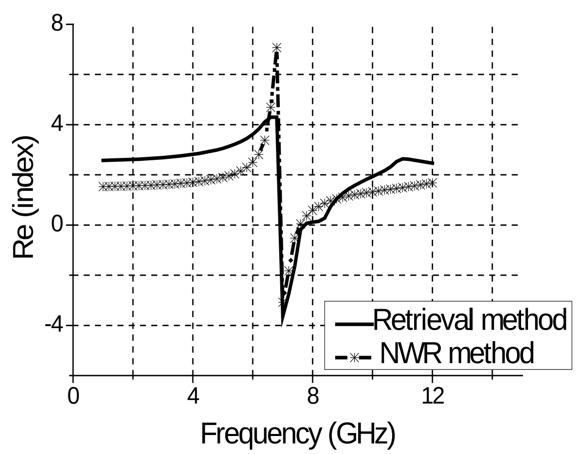

(b)

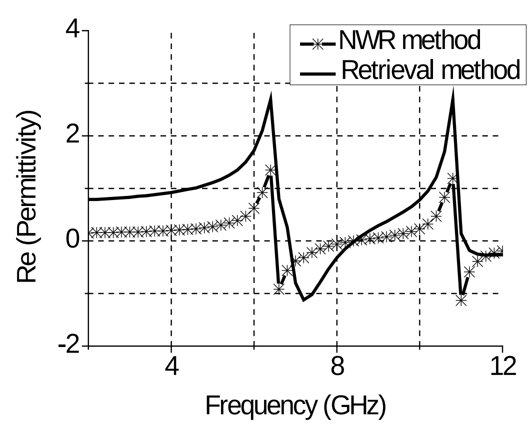

(c)

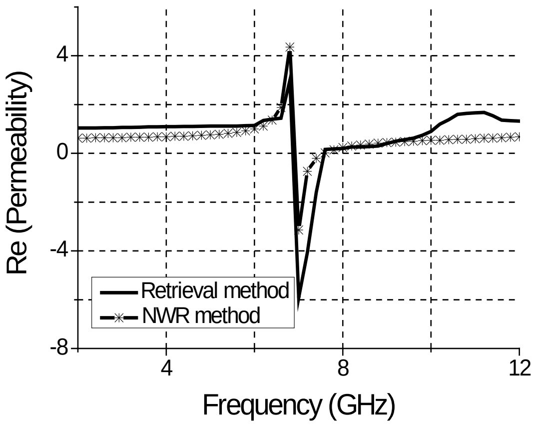

(d)

Fig. 3. (a) Retrieved impedance, (b) retrieved and NRW index, (c) retrieved and NRW real part of permittivity, (d) retrieved and NRW real part of permeability.

Figures 4 and 5 show the real and imaginary parts of the permeability and permittivity for various values of P, respectively. We observe that the general variation of the P-parameter has no impact on the signs of the permittivity (Fig. 5a-b). There is just a variation of the resonance frequency due to the variation of the total length of the radiating element. On the other hand, the parameter has an impact on the permeability. For P = 0, our resonator has a constant permeability (Fig. 4a), moreover, the real part of the refractive index (Fig. 6a) remains negative because observing the Fig. 4b, the imaginary permeability is positive for P=0, and having the real part of permittivity is negative (Fig. 5a), we obtain the necessary condition for a negative refractive index [25]:

$$\varepsilon'\mu'' + \varepsilon''\mu' \prec 0. \tag{19}$$

Figure 6b shows the imaginary part of refractive index.

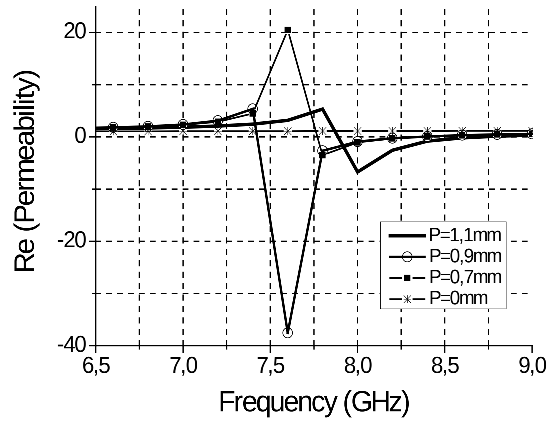

(a)

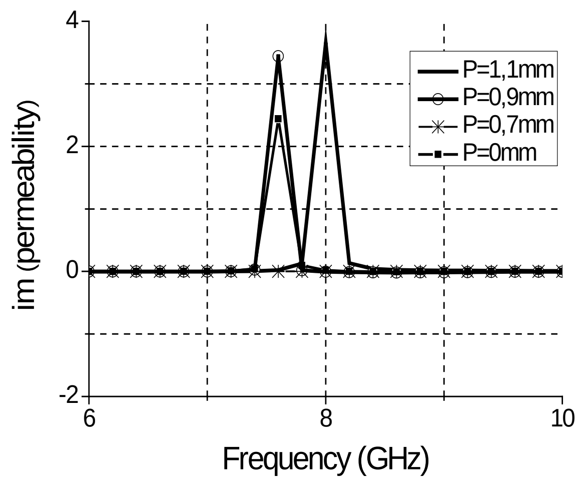

(b)

Fig. 4. (a) Standard retrieved real part of permeability for various P, (b) standard retrieved imaginary part of permeability for various P.

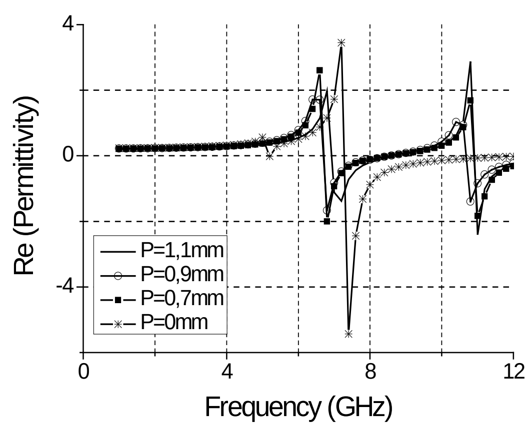

(a)

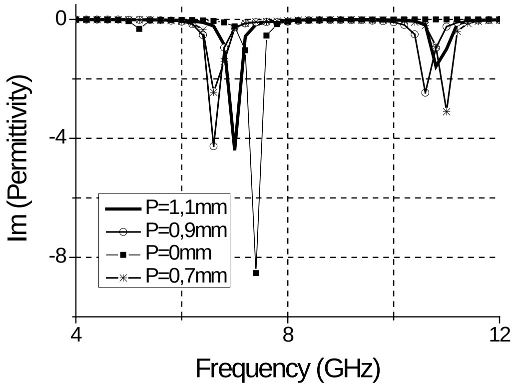

(b)

Fig. 5. (a) Standard retrieved real part of permittivity for various P, (b) standard retrieved imaginary part of permittivity for various P.

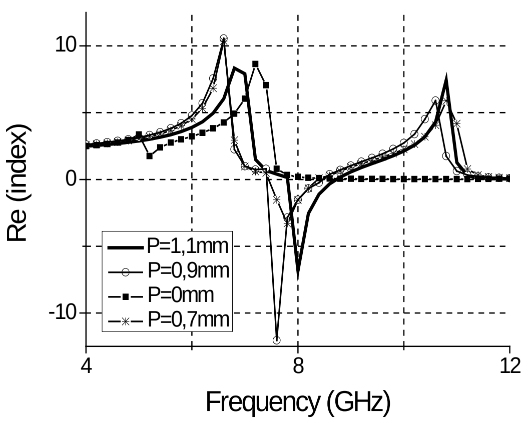

(a)

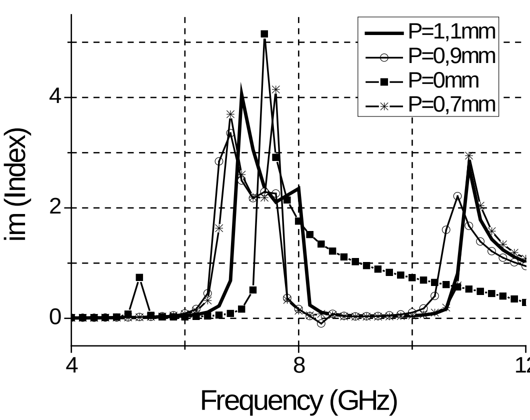

(b)

Fig. 6. (a) Standard retrieved real part of index for various P, (b) standard retrieved imaginary part of index for various P.

V. CONCLUSION

The design and study of a new LHM resonator based on two split triangles has been shown at microwave frequencies. The good agreement between NRW and standard retrieval method for two different directions of propagation is observed. The results confirm the existence of the LHM with simultaneous negatives permittivity and permeability. The effect of “P” parameter on the magnetic resonance of STR was observed. However, STRs present the important advantage of double negative ε and μ printing metallic elements just in one side (top side) of the substrate.

REFERENCES

[1] D. R. smith, W. J. Padilla, D. C. Vier, S. C. Nemat-Nasser, and S. Schultz, “Composite medium with simultaneously negative permittivity and permeability”, *Phys. Rev. Lett.*, 84, 4184-4187, 2000.

[2] R. Shelby, D. R. Smith, and S. Schultz, “Experimental Verification of a Negative Index of Refraction”, *Science* 292, pp. 77-79, 2001.

[3] J. B. Pendry, “Negative Refraction Makes a Perfect Lens,” *Phys. Rev. Lett.*, vol. 85, 3966-3969, 2000.

[4] I. V. Lindell, S. A. Tretyakov, K. I. Nikoskinen, and S. Ilvonen, “BW Media with Negative Parameters, Capable of Supporting Backward Waves,” *Micr. Opt. Tech. Lett.*, 31, pp. 129-133, 2001.

[5] G. Monti and L. Tarricone, “Dispersion Analysis of a Negative Group Velocity Medium with MATLAB,” *Applied Computational Electromagnetic Society (ACES) Journal*, vol. 24, no. 5, pp. 478-486, October 2009.

[6] J. Lu, T. M. Grzegorczyk, Y. Zhang, J. Pacheco, B.-I. Wu, J. A. Kong, and M. Chen, “Cerenkov Radiation in Materials with Negative Permittivity and Permeability,” *Optics Express*, vol. 11, pp.723-734, 2003.

[7] N. Engheta, “An Idea for Thin Subwavelength Cavity Resonators using Metamaterials with Negative Permittivity and Permeability,” *IEEE Antennas Wireless Propagation Letters*, vol. 1, pp. 10-13, 2002.

[8] W. J. Smith, D. C. Padilla, S. C. Vier, Nemat-Nasser, and S. Schultz, “Composite Medium with Simultaneously Negative Permeability and Permittivity,” *Phys. Rev. Lett.*, vol. 84, no. 18, 4184-4187, 2000.

[9] C. Caloz and T. Itoh, *Electromagnetic Metamaterials: Transmission Line Theory and*

Microwave Applications, Piscataway, NJ: Wiley-IEEE, 2005.

[10] J. B. Pendry, A. J. Holden, D. J. Robbins, and W. J. Stewart, "Magnetism from Conductors, and Enhanced," *IEEE Trans. on Microwave Theory and Techniques*, vol. 47, no. 11, November 1999.

[11] V. G. Veselago, "The Electrodynamics of Substances with Simultaneously Negative Values of ε and μ," *Sov. Phys. Uspekhi,* vol. 10, pp. 509-514, Jan.-Feb. 1968.

[12] C. R. Simovski and S. L. He , "Frequency Range and Explicit Expressions for Negative Permittivity and Permeability for an Isotropic Medium Formed by a Lattice of Perfectly Conducting Omega Particles," *Phys. Lett.,* A, 311, 254, 2003.

[13] L. Ran, J. Huangfu, H. Chen, Y. Li, X. Zhang, K. Chen, and J. A. Kong, "Microwave Solid-State Left-Handed Material with a Broad Bandwidth and an Ultralow Loss," *Phys. Rev.* B, vol. 70, 073102, 2004.

[14] B. D. Braaten, R. P. Scheeler, M. Reich, R. M. Nelson, C. Bauer-Reich, J. Glower, and G. J. Owen, "Compact Metamaterial-Based UHF RFID Antennas: Deformed Omega and Split-Ring Resonator Structures," *Applied Computational Electromagnetic Society (ACES) Journal,* vol. 25, no. 6, pp. 530-542, June 2010.

[15] M. Kafesaki, I. Tsiapa, N. Katsarakis, Th. Koschny, C. M. Soukoulis, and E. N. Economou, "Left-Handed Metamaterials: The Fishnet Structure and its Variations," *Phys. Rev. B,* vol. 75, 235114, 2007.

[16] W. B. Weir, "Automatic measurement of complex dielectric constant and permeability at microwave frequencies", *Proc. IEEE*, vol.62, no.1, pp. 33-36, Jan. 1974.

[17] A. M. Nicholson and G. F. Ross, "Measurement of the intrinsic properties of materials by time domain techniques", *IEEE Trans. Instrum. Meas.*, IM-19, pp. 377-382, 1970.

[18] D. R. Smith, D. C. Vier, Th. Koschny, and C. M. Soukoulis, "Electromagnetic Parameter Retrieval from Inhomogeneous Metamaterials", Foundation for Research and Technology Hellas (FORTH), 71110 Heraklion, Crete, Greece, March 2005.

[19] D. R. Smith, S. Schultz, P. Markoš, and C. M. Soukoulis, "Determination of effective permittivity and permeability of metamaterials from reflection and transmission coefficients", *Phys. Rev. B*, vol. 65, 195104, 2002.

[20] D. M. Pozar, *Microwave Engineering*, 2nd eds. John Wiley & Sons, New York, p. 211, 1998.

[21] H. Bahrami and M. Hakkak, "Analysis and Design of Highly Compact Band-Pass Waveguide Filter Utilizing Complementary Split Ring Resonator (CSRR)," *Progress In Electromagnetics Research*, vol. 80, pp. 107–122, 2008.

[22] Michel A. Abaga Abessolo, A. El Moussaoui, and N. Aknin, "Dual-Band Monopole Antenna with Omega Particles for Wireless Applications," *Progress In Electromagnetics Research Letters*, vol. 24, pp. 27-34, 2011.

[23] Z. Duan, S. Qu, and Y. Hou, "Electrically Small Antenna Inspired by Spired Split Ring Resonator," *Progress In Electromagnetics Research Letters*, vol. 7, pp. 47-57, 2009.

[24] G. Du, X. Tang, and F. Xiao, "Tri-Band Metamaterial-Inspired Monopole Antenna with Modified S-Shaped Resonator," *Progress In Electromagnetics Research Letters*, vol. 23, pp. 39-48, 2011.

[25] U. K. Chettiar, A. V. Kildishev, H.-K. Yuan, W. Cai, S. Xiao, V. P. Drachev, and V. M. Shalaev, "Double Negative Index Metamaterial: Simultaneous Negative Permeability and Permittivity at 812 nm", *Optical Society of America*, 2007.

[26] X.-C. Zhang, Z.-Y. Yu, and J. Xu, "Nouvel Band-Pass Substrate Integrated Waveguide (SIW) Filter Based on Complementary Split Ring Resonators (CSRRS)," *Progress In Electromagnetics Research,* vol. 72, pp. 39-46, 2007.

[27] H. Chen, L. Ran, J. Huangfu, X. Zhang, and K. Chen, "Left-Handed Materials Composed of Only S-Shaped Resonators," *Phys. Rev. E*, vol. 70, 057605, 2004.

[28] J. B. Pendry, "Calculating Photonic Band Structure", *J. Phys. Condens. Matter*, vol. 8, pp. 1085-1108, Feb 1996.

Michel A. Abaga Abessolo was born in Oyem, Gabon, in January 1981. He received the Licence es sciences in Physics from Abdelmalek Essaadi University, Tetuan, Morocco, in 2005 and the DESA degree in information and telecommunication systems from the Abdelmalek Essaadi University, Tetuan, Morocco, in 2007. He is currently working toward the Ph.D. degree under the direction of Profs. M. El Moussaoui and Mrs. Aknin at the Abdelmalek Essaadi University. His current interest includes microwave antennas and filters based on enhanced transmission phenomena, and metamaterials.

Noura Aknin received the Licence in Physics and the Ph.D. degree in Electrical Engineering, respectively, in 1988 and 1998 from Abdelmalek Essaadi University in Tetuan, Morocco. She is a Professor of Telecommunications and Computer Engineering in Abdelmalek Essaadi University since 2000. She is the co-founder of the IEEE Morocco Section since November 2004 and she is the Women in Engineering Coordinator. She has been a member of the Organizing and the Scientific Committees of several symposia and conferences dealing with RF, Mobile Networks, Social Web, and information technologies. Prof. Noura Aknin is a member of IEEE Communications Society and Computer Society. Her research interests focus mainly on Wireless and mobile communication systems, radio network planning and optimization. Moreover, she is the project manager for research & development project related to Mobile Networks funded by the national telecommunications company “Maroc Telecom”.

A. El MOUSSAOUI received the Ph.D. degree in Electronics at the University of BRADFOR in 1990. In 2007, he received the International Master in E-learning in the Curt Bosh institute in Switzerland. He has been a member of the Organizing and the Scientific Committees of several symposia and conferences dealing with RF, mobile networks, and information technologies. He has participated in several project with France and Spain. His research interests are: electronic engineering, third generation mobile system, radio network planning and optimization. Currently, he is the vice president of Abdelmalek Essaidi University in Tetuan, Morocco.

2011 INSTITUTIONAL MEMBERS

DTIC-OCP LIBRARY
8725 John J. Kingman Rd, Ste 0944
Fort Belvoir, VA 22060-6218

AUSTRALIAN DEFENCE LIBRARY
Northcott Drive
Canberra, A.C.T. 2600 Australia

BEIJING BOOK CO, INC
701 E Linden Avenue
Linden, NJ 07036-2495

DARTMOUTH COLLEGE
6025 Baker/Berry Library
Hanover, NH 03755-3560

DSTO EDINBURGH
AU/33851-AP, PO Box 830470
Birmingham, AL 35283

SIMEON J. EARL – BAE SYSTEMS
W432A, Warton Aerodome
Preston, Lancs., UK PR4 1AX

ENGINEERING INFORMATION, INC
PO Box 543
Amsterdam, Netherlands 1000 Am

ETSE TELECOMUNICACION
Biblioteca, Campus Lagoas
Vigo, 36200 Spain

GA INSTITUTE OF TECHNOLOGY
EBS-Lib Mail code 0900
74 Cherry Street
Atlanta, GA 30332

TIMOTHY HOLZHEIMER
Raytheon
PO Box 1044
Rockwall, TX 75087

HRL LABS, RESEARCH LIBRARY
3011 Malibu Canyon
Malibu, CA 90265

IEE INSPEC
Michael Faraday House
6 Hills Way
Stevenage, Herts UK SG1 2AY

INSTITUTE FOR SCIENTIFIC INFO.
Publication Processing Dept.
3501 Market St.
Philadelphia, PA 19104-3302

LIBRARY – DRDC OTTAWA
3701 Carling Avenue
Ottawa, Ontario, Canada K1A OZ4

LIBRARY of CONGRESS
Reg. Of Copyrights
Attn: 407 Deposits
Washington DC, 20559

LINDA HALL LIBRARY
5109 Cherry Street
Kansas City, MO 64110-2498

MISSOURI S&T
400 W 14th Street
Rolla, MO 56409

MIT LINCOLN LABORATORY
Periodicals Library
244 Wood Street
Lexington, MA 02420

NATIONAL CHI NAN UNIVERSITY
Lily Journal & Book Co, Ltd
20920 Glenbrook Drive
Walnut, CA 91789-3809

JOHN NORGARD
UCCS
20340 Pine Shadow Drive
Colorado Springs, CO 80908

OSAMA MOHAMMED
Florida International University
10555 W Flagler Street
Miami, FL 33174

NAVAL POSTGRADUATE SCHOOL
Attn:J. Rozdal/411 Dyer Rd./ Rm 111
Monterey, CA 93943-5101

NDL KAGAKU
C/0 KWE-ACCESS
PO Box 300613 (JFK A/P)
Jamaica, NY 11430-0613

OVIEDO LIBRARY
PO BOX 830679
Birmingham, AL 35283

DAVID PAULSEN
E3Compliance
1523 North Joe Wilson Road
Cedr Hill, TX 75104-1437

PENN STATE UNIVERSITY
126 Paterno Library
University Park, PA 16802-1808

DAVID J. PINION
1122 E Pike Street #1217
SEATTLE, WA 98122

KATHERINE SIAKAVARA
Gymnasiou 8
Thessaloniki, Greece 55236

SWETS INFORMATION SERVICES
160 Ninth Avenue, Suite A
Runnemede, NJ 08078

YUTAKA TANGE
Maizuru Natl College of Technology
234 Shiroya
Maizuru, Kyoto, Japan 625-8511

TIB & UNIV. BIB. HANNOVER
DE/5100/G1/0001
Welfengarten 1B
Hannover, Germany 30167

UEKAE
PO Box 830470
Birmingham, AL 35283

UNIV OF CENTRAL FLORIDA
4000 Central Florida Boulevard
Orlando, FL 32816-8005

UNIVERSITY OF COLORADO
1720 Pleasant Street, 184 UCB
Boulder, CO 80309-0184

UNIVERSITY OF KANSAS – WATSON
1425 Jayhawk Blvd 210S
Lawrence, KS 66045-7594

UNIVERSITY OF MISSISSIPPI
JD Williams Library
University, MS 38677-1848

UNIVERSITY LIBRARY/HKUST
Clear Water Bay Road
Kowloon, Honk Kong

CHUAN CHENG WANG
8F, No. 31, Lane 546
MingCheng 2nd Road, Zuoying Dist
Kaoshiung City, Taiwan 813

THOMAS WEILAND
TU Darmstadt
Schlossgartenstrasse 8
Darmstadt, Hessen, Germany 64289

STEVEN WEISS
US Army Research Lab
2800 Powder Mill Road
Adelphi, MD 20783

YOSHIHIDE YAMADA
NATIONAL DEFENSE ACADEMY
1-10-20 Hashirimizu
Yokosuka, Kanagawa,
Japan 239-8686

APPLIED COMPUTATIONAL ELECTROMAGNETICS SOCIETY JOURNAL
http://aces.ee.olemiss.edu

INFORMATION FOR AUTHORS

PUBLICATION CRITERIA

Each paper is required to manifest some relation to applied computational electromagnetics. **Papers may address general issues in applied computational electromagnetics, or they may focus on specific applications, techniques, codes, or computational issues.** While the following list is not exhaustive, each paper will generally relate to at least one of these areas:

1. **Code validation.** This is done using internal checks or experimental, analytical or other computational data. Measured data of potential utility to code validation efforts will also be considered for publication.

2. **Code performance analysis.** This usually involves identification of numerical accuracy or other limitations, solution convergence, numerical and physical modeling error, and parameter tradeoffs. However, it is also permissible to address issues such as ease-of-use, set-up time, run time, special outputs, or other special features.

3. **Computational studies of basic physics.** This involves using a code, algorithm, or computational technique to simulate reality in such a way that better, or new physical insight or understanding, is achieved.

4. **New computational techniques** or new applications for existing computational techniques or codes.

5. **"Tricks of the trade"** in selecting and applying codes and techniques.

6. **New codes, algorithms, code enhancement, and code fixes.** This category is self-explanatory, but includes significant changes to existing codes, such as applicability extensions, algorithm optimization, problem correction, limitation removal, or other performance improvement. **Note: Code (or algorithm) capability descriptions are not acceptable, unless they contain sufficient technical material to justify consideration.**

7. **Code input/output issues.** This normally involves innovations in input (such as input geometry standardization, automatic mesh generation, or computer-aided design) or in output (whether it be tabular, graphical, statistical, Fourier-transformed, or otherwise signal-processed). Material dealing with input/output database management, output interpretation, or other input/output issues will also be considered for publication.

8. **Computer hardware issues.** This is the category for analysis of hardware capabilities and limitations of various types of electromagnetics computational requirements. Vector and parallel computational techniques and implementation are of particular interest.

Applications of interest include, but are not limited to, antennas (and their electromagnetic environments), networks, static fields, radar cross section, inverse scattering, shielding, radiation hazards, biological effects, biomedical applications, electromagnetic pulse (EMP), electromagnetic interference (EMI), electromagnetic compatibility (EMC), power transmission, charge transport, dielectric, magnetic and nonlinear materials, microwave components, MEMS, RFID, and MMIC technologies, remote sensing and geometrical and physical optics, radar and communications systems, sensors, fiber optics, plasmas, particle accelerators, generators and motors, electromagnetic wave propagation, non-destructive evaluation, eddy currents, and inverse scattering.

Techniques of interest include but not limited to frequency-domain and time-domain techniques, integral equation and differential equation techniques, diffraction theories, physical and geometrical optics, method of moments, finite differences and finite element techniques, transmission line method, modal expansions, perturbation methods, and hybrid methods.

Where possible and appropriate, authors are required to provide statements of quantitative accuracy for measured and/or computed data. This issue is discussed in "Accuracy & Publication: Requiring, quantitative accuracy statements to accompany data," by E. K. Miller, *ACES Newsletter,* Vol. 9, No. 3, pp. 23-29, 1994, ISBN 1056-9170.

SUBMITTAL PROCEDURE

All submissions should be uploaded to ACES server through ACES web site (http://aces.ee.olemiss.edu) by using the upload button, journal section. Only pdf files are accepted for submission. The file size should not be larger than 5MB, otherwise permission from the Editor-in-Chief should be obtained first. Automated acknowledgment of the electronic submission, after the upload process is successfully completed, will be sent to the corresponding author only. It is the responsibility of the corresponding author to keep the remaining authors, if applicable, informed. Email submission is not accepted and will not be processed.

EDITORIAL REVIEW

In order to ensure an appropriate level of quality control, papers are peer reviewed. They are reviewed both for technical correctness and for adherence to the listed guidelines regarding information content and format.

PAPER FORMAT

Only camera-ready electronic files are accepted for publication. The term **"camera-ready" means that the material is neat, legible, reproducible, and in accordance with the final version format listed below.**

The following requirements are in effect for the final version of an ACES Journal paper:

1. The paper title should not be placed on a separate page.

The title, author(s), abstract, and (space permitting) beginning of the paper itself should all be on the first page. The title, author(s), and author affiliations should be centered (center-justified) on the first page. The title should be of font size 16 and bolded, the author names should be of font size 12 and bolded, and the author affiliation should be of font size 12 (regular font, neither italic nor bolded).

2. An abstract is required. The abstract should be a brief summary of the work described in the paper. It should state the computer codes, computational techniques, and applications discussed in the paper (as applicable) and should otherwise be usable by technical abstracting and indexing services. The word "Abstract" has to be placed at the left margin of the paper, and should be bolded and italic. It also should be followed by a hyphen (—) with the main text of the abstract starting on the same line.

3. All section titles have to be centered and all the title letters should be written in caps. The section titles need to be numbered using roman numbering (I. II. ….)

4. Either British English or American English spellings may be used, provided that each word is spelled consistently throughout the paper.

5. Internal consistency of references format should be maintained. As a guideline for authors, we recommend that references be given using numerical numbering in the body of the paper (with numerical listing of all references at the end of the paper). The first letter of the authors' first name should be listed followed by a period, which in turn, followed by the authors' complete last name. Use a coma (,) to separate between the authors' names. Titles of papers or articles should be in quotation marks (" "), followed by the title of journal, which should be in italic font. The journal volume (vol.), issue number (no.), page numbering (pp.), month and year of publication should come after the journal title in the sequence listed here.

6. Internal consistency shall also be maintained for other elements of style, such as equation numbering. Equation numbers should be placed in parentheses at the right column margin. All symbols in any equation have to be defined before the equation appears or right immediately following the equation.

7. The use of SI units is strongly encouraged. English units may be used as secondary units (in parentheses).

8. Figures and tables should be formatted appropriately (centered within the column, side-by-side, etc.) on the page such that the presented data appears close to and after it is being referenced in the text. When including figures and tables, all care should be taken so that they will appear appropriately when printed in black and white. For better visibility of paper on computer screen, it is good to make color figures with different line styles for figures with multiple curves. Colors should also be tested to insure their ability to be distinguished after black and white printing. Avoid the use of large symbols with curves in a figure. It is always better to use different line styles such as solid, dotted, dashed, etc.

9. A figure caption should be located directly beneath the corresponding figure, and should be fully justified.

10. The intent and meaning of all text must be clear. For authors who are not masters of the English language, the ACES Editorial Staff will provide assistance with grammar (subject to clarity of intent and meaning). However, this may delay the scheduled publication date.

11. Unused space should be minimized. Sections and subsections should not normally begin on a new page.

ACES reserves the right to edit any uploaded material, however, this is not generally done. It is the author(s) responsibility to provide acceptable camera-ready files in pdf and MSWord formats. Incompatible or incomplete files will not be processed for publication, and authors will be requested to re-upload a revised acceptable version.

COPYRIGHTS AND RELEASES

Each primary author must execute the online copyright form and obtain a release from his/her organization vesting the copyright with ACES. Both the author(s) and affiliated organization(s) are allowed to use the copyrighted material freely for their own private purposes.

Permission is granted to quote short passages and reproduce figures and tables from and ACES Journal issue provided the source is cited. Copies of ACES Journal articles may be made in accordance with usage permitted by Sections 107 or 108 of the U.S. Copyright Law. This consent does not extend to other kinds of copying, such as for general distribution, for advertising or promotional purposes, for creating new collective works, or for resale. The reproduction of multiple copies and the use of articles or extracts for commercial purposes require the consent of the author and specific permission from ACES. Institutional members are allowed to copy any ACES Journal issue for their internal distribution only.

PUBLICATION CHARGES

All authors are allowed for 8 printed pages per paper without charge. Mandatory page charges of $75 a page apply to all pages in excess of 8 printed pages. Authors are entitled to one, free of charge, copy of the printed journal issue in which their paper was published. Additional reprints are available for $ 50. Requests for additional re-prints should be submitted to the managing editor or ACES Secretary.

Corresponding author is required to complete the online form for the over page charge payment right after the initial acceptance of the paper is conveyed to the corresponding author by email.

ACES Journal is abstracted in INSPEC, in Engineering Index, DTIC, Science Citation Index Expanded, the Research Alert, and to Current Contents/Engineering, Computing & Technology.